

MULTI-FREQUENCY ELECTRICAL CONDUCTIVITY IMAGING VIA
CONTACTLESS MEASUREMENTS

A THESIS SUBMITTED TO
THE GRADUATE SCHOOL OF NATURAL AND APPLIED SCIENCES
OF
MIDDLE EAST TECHNICAL UNIVERSITY

BY

KORAY ÖZDAL ÖZKAN

IN PARTIAL FULFILLMENT OF THE REQUIREMENTS
FOR
THE DEGREE OF MASTER OF SCIENCE
IN
ELECTRICAL AND ELECTRONICS ENGINEERING

JANUARY 2006

Approval of the Graduate School of Natural and Applied Sciences.

Prof. Dr. Canan Özgen
Director

I certify that this thesis satisfies all the requirements as a thesis for the degree of Master of Science.

Prof. Dr. İsmet Erkmn
Head of Department

This is to certify that we have read this thesis and that in our opinion it is fully adequate, in scope and quality, as a thesis for the degree of Master of Science.

Prof. Dr. Nevzat G. Gençer
Supervisor

Examining Committee Members

Prof. Dr. Y. Ziya İder (Bilkent Unv., EE)

Asst. Prof. Dr. Yeşim S. Doğrusöz (METU, EE)

Prof. Dr. Kemal Leblebicioğlu (METU, EE)

Prof. Dr. Cengiz Beşikçi (METU, EE)

Prof. Dr. Nevzat G. Gençer (METU, EE)

ABSTRACT

MULTI-FREQUENCY ELECTRICAL CONDUCTIVITY IMAGING VIA CONTACTLESS MEASUREMENTS

Özkan, Koray Özdal

Ms, Department of Electrical and Electronics Engineering

Supervisor: Prof. Dr. Nevzat G. Gençer

January 2006, 108 pages

A multi-frequency data acquisition system is realized for subsurface conductivity imaging of biological tissues. The measurement procedures of the system at different frequencies are same. The only difference between the single frequency experiments and the multi-frequency experiments is the hardware, i.e. the sensor and the power amplifier used in the single frequency experiments was different than that were used in the multi-frequency experiments. To avoid confusion the measurement system with which the single frequency experiments were performed is named as prototype system and the measurement system with which the multi-frequency experiments were performed is named as multi-frequency system. This system uses magnetic excitation (primary field) to induce eddy currents inside the conductive object and measures the resulting magnetic field due to eddy currents (secondary field). For this purpose, two differential-coil sensors are constructed; one is for the single frequency measurements and the other is for the multi-frequency measurements. Geometrically the coils are same, the only difference between them is the ra-

dius of the wires wound on them. The sensor consists of two differentially connected identical receiver coils employed to measure secondary field and in between the receiver coils is placed a transmitter coil, which creates the primary field. The coils are coaxial. In the prototype system the transmitter coil is driven by a sinusoidal current of 300 mA (peak) at 50 kHz. In the multi-frequency system the transmitter coil is driven by a sinusoidal current of 217 mA (peak), 318 mA (peak), 219 mA (peak) and 211 mA (peak) at 30 kHz, 50 kHz, 60 kHz and 90 kHz, respectively. A data acquisition card (DAcC) is designed and constructed on a printed circuit board (PCB) for phase sensitive detection (PSD). The equivalent input noise voltage of the card was found as 146.80 nV. User interface programs (UIP) are prepared to control the scanning experiments via PC (HP VEE based UIP, LabVIEW based UIP) and to analyze the acquired data (MATLAB based UIP). A novel sensitivity test method employing resistive ring phantoms is developed. A relation between the classical saline solution filled vessel (45mm radius, 10 mm depth) phantoms and the resistive ring phantoms is established. The sensitivity of the prototype system to saline solutions filled vessels is 13.2 mV/(S/m) and to resistive rings is 155.02 mV/Mho while the linearity is 3.96% of the full scale for the saline solution filled vessels and 0.12% of the full scale for the resistive rings. Also the sensitivity of the multi-frequency system is determined at each operation frequency by using resistive ring phantoms. The results are in consistence with the theory stating that the measured signals are linearly proportional with the square of the frequency. The signal to noise ration (SNR) of the prototype system is calculated as 35.44 dB. Also the SNR of the multi-frequency system is calculated at each operation frequency. As expected, the SNR of the system increases as the frequency increases. The system performance is also tested with agar phantoms. Spatial resolution of the prototype system is found 9.36 mm in the point spread function (PSF) sense and 14.4 mm in the line spread function (LSF) sense. Spatial resolution of the multi-frequency system is also found at each operation frequency. The results show that the resolving power of the system to distinguish image details increases as the frequency

increases, as expected. Conductivity distributions of the objects are reconstructed using Steepest-Descent algorithm. The geometries and the locations of the reconstructed images match with those of the real images. The image of a living tissue, a leech, is acquired for the first time in the literature. Magnetic conductivity spectroscopy of a biological tissue is shown for the first time in electrical conductivity imaging via contactless measurements. The results show the potential of the methodology for clinical applications.

Keywords: Magnetic induction, Medical imaging, Contactless conductivity measurements, Electrical impedance imaging

ÖZ

KONTAK OLMADAN ÇOK-FREKANSLI ELEKTRİKSEL İLETKENLİK GÖRÜNTÜLENMESİ

Özkan, Koray Özdal

Yüksek Lisans, Elektrik ve Elektronik Mühendisliği Bölümü

Tez Yöneticisi: Prof. Dr. Nevzat G. Gençer

Ocak 2006, 108 sayfa

Biyolojik dokuların yüzeyaltı iletkenliklerinin görüntülenmesi için çok-frekanslı bir veri işleme sistemi gerçekleştirilmiştir. Sistemin farklı frekanslardaki ölçme prosedürü aynıdır. Tek-frekanslı deneyler ile çok-frekanslı deneyler arasındaki tek fark donanımdır. Karışıklığı önlemek için tek-frekanslı deneylerin yapıldığı sistem prototip sistem, çok-frekanslı deneylerin yapıldığı sistem ise çok-frekanslı sistem olarak adlandırılmıştır. Sistem, manyetik uyarım (birincil alan) kullanılarak iletken cisimler içerisinde Eddy akımları oluşturur ve bu akımların yarattığı manyetik alanları (ikincil alan) ölçer. Bu amaçla biri prototip sistem, diğeri ise çok-frekanslı sistem için olmak üzere 2 fark-sensörü oluşturulmuştur. Geometrik olarak sensörler aynıdır, farkları ise üzerlerine sarılan bobinin yarıçapıdır. Sensör ikincil alanları ölçmek için 2 özdeş alıcı bobin ve bunların arasına, birincil alanı oluşturmak için, konulmuş 1 verici bobinden oluşur. Bobinler eş merkezlidirler. Prototip sistemde verici bobin 50 kHz frekanslı tepe değeri 300 mA olan sinüzoidal akımla sürülmüştür. Çok-frekanslı sistemde verici bobin sırasıyla frekansları 30 kHz, 50 kHz, 60 kHz ve 90 kHz, tepe

değerleri ise 217 mA, 318 mA, 219 mA ve 211 mA olan sinüzoidal akımlarla sürülmüştür. Faza duyarlı ölçümler için bir veri toplama kartı tasarlanmış ve baskı devre üzerine basılmıştır. Kartın giriş gürültü gerilimi 146.80 nV olarak hesaplanmıştır. Deneyleri bilgisayarla yapmak için HP-VEE ve LabVIEW programları, toplanan verileri işlemek için ise MATLAB programı kullanılarak arayüz programları yazılmıştır. Halka şeklinde dirençler kullanılarak sistemin hassasiyetini ölçen yeni bir test metodu geliştirilmiştir. Direnç fantomları ve tuzlu su fantomları arasında bir ilişki sağlanmıştır. Prototip sistemin tuzlu su fantomlarına hassasiyeti 13.2 mV/(S/m), direnç fantomlarına hassasiyeti ise 155.02 mV/Mho iken doğrusallığı tuzlu sular için tüm ekseninde %3.96, dirençler için ise tüm ekseninde % 0.12'dir. Çok-frekanslı sistemin hassasiyeti direnç fantomları kullanılarak tüm çalışma frekanslarında hesaplanmıştır. Sonuçların teoriye uyduğu görülmüştür. Prototip sistemin sinyal gürültü oranı 35.44 dB dir. Çok-frekanslı sistemin sinyal gürültü oranı da her frekans için hesaplanmıştır. Beklenildiği gibi frekans arttıkça sistemin sinyal gürültü oranı da artmaktadır. Sistemin performansı agar fantomlarıyla da test edilmiştir. Prototip sistemin uzaysal çözünürlüğü nokta yayılım fonksiyonu ile 9.36 mm, çizgi yayılım fonksiyonu ile 14.4 mm olarak hesaplanmıştır. Her çalışma frekansı için çok-frekanslı sistemin uzaysal çözünürlüğü hesaplanmıştır. Sonuçlardan, beklenildiği gibi, frekans arttıkça sistemin cisimleri ayırtma gücünün arttığı görülmüştür. Cisimlerin iletkenlik görüntülerini oluşturmak için En Dik Azalma (Steepest-Descent) algoritması kullanılmıştır. Görüntüler gerçek cisimlerin yerleri ve geometrileri ile uyusmaktadır. Literatürde ilk kez canlı hayvan deneyi yapılmış ve bir sülük görüntülenmiştir. Yine dokunmasız yöntemlerle iletkenlik görüntülenmesi alanında bir ilk olarak biyolojik dokunun iletkenlik spektroskopisi çıkarılmıştır. Sonuçlar bu metodun klinik uygulamalar için potansiyelini göstermektedir.

Anahtar Kelimeler: Manyetik indükleme, Tıbbi görüntüleme, Dokunmasız iletkenlik ölçümleri, Elektriksel empedans görüntüleme

a

ACKNOWLEDGMENTS

I am deeply grateful to Prof. Dr. Nevzat G. GENÇER for his invaluable support, guidance and endless patience throughout this study. I want to express my deepest gratitude to Evrim ÇOLAK, for his help, criticism and encouragement. Without Dr. Gençer and Evrim these work would never have come into existence. My special thanks are going to Volkan Emre ARPINAR and Evren DEĞİRMENCİ for everything. I hereby declare that these three guys (EEE) are wonderful people. I would like to thank to my friends Dr. Zeynep Akalın ACAR, Dr. Can Erkin ACAR, Dr. Serap AYDIN, Taha AHİ, Yoldaş ATASEVEN, Cemil KIZILÖZ, Doğa GÜR SOY, Dario Martin LORCA, Murat ÖZSÜT, Reyhan TUTUK, Bülent UŞAKLI, Ayhan YILMAZ, Hüseyin YİĞİTLER and Hayrettin YÜZER for their comments and precious support. The valuable helps of Prof. Dr. Nilgün GÜNALP, Prof. Dr. Bülent ERTAN, Prof. Dr. Murat Eyübođlu in the Dept. of EEE and Dr. C. Can BİLGİN and his assistants Çiğdem and Didem in the Dept. of Biology are appreciated. Veyssel EREN and Zekeriya ÖZGÜN are gratefully acknowledged for their effort in machine shop. I would like to thank to Prof. Dr. Muhammet KÖKSAL and my teachers in İNÖNÜ ÜNİVERSİTESİ, my dear friends: Ebubekir AKEL, Sedat BARAN and his family, Ruken KAHRAMAN, Mustafa KÖSE and his family, Hülya ÖZTÜRK, and the VIP MALATYALILAR Turizm stuff including Ahmet ÖZER, 'the manager', from Tepehan, PÜTÜRGE. Finally I want to thank to the ARISAN's (Mehmet Murat, Derya Dilek, Selin, Sinem, Gizem), the ERBAŞ's (Sinan, Ayten, Ali, Mert), my mother Hikmet ÖZKAN and my sister Selcen Özgül ÖZKAN for their endless patience and CİNO for his endless biting. The author is supported by The Scientific & Technological Research Council of Turkey (TÜBİTAK) from March, 2004 to September, 2005.

TABLE OF CONTENTS

ABSTRACT	iii
ÖZ	vi
DEDICATION	viii
ACKNOWLEDGMENTS	viii
TABLE OF CONTENTS	x
LIST OF TABLES	xiii
LIST OF FIGURES	xiv
CHAPTER	
1 INTRODUCTION	1
1.1 Medical Imaging	1
1.2 Electrical Impedance Tomography	2
1.3 Electrical Conductivity Imaging via Contactless Measurements	6
1.4 Multi-Frequency Studies	13
1.5 Objective of the Study	15
1.6 Outline of the Thesis	15
2 THEORETICAL BACKGROUND	16
2.1 Introduction	16
2.2 Forward Problem	16
2.2.1 Calculation of Measurement Sensitivity to Conductivity Distribution Using the <i>Reciprocity Theorem</i>	17
2.2.2 Investigating the Relation of Magnetic Flux Density to Induced Currents by Using the <i>Biot-Savart Theorem</i>	21
2.3 Inverse Problem	22

	2.3.1	Characteristics of the imaging system	24
	2.3.2	The Steepest Descent Algorithm	29
3		EXPERIMENTAL SETUP	30
	3.1	Data Collection System	30
	3.1.1	Basic Operation Principle	30
	3.1.2	Power Amplifier	32
	3.1.3	Coils	33
	3.1.3.1	Characteristics of the prototype system sensor	33
	3.1.3.2	Sensor for the multi-frequency system	35
	3.1.4	Phase Sensitive Detection	35
	3.1.4.1	Introduction	35
	3.1.4.2	Basics of Phase Sensitive Detection	37
	3.1.4.3	The Data Acquisition Card	37
	3.2	XY Scanner System	44
	3.2.1	RS-232 Programming	47
	3.3	Data collection, acquisition and analysis software	47
	3.3.1	Data Collecting Step	48
	3.3.1.1	HP VEE Based User Interface Program	48
	3.3.1.2	LabVIEW Based User Interface Program	50
	3.3.2	Data Analysis Step	52
	3.3.2.1	MATLAB Based User Interface Program	52
4		RESULTS	54
	4.1	Introduction	54
	4.2	The Prototype System Operating at Single Frequency: 50 kHz	55
	4.2.1	Sensitivity to conductivity variations	55
	4.2.1.1	Saline Solution Phantoms	55
	4.2.1.2	Resistance Phantoms	57
	4.2.2	Signal to Noise Ratio	57
	4.2.3	Spatial Resolution	58

4.2.4	Image Reconstruction	58
4.2.4.1	Cylindrical Agar Phantom	59
4.2.4.2	Agar Phantom Bars	59
4.2.4.3	The First Conductivity Images of a Living Tissue	60
4.3	The Multi-Frequency System	70
4.3.1	Sensitivity	70
4.3.2	Signal to Noise Ratio	73
4.3.3	Spatial Resolution	74
4.3.4	Image Reconstruction	75
4.4	Spectroscopy	81
4.5	Equivalent Input Noise Voltage	82
4.5.1	Introduction	82
4.5.2	The Input Noise of the Data Acquisition Card	82
5	CONCLUSIONS AND DISCUSSION	83
5.1	Summary and Conclusion	83
5.2	Future Work	86
	REFERENCES	87
	APPENDICES	93
A	Useful Assumptions	93
A.1	Effects of Displacement Currents	93
A.2	Effects of $e^{-j\mathbf{k}\cdot\mathbf{R}}$ Term	93
B	RESISTANCE OF A CONDUCTIVE RING	95
C	MAGNETIC FIELD MEASUREMENT USING RESISTIVE RING EXPERIMENT	98
D	THERMAL NOISE	101
D.1	Equivalent Noise Bandwidth	102
D.2	Noise In IC Operational Amplifiers	104
D.3	Addition of Noise Voltages	105
E	AGAR PHANTOM PREPARATION	107
E.1	Equipment and Materials Needed	107
E.2	Preparation	107

LIST OF TABLES

1.1	The resistivity of body tissues at low frequencies (20 to 100 kHz [1])	3
3.1	Technical specifications of HY60	32
3.2	Technical specifications of XP3000	33
3.3	Coil Properties of the single-frequency prototype system . . .	35
3.4	Coil Properties of the multi-frequency system	35
3.5	Capacitors employed in series with the transmitter coil to cancel out the inductance of the coil in the multi-frequency system	37
4.1	The excitation currents and the slopes of the measured voltages at each operation frequency in the multi-frequency experiment.	73
4.2	SNR of the multi-frequency system at each operation frequency	74
4.3	FWHM of the multi-frequency system at each operation frequency.	75
A.1	Ratio of displacement to conduction currents for various frequencies and body tissues.	94
A.2	Wavelengths and skin depths for various frequencies, The wavelength and the skin depth is defined as: $\lambda = \frac{2\pi}{\beta}$ and $\sigma = \frac{1}{\alpha}$, respectively. The wave number k can be express as $k = \alpha + j\beta$.	94
A.3	Propagation related parameters for various frequencies. Error column shows the percentage error of magnitude from unity. Magnitude and phase difference of $e^{-j\mathbf{k}\mathbf{R}}$ is tabulated.	94
C.1	Resistor values (and corresponding $1/(\text{resistor values})$) used in the resistive ring experiments.	99
D.1	Ratio of the Noise Bandwidth B to the 3-dB Bandwidth f_0 . .	102

LIST OF FIGURES

1.1	The ACEIT measurement system. In this figure; time-varying currents are injected to the subject via the electrode # 10 and the electrode # 11, and the resultant voltage is measured using the electrode # 8 and the electrode # 9	5
1.2	The ICEIT measurement system. In this figure; time-varying magnetic fields, generated by sinusoidal current carrying wires encircling the conductive body, are applied to induce currents in the body and the voltage measurements are performed using the electrode # 8 and the electrode # 9	5
1.3	The measurement methodologies proposed by Ahmad and Gençer [2], [3]. (a) Single coil sensor model, (b) Two-coil sensor model.	11
1.4	The differential coil sensor.	12
1.5	Frequency variation of the relative permittivity ϵ_r , and conductivity σ for skin at 37 °C (Schwan 1965 [4], Yamamoto and Yamamoto 1976 [5]).	14
2.1	General principles of data collection in the magnetic-induction magnetic-measurement system. A transmitter coil is energized with low-frequency sinusoidal currents, generating time-varying magnetic fields. This induces currents in the nearby conductive body. A receiver coil senses the magnetic fields of both primary current in the transmitter coil, and the induced current in the conductive body.	17
2.2	Magnetic vector potential at point P created by current carrying loop.	18
2.3	Singular values of \mathbf{S}' normalized with the highest singular value. (a) $n = 256$ and $m = 256$, $\kappa = 719.6$, (b) $n = 1296$ and $m = 1296$, $\kappa = 2.3 \times 10^3$	26
2.4	Display of the right singular vectors corresponding to higher singular values.	27
2.5	Display of the right singular vectors corresponding to lower singular values.	28
3.1	The block diagram and appearance of the data acquisition system: (a) The block diagram of the system, (b) The appearance of the system.	31

3.2	Impedance as a function of frequency characteristic of the sensor used in the prototype system, (a) The transmitter coil characteristic (the resonance frequency is 2.55 MHz), (b) The differentially connected receiver coils characteristic (the resonance frequency is 306.02 kHz).	34
3.3	Impedance as a function of frequency characteristic of the sensor used in the multi-frequency system, (a) The transmitter coil characteristic (the resonance frequency is 3.225MHz), (b) The differentially connected receiver coils characteristic (the resonance frequency is 675.013 kHz).	36
3.4	The Data Acquisition Card (DAcC), (a) block diagram representation, (b) detailed block diagram representation.	38
3.5	Transmitter Coil Current Buffer. Transmitter coil current entering the DAcC at 'TRANSMITTER' flows through the capacitor connected between the sockets indicated as CAP and then passes from the monitor resistor in <i>R_M</i> socket and flows to the ground. Voltage on the monitor resistance (<i>REF_1</i>) is taken as the reference voltage and is buffered. The buffer output (<i>TR_BUF_OUT</i>) is connected to the input of the amplifier circuit (Figure 3.6).	40
3.6	Amplifier (A1 circuit) connections. Its input is the buffered monitor resistor (<i>R_M</i>) voltage <i>TR_BUF_OUT</i> (Figure 3.5). Total amplification factor of *111 is available with this configuration without any instability. Output of the amplifier is connected to the input of the phase shifter circuit (Figure 3.7).	40
3.7	Phase shifter (PS) circuit. Its input is the buffered & amplified monitor resistor (<i>R_M</i>) voltage <i>A1_OUT_S2</i> (Figure 3.6). In the phase shifter blocks switching the positions of the 2.2 nF capacitor and the 1+10+100 k Ω potentiometers results in the phase shifter a phase lag or phase lead circuit. Output of the PS is connected to the input of the multiplier (Figure 3.9).	41
3.8	Receiver coil signal buffer circuit connections. Output of the differentially connected coils is given to the DAcC via RECEIVER channel (Figure 3.5). Socket block named as <i>REC_CAP</i> is available in case capacitors between V_+ input of the buffer and ground are needed to load the receiver coils. The output of the buffer is connected to the input of the multiplier (Figure 3.9).	41
3.9	Multiplier circuit connections. AD633 is employed to multiply the buffered reference voltage and buffered receiver coil signal which are available at <i>Q1_OUT_S3</i> (Figure 3.7) and <i>REC_BUF_OUT</i> (Figure 3.8), respectively.	42
3.10	Amplifier circuit connections. Total amplification factor of *100 is available with this configuration without any instability.	42

3.11	Low Pass Filter circuit connections. Input to this circuit, comes from the output of the multiplier shown as <i>MULT_O</i> (Figure 3.9). To decrease the cutoff frequency of <i>F_1</i> , external 220 nF capacitors are connected in parallel to the internal 1000 pF capacitors buried in the filter IC [6], [7] (Pages 1 and 6). The output of the multiplier (<i>F_1_0_S3</i>) is connected to the input of the Amplifier (Figure 3.10)	43
3.12	PIC16F877 μC connecting scheme	45
3.13	Step motor driving circuitry. Since the direction of the motion is 2D, there are two step motors. Thus, two of these circuits are required to control the two step motors separately. Here ' <i>i</i> ' in <i>Dk_i</i> represents the motor number while ' <i>k</i> ' represents the pin number of the μC . The voltage levels in nodes <i>D7_1</i> , ..., <i>D4_1</i> (<i>D3_2</i> , ..., <i>D0_2</i> for the other step motor driver) controls the voltage levels in terminals 1, 3, 2 and 4, respectively. . . .	46
3.14	HP VEE 4.0 based user interface program.	48
3.15	LabVIEW based user interface program.	50
3.16	MATLAB based Graphical User Interface (GUI) program. . .	52
4.1	Receiver coil output voltages as a function of conductivity obtained by using saline solution phantoms (100 data are taken for each phantom).	56
4.2	Receiver coil output voltage as a function of conductivity obtained by using resistance phantoms (100 data are taken for each phantom)	56
4.3	Experiment result and inverse problem solution of 7.5 mm radius circular agar phantom: (a) measured field profile, (b) reconstructed conductivity distribution, (c) FWHM calculation.	62
4.4	Experiment result and inverse problem solution of 7.5 mm radius circular agar phantom placed at the center of the scanning area: (a) measured field profile, (b) reconstructed conductivity distribution.	63
4.5	Experiment result and inverse problem solution of the 15 mm width, 57 mm long bar shaped agar phantom : (a) measured field profile, (b) reconstructed conductivity distribution.	64
4.6	Experiment result and inverse problem solution of two 15 mm width, 57 mm long bar shaped agar phantoms : (a) measured field profile, (b) reconstructed conductivity distribution, (c) image spread along axial direction.	66
4.7	The first conductivity images of a living tissue: imaging a leech. (a) The measured field profile, (b) reconstructed conductivity distribution, (c) photograph of the leech, (d) edges of the reconstructed conductivity distribution, (e) the leech boundaries and the reconstructed conductivity distribution are shown on the same figure.	69
4.8	Receiver coil output voltage as a function of conductivity at (a) 30 kHz, (b) 50 kHz, (c) 60 kHz, (d) 90 kHz.	72

4.9	The normalized slopes of the sensitivity experiments (receiver coil output as a function of conductivity measurements) at each operation frequency. In theory (Equation 2.9), the measured voltage is proportional to the square of the frequency. . .	73
4.10	SNR of the multi-frequency system as a function of frequency.	74
4.11	Measured profile on the horizontal line of Figure 4.15(b). The FWHM is calculated as 19.8 mm at 30 kHz.	76
4.12	Measured profile on the horizontal line of Figure 4.15(b). The FWHM is calculated as 10.8 mm at 60 kHz.	76
4.13	Measured profile on the horizontal line of Figure 4.17(b). The FWHM is calculated as 9 mm at 90 kHz.	77
4.14	The photograph of the phantom with three agar bodies of different shapes. The conductivity of the agar blocks is 6 S/m.	77
4.15	Experimental results for the agar phantom at 30 kHz: (a) measured field profile, (b) reconstructed conductivity distribution profile.	78
4.16	Experimental results for the agar phantom at 60 kHz: (a) measured field profile, (b) reconstructed conductivity distribution profile.	79
4.17	Experimental results for the agar phantom at 90 kHz: (a) measured field profile, (b) reconstructed conductivity distribution profile.	80
4.18	Conductivity spectrum of a potato. If the conductivity of the potato was independent from the frequency and was equal to that was measured at 30 Khz, the measured conductivities were to be equal to the conductivity values shown with a star (*). Since the plots are different it is concluded from the figure that the conductivity of the potato increases as the frequency increases. Data have been normalized with respect to the readings at 30 kHz.	81
B.1	The conductive ring. A z-directed magnetic field applied to a conductive ring of inner radius b and outer radius a. Height of the ring is indicated as h.	96
C.1	Magnetic field measurement using resistive ring experiment setup	99
C.2	Receiver coil output voltage versus conductivity plot obtained by using resistive ring. Mean value of the difference data is plotted as a function of: (a) resistor values, (b) 1/(resistor values) (100 sample are taken for each measurement).	100
D.1	Ideal bandwidth of low-pass and band-pass circuit elements . .	103
D.2	Actual response and equivalent noise bandwidth for low-pass circuit.	103
D.3	Typical op-amp circuit with an absolute gain $A = \frac{R_f}{R_1}$	104

D.4	Typical op-amp circuit (Figure D.3) with the equivalent noise voltage and current sources included; (a) Circuit of Figure D.3 with noise sources added; (b) Circuit of Figure D.4(a) with noise sources combined at one terminal for the case $R_{s1} = R_{s2} = R_s$.	106
-----	---	-----

CHAPTER 1

INTRODUCTION

1.1 Medical Imaging

Medical imaging is used in clinical evaluations to diagnose specific diseases by displaying the distribution of a physical property in human body. Alternatively, it may be used to understand working mechanisms of various organs. Most of these techniques also have industrial applications.

Mathematically speaking, medical imaging usually involves the solution of *inverse problems*. This means that the cause (in this case properties of the living tissue) is inferred from the effect. The effect, in this case, is the response probed by various means. In the case of ultrasonography, the probe is an ultrasonic detector; in the case of radiography, the probe is an X-ray detector.

Radiographs, Fluoroscopy, Computed Tomography (CT), Magnetic Resonance Imaging (MRI) and Ultrasound are the well-known modern imaging modalities [8]. Recently proposed/developed medical imaging modalities are: Diffuse Optical Tomography (DOT) [9], Elastography [10], Electrical Impedance Tomography (EIT)[11], Nuclear Medicine [12], Optoacoustic Imaging [13], Positron Emission Tomography (PET) [14], and Ophthalmology [15].

In this thesis study, the results of a new imaging modality is presented which

uses magnetic means to image electrical conductivity of body tissues. The technique is closely related to its predecessors, proposed about two decades ago, to image electrical impedance of body tissues. Thus, before reporting the results of the new approach, some of these previous methods will be reviewed.

1.2 Electrical Impedance Tomography

Table 1.1 lists the electrical resistivity of different body tissues, showing that different body tissues can be distinguished by using their resistivity properties. Electrical Impedance Tomography uses surface voltage measurements to image the electrical properties (conductivity/permittivity) of the body.

In EIT, currents can be introduced into the subject either by using electrodes or by using magnetic induction. In applied-current electrical impedance tomography (ACEIT), time-varying currents with constant amplitude are injected to the subject via the surface electrodes, and the resultant voltages are measured using the same electrodes [1], [16]- [18] (Fig. 1.1). In induced-current electrical impedance tomography (ICEIT), time-varying magnetic fields, generated by sinusoidal current carrying wires encircling the conducting body, are applied to induce currents in the body and voltage measurements are performed using the surface electrodes [19]- [24] (Fig. 1.2).

Table 1.1: The resistivity of body tissues at low frequencies (20 to 100 kHz [1])

Tissue	Resistivity (Ωcm)
Cerebrospinal Fluid	65
Plasma	66
Blood	150
Liver	350 550
Human Arm	240 (longitudinal) 675 (transverse)
Skeletal Muscle	125 (longitudinal) 1800 (transverse) 150 (longitudinal) 2300 (transverse) 530 (average of above)
Cardiac Muscle	160 (longitudinal) 424 (transverse) 575 (longitudinal) 5181 (transverse) 410 ~ 750 (average of above)
Neural Tissue -gray matter -white matter	580 284 682
Lung	727 ~ 2363 2100 \pm 17 % 1120 1275
Fat	2060 2500 2720
Bone	16600

Some notable features of ICEIT compared to ACEIT are the following:

- The electrodes are used for a single function, i.e., for voltage measurements. Consequently, the voltage sensing electronics can be optimized,
- Internal current level is not limited by the current density at the injection electrodes (it is not limited to the safe current density on the skin where the injection electrodes are attached). It can be enhanced by applying different magnetic field patterns to increase the signal-to-noise ratio in the measurements,
- For a given number of electrodes, the number of independent measurements can be increased by introducing spatially independent magnetic field patterns. In principle, it is possible to manipulate the applied magnetic fields and thus the induced current distribution to examine a particular part of the region in detail.

One disadvantage of induced-current approach is the induced EMF imposed in the measurement cables. However, this effect can be minimized by orienting the cables appropriately with respect to the applied field and keeping them rigidly fixed during the measurements.

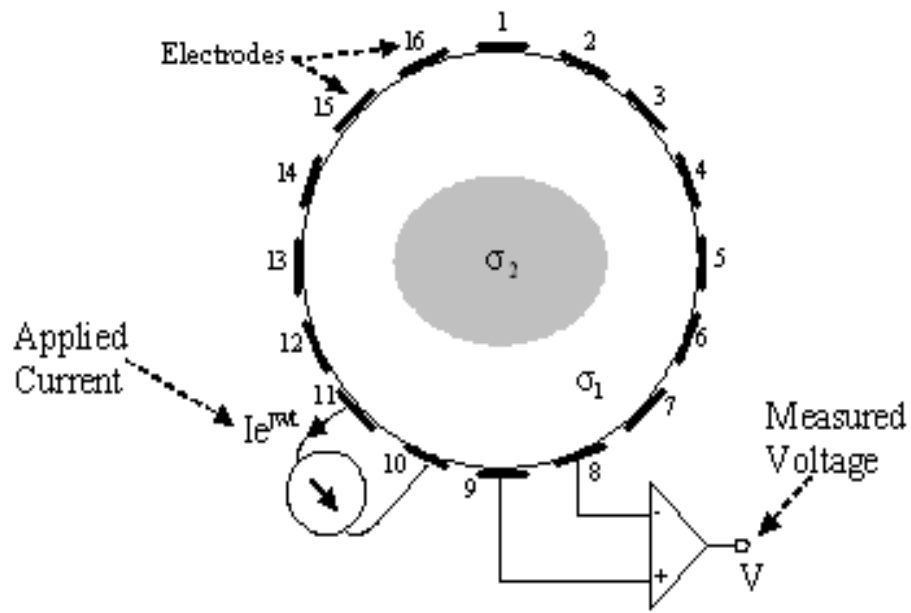


Figure 1.1: The ACEIT measurement system. In this figure; time-varying currents are injected to the subject via the electrode # 10 and the electrode # 11, and the resultant voltage is measured using the electrode # 8 and the electrode # 9

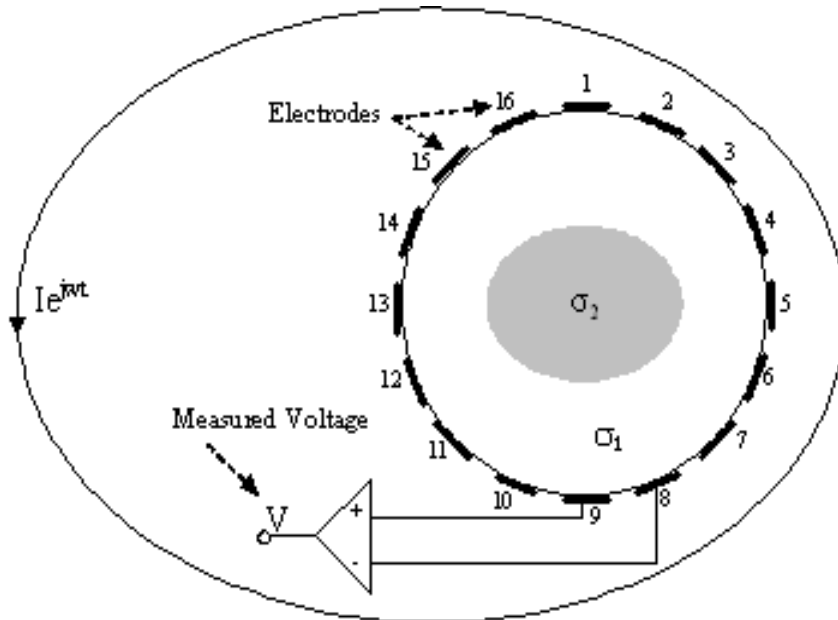


Figure 1.2: The ICEIT measurement system. In this figure; time-varying magnetic fields, generated by sinusoidal current carrying wires encircling the conductive body, are applied to induce currents in the body and the voltage measurements are performed using the electrode # 8 and the electrode # 9

A number of applications were reported for EIT, namely, monitoring lung and thorax function [25], heart imaging [26]-[28], detection of cancer in the skin and breast [29]-[33] and location of epileptic foci[34]. All applications are currently considered experimental and a review of these applications can be found in [35].

In geophysics, the idea dates back to 1930s. A similar technique is employed to locate resistivity anomalies using electrodes on the surface of the earth or in bore holes [36]. In industrial process monitoring, arrays of electrodes are used, for example, to monitor mixtures of conductive fluids in vessels or pipes, or measuring degree of salt content in sea water. The method is also used for nondestructive testing ([37], [38]).

The credit for the invention of EIT as a medical imaging technique is usually attributed to John G. Webster in around 1978 [39], although the first practical realization of a medical EIT system was due to David C. Barber and Brian H. Brown [1].

1.3 Electrical Conductivity Imaging via Contactless Measurements

Figure 1.3 and Figure 1.4 shows different measurement strategies of an alternative method. In that method, a transmitter coil is driven by a sinusoidal current to generate time varying magnetic fields. When a conducting body is brought nearby these coils, eddy currents are induced in the body. The distribution of these currents is a function of the body's impedance distribution. These currents create secondary magnetic fields and the electromotive force induced in a receiver coil is measured using different approaches.

Compared to the EIT techniques mentioned above, this method has the following advantages:

1. There is no physical contact between the body and the measurement system,
2. Currents can be coupled into the body avoiding the screening effects of the superficial insulating layers,
3. The number of measurements can be increased by simply shifting the transmitter and receiver coil array.

The measurement technique is known as *Induction Logging* in geophysics and used for the purpose of geophysical inspection [36]. In process tomography applications, the technique is named as *Mutual Inductance Tomography* or *Electromagnetic Inductance Tomography* [34], [37]. Inspired from the process tomography applications, the method was also proposed for imaging body tissues, and it was termed as *Electromagnetic Imaging* and *Mutual Inductance Imaging* [26], though the proposed method was basically a tomography system.

The usage of magnetic induction-magnetic measurement technique to measure the conductivity of the biological tissues was first proposed by Tarjan and McFee in 1968 [40]. The method was used to determine the average conductivity variation of human torso and head at an operating frequency of 100 kHz employing a differential coil sensor of 13 cm diameter. Single-point measurements following conductivity fluctuations in the human heart are reported [40]. Almost 25 years later, Al-Zeibak and Saunders proposed to use the same method to produce tomographic images of conducting bodies immersed in saline solutions [41]. A small drive-coil (excited at an operating frequency of 2MHz) and a distant pickup-coil is used to scan saline phantoms. The images were reconstructed by employing computational algorithms developed for X-ray CT. The method was named as *Mutual Induction Tomography* (MIT). They reported that fat and fat-free tissues could be distinguished and the internal and external geometry of simple objects can be determined . Around the

same period, Netz et al. employed the same technique with miniaturized coils (25-mm diameter) at an operation frequency of 100 kHz [42]. They reported that the calibration measurements using equal volumes of NaCl solutions of different concentrations show linear dependence on the electrolyte content of the solutions.

Korzhenevskii and Cherepenin (1997) presented a theoretical study of a two-coil arrangement and proposed the direct measurement of phase angle for detecting the eddy currents in the conducting bodies. They applied the filtered backprojection algorithm to the simulated measurements to obtain images [43]. Almost 3 years later, Korjenevsky et al. (2000) reported the implementation of this method [44]. The system employed 16 electronically switched excitation and detection coil units arranged in a circle. The carrier frequency of the system was 20 MHz and this was down-converted to 20 kHz for processing. Demonstration of the imaging of cylindrical objects, with positive and negative conductivity contrast, in a saline bath is given in the same study. The objects, each with diameter 29 % of the array diameter, were clearly resolved using a filtered-back projection algorithm. Korjenevsky and Sapetsky (2000) showed that reduced spatial distortion could be achieved when the images were reconstructed by a neural network for some simple distributions of conductivity [45].

A review of magnetic impedance tomography studies can be found in [46]. There is considerable interest in applying this technique to medical imaging in the last five years:

Scharfetter et al. (2001) implemented a new system that operates at relatively low frequencies (20-370 kHz). The measurement system consists of a solenoid transmitter, a planar gradiometer as a receiver, and a sensitive phase detector [47]. Sensitivity maps of the system are investigated [48], [49] and a fast computation algorithm of sensitivity map is developed [50]. They adopted an existing inverse problem solution [51], which they called 3D inverse eddy

current solution, to reconstruct images, [52].

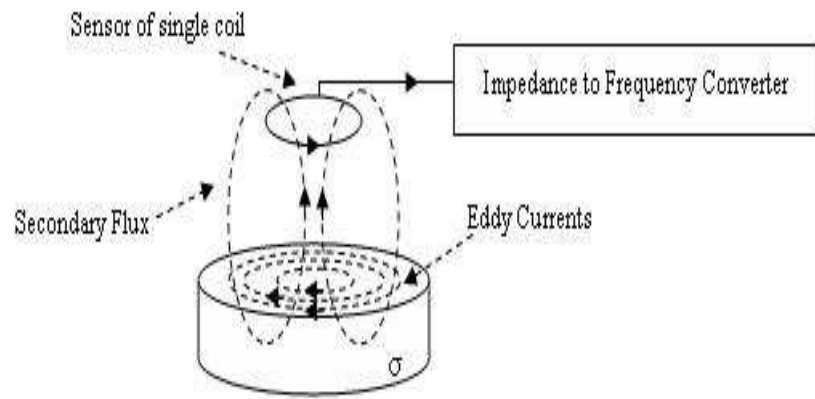
Watson et al. (2004) implemented a new sensor, which in principle, cancels the primary magnetic field by a single receiver, mounted such that no magnetic flux runs through it, instead of using an additional back-off coil [53]. The numerical models and solutions obtained by Morris et al. (2001) [54] are used for simulation studies. The above mentioned sensors are compared with the axial gradiometers [55]. The frequency is selected between 1-10 Mhz. The implementation of this system was demonstrated by Igney et al. (2005) using an array of coils [56].

Independent from the earlier studies, the feasibility of this method was also explored for sub-surface imaging by testing the safety conditions at 50 kHz [57], [58], [51]. Gencer and Tek calculated the pick-up voltages for a miniaturized coil configuration over a uniformly conductive semi-infinite region. Transmitter and receiver coils of radii 10 mm were placed coaxially above the half space (the transmitter and receiver coil distances are 6 cm and 1 cm, respectively). The secondary voltages were about 10 microvolt while the induced currents were well below the safety limit (1.6 mA/cm^2 at 50 kHz). In that study, the effects of displacement currents and propagation effects were also discussed. It was observed that, apart from certain tissues, like heart muscle, kidney, liver and lung, the displacement currents can be assumed negligible for frequencies below 100 kHz. For a survey distance of 20 cm, the % error between the magnitude of the propagation term and unity becomes significant as the frequency increases (7.64% at 100 kHz). Consequently, Gencer *et al.* chose lower frequencies (<100 kHz) to cope with the difficulties arising from both displacement currents and wave propagation delays [58]. They also discussed the safety considerations of the system [51]. To apply the method to realistic body geometries, the forward problem was analyzed by using Finite Element Method (FEM). The inverse problem solutions were obtained using the pseudo-inverse of the sensitivity matrix [51]. In the latter studies, two data

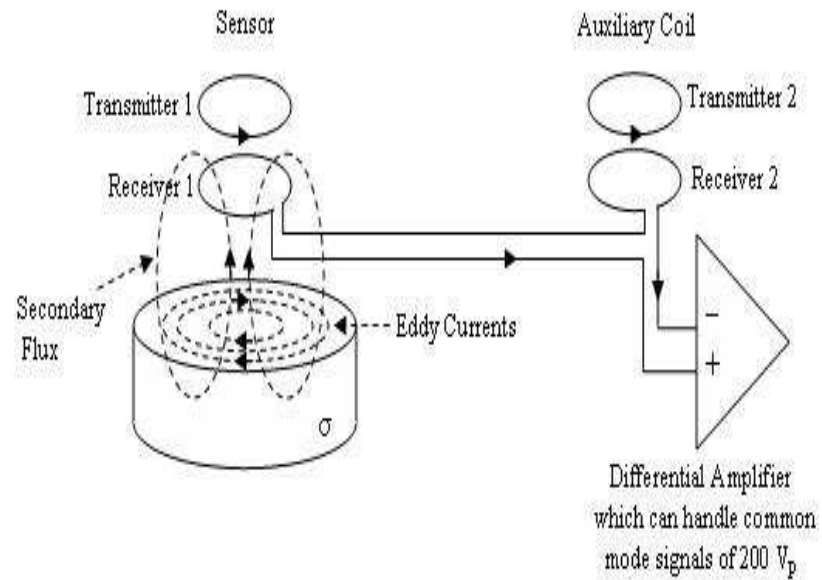
acquisition systems were developed and implemented [2], [59], [60]. The performance of these systems were investigated using saline solution filled glass tubes and biological tissues. Recently, another (improved) data acquisition system operating at 14.1 kHz was developed by Çolak and Gençer [60]. These three implementations will be shortly reviewed next.

In the first implementation, two different measurement methodologies were proposed [3]. The first approach employs a single-coil (Figure 1.3 (a)). In this model, a single sensor is used for both transmitter and receiver. When the conductive object is placed near the sensor, its impedance will change. An impedance-to-frequency converter is used to convert this impedance variations to the square wave whose frequency is a function of the body conductivity. This frequency output is directly connected to a parallel port of a PC. Frequency changes versus concentration of saline solutions (of concentration 10 gr/l to 100 gr/l) was investigated. Changes of 100 Hz output frequency for every 1.9 mS/cm conductivity change was reported at the operation frequency of 1.4 MHz. The details of the measurement system and further information can be found in [3]. The second approach employs two coils (Figure 1.3 (b)). In this approach, there are two different channels for the sensor. One for the reference, and the other for the measurement. Output of these two channels is fed to a differential amplifier. Finally phase sensitive detection (PSD) is employed to the signal at the output of the differential amplifier. The PSD output is converted to digital signal with an analog-to-digital converter (ADC). The ADC output is then fed to the PC. The system operates at 15 KHz. The SNR of the system was reported as 39 dB while the spatial resolution was determined as 9 mm. More detailed information can be found in [3].

In the second implementation, a differential coil sensor was realized and used to scan conduction phantoms by a PC controlled scanning system [61] (Figure 1.4). The data acquisition system was constructed using a PC controlled lock-in amplifier instrument. The operation frequency of the system was 11.6 kHz. The SNR of the system was reported as 34 dB. The conductivity images are re-



(a)



(b)

Figure 1.3: The measurement methodologies proposed by Ahmad and Gençer [2], [3]. (a) Single coil sensor model, (b) Two-coil sensor model.

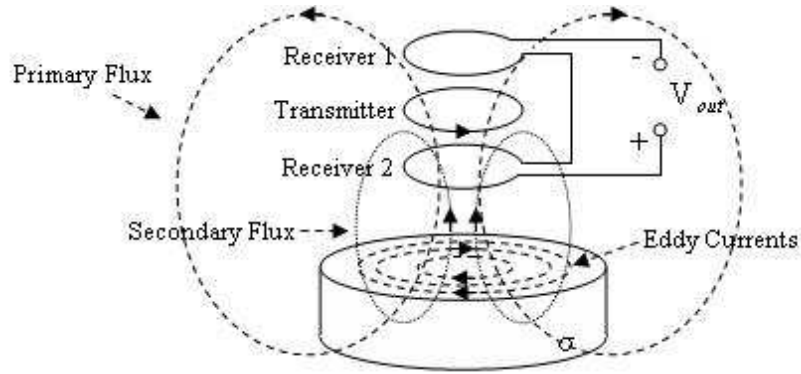


Figure 1.4: The differential coil sensor.

constructed using the sensitivity matrix approach. The spatial resolution was determined as 12.35 mm for agar phantoms and 17 mm for isolated conducting phantoms. The sensitivity of the system is measured as 21.47 mV/(S/m) while the linearity is 7.2% full scale. Also the measured field profile of a biological tissue was reported for the first time in the literature. Thus, the potential of this methodology for clinical applications was shown ([59], [62]). The details of the measurement system and further information can be found in [61].

In the third implementation, the former data acquisition system [61] was improved to obtain measurements with a faster scanning speed. Also a data acquisition card was designed to eliminate the use of the Lock-in instrument in the phase sensitive measurements, thus achieving a portable system. The performance of the system was investigated with a novel test method employing resistor rings. The minimum conductivity value that can be distinguished was determined as 2.7 S/m. Field profiles of agar objects with different geometries were reported. The details of the measurement system and further information can be found in [60].

1.4 Multi-Frequency Studies

The electrical properties of the biological tissues -conductivity and permittivity- are strictly dependent on the operating frequency [63]. As frequency increases, the cell membrane permits the current to pass inside the intracellular fluid. This causes an increase in conductivity values. This phenomena is known as β -relaxation or Maxwell-Wagner dispersion [64]. At this region as frequency increases, the permittivity value decreases (Figure 1.5). Since the change of conductivity differs from tissue to tissue, multi-frequency studies should be investigated.

Previous researches studied on the adopted measurement approach were concentrated on single frequency measurements [61], [3], [60]. In the literature, the feasibility study of multi-frequency studies working in the β -dispersion region was investigated experimentally on biological tissues, and a conductivity spectrum of a potato was determined by Scharfetter *et al.* [47]. This study showed the feasibility of a spectroscopic system and feasibility of on-line monitoring of brain oedema. However, in the literature, the multi-frequency images of an object hasn't been reported yet. To the knowledge of the author the scope of this study is the first in multi-frequency contactless conductivity imaging.

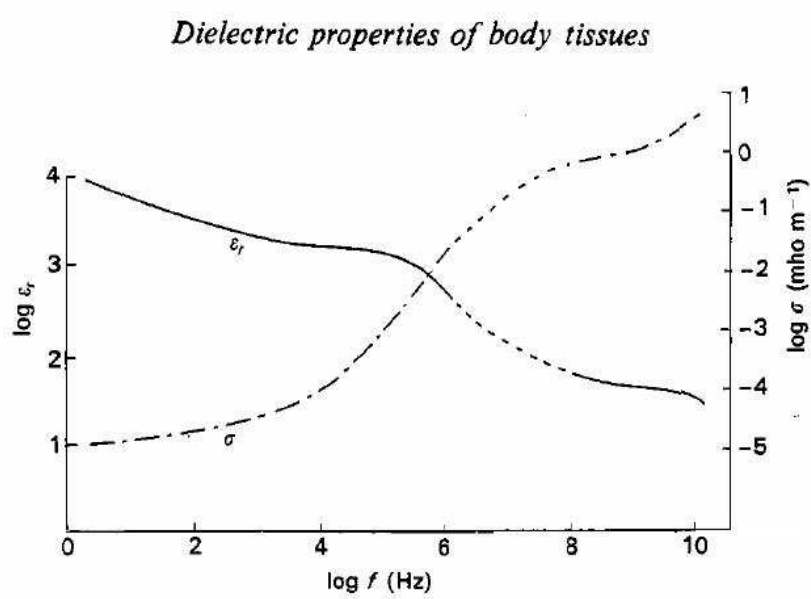


Figure 1.5: Frequency variation of the relative permittivity ϵ_r , and conductivity σ for skin at 37 °C (Schwan 1965 [4], Yamamoto and Yamamoto 1976 [5]).

1.5 Objective of the Study

Objectives of this study are listed as follows:

- To design and develop a prototype system at single frequency. The system should measure very small ac magnetic fields and be capable of phase sensitive detection. The output of the system should change linearly with the conductivity.
- To design and develop a multi-frequency data acquisition system. Necessary hardware should be designed and implemented. The system should distinguish the conductivity variations in the range of biological tissues.
- To perform multi-frequency experiments. There must be a consistency between the results and the theory, i.e. the quality of the images should increase when the frequency increases.
- To obtain field profiles of the phantoms.
- To reconstruct the conductivity profiles of agar objects and biological tissues from the field profiles.

1.6 Outline of the Thesis

After a short introduction on existing conductivity imaging modalities (Chapter 1), the theory behind magnetic induction and magnetic measurement method is discussed and the inverse problem solution method is explained in Chapter 2. In Chapter 3, the hardware details of the data acquisition systems and the data collection, acquisition and analysis software behind them are described. The results are given in Chapter 4. Finally the performance of the system is discussed in Chapter 5.

CHAPTER 2

THEORETICAL BACKGROUND

2.1 Introduction

Figure 2.1 shows the basic measurement principles of electrical conductivity imaging via contactless measurements. This modality uses magnetic excitation to induce currents inside the body and measures the magnetic fields of the induced currents (eddy currents). Thus the measurement system has no physical contact to the conducting body opposed to the other electrical impedance imaging methods. A transmitter coil is driven by a sinusoidal current to provide time varying magnetic fields. When a body is brought nearby these coils, eddy currents are induced in the body. The distribution of these currents is a function of the body's impedance distribution. These currents create secondary magnetic fields and the electromotive force induced in a receiver coil is measured. The theory behind this principle is given in the next section.

2.2 Forward Problem

The *forward problem* of this imaging modality is defined as calculation of the secondary magnetic fields for a known conductivity distribution. The theoretical formulation relating the conductivity to the magnetic measurements was given in [58], [51]. In this thesis report, a review of these formulations will be presented. In the first formulation the *magnetic reciprocity* theorem is used, while in the second formulation the *Biot-Savart* theorem is employed. Note that with simple manipulations, it is possible to reach to one equation by using

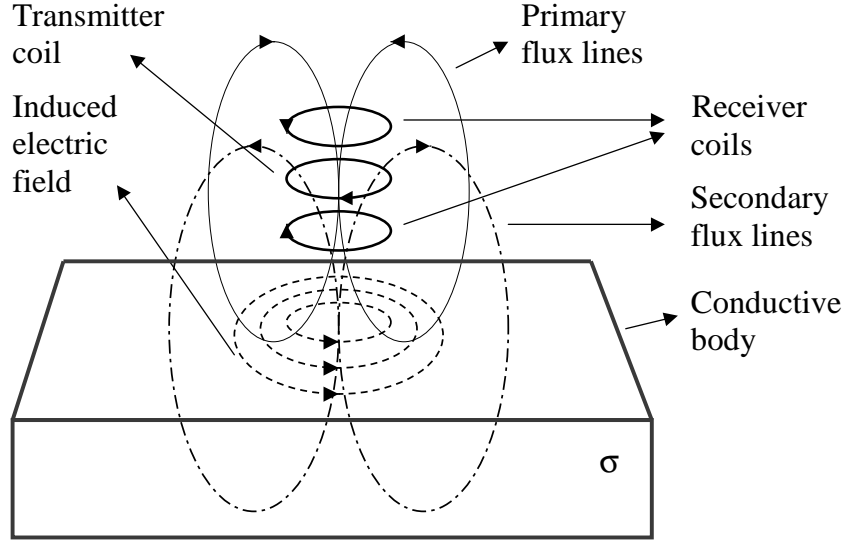


Figure 2.1: General principles of data collection in the magnetic-induction magnetic-measurement system. A transmitter coil is energized with low-frequency sinusoidal currents, generating time-varying magnetic fields. This induces currents in the nearby conductive body. A receiver coil senses the magnetic fields of both primary current in the transmitter coil, and the induced current in the conductive body.

the other.

2.2.1 Calculation of Measurement Sensitivity to Conductivity Distribution Using the *Reciprocity Theorem*

In a linear, isotropic, non-magnetic medium, the electric field has two sources, namely, the time varying magnetic field and the surface and volume charges. For a sinusoidal excitation, the electric field \vec{E} can be expressed as the combination of these two sources:

$$\vec{E} = -\nabla\phi - j\omega\vec{A} \quad (2.1)$$

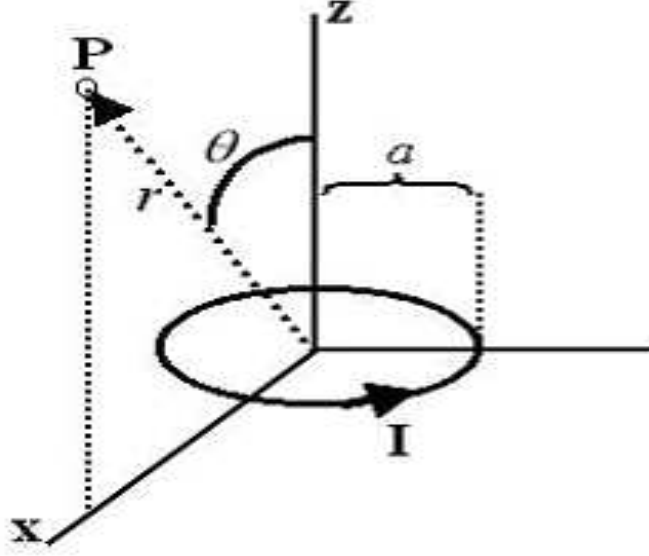


Figure 2.2: Magnetic vector potential at point P created by current carrying loop.

where \vec{A} , ϕ and ω represent the magnetic vector potential, scalar potential and radial frequency respectively. The vector potential term can easily be calculated for a certain coil configuration by assuming 1) the magnetic vector potential generated by the transmitter coil is equal to the primary vector potential \vec{A}_p , and 2) the displacement currents are negligible. The validity of this assumptions is discussed in Appendix A.

Fig. 2.2 shows a circular loop of radius a carrying a current I centered at the origin in the x-y plane. The magnetic vector potential \vec{A} at point P is calculated as [65]:

$$\vec{A}_\phi(r, \theta) = \frac{\mu_0}{4\pi} \frac{4Ia}{\sqrt{a^2 + r^2 + 2arsin\theta}} \frac{(2 - k^2)K(k) - 2E(k)}{k^2} \quad (2.2)$$

where K and E are the elliptic integrals of the first and second kinds, respectively.

Argument k of the elliptic integral is defined as

$$k^2 = \frac{4a \operatorname{arcsin} \theta}{a^2 + r^2 + 2a \operatorname{arcsin} \theta} \quad (2.3)$$

The scalar potential distribution term for the same coil configuration requires the solution of the following differential equation [22], [20]:

$$\nabla \cdot (\sigma \nabla \phi) = -\omega \vec{A}_p \cdot \nabla \sigma \quad (2.4)$$

$$\frac{\partial \phi}{\partial n} = \omega A_{pn} \quad (2.5)$$

where σ denotes the conductivity and \vec{A}_{pn} is the normal component of the magnetic vector potential on the surface of the conductive body. Using the above given assumptions, the scalar potential has only imaginary component. Consequently, \vec{E} can be expressed as

$$\vec{E} = -j (\omega \vec{A} + \nabla \phi) \quad (2.6)$$

The induced current density \vec{J}_i in the conductive object is $\vec{J}_i = \sigma \vec{E}$. This current in the conductive object create a magnetic flux Φ which is picked up by the receiver coil. Using the reciprocity theorem [66], Φ can be calculated using the following integrals in the corresponding volumes [51]:

$$\Phi = \frac{1}{I_R} \oint \vec{A} \cdot \vec{J}_T dV_{Coil} + \frac{1}{I_R} \int \vec{A}_R \cdot \vec{J}_i dV_{Body} \quad (2.7)$$

where \vec{A}_R is the magnetic vector potential created by the reciprocal current I_R in the receiver coil. \vec{J}_T and \vec{J}_i represent the current density in the transmitter coil and the induced current density in the conductive object, respectively. The differential volume elements of the receiver coil and conducting body are

denoted by dV_{Coil} and dV_{Body} , respectively. Note that, the first term on the right is the primary flux, directly coupled from the transmitter coil. The second term represents the flux caused by the induced currents. The electromotive force in the receiver coil can then be expressed as:

$$\begin{aligned}
v &= -j \omega \Phi \\
v &= -j I_T \oint \left(\frac{\omega \vec{A}_{R_1}}{I_{R_1}} \right) \cdot d\vec{l} \\
&\quad - \int \frac{\omega \vec{A}_R}{I_R} \cdot \sigma(\omega \vec{A}_T + \nabla \phi) dV_{Body}
\end{aligned} \tag{2.8}$$

As seen in the above equations, the induced voltage in the receiver coil has two components. The *quadrature* component arises from the transmitter coil current and, under the adopted excitation (low-frequency) conditions, is not affected from the conducting body. Whereas the *in-phase* component directly reflect the conductivity information. The quadrature component is very large compared with the in-phase component and should be cancelled out by some means. In this study, a differentially connected receiver coil is used for that purpose. For identical receiver coils placed at the same distance from the transmitter coil, the differential connection yields an output voltage which can be expressed as given below:

$$v = \int \omega \left(\frac{\omega \vec{A}_{R_1}}{I_{R_1}} - \frac{\omega \vec{A}_{R_2}}{I_{R_2}} \right) \cdot \sigma(\omega \vec{A}_T + \nabla \phi) dV_{Body}. \tag{2.9}$$

Here \vec{A}_{R_1} and \vec{A}_{R_2} are the magnetic vector potentials created by the reciprocal currents I_{R_1} and I_{R_2} , respectively. \vec{A}_{R_1} and \vec{A}_{R_2} can be calculated using Equation (2.2) and (2.3).

2.2.2 Investigating the Relation of Magnetic Flux Density to Induced Currents by Using the *Biot-Savart Theorem*

Assume that the time varying magnetic field is obtained by energizing a transmitter coil with a sinusoidal current. Then, under the quasi-static conditions, the magnetic flux density \vec{B} can be calculated by using the Biot-Savart law:

$$\vec{B} = \frac{\mu_0}{4\pi} \int \frac{\vec{J} \times \vec{R}}{R^3} dV \quad (2.10)$$

Where \vec{J} is the source current density, μ_0 is the free space permeability, R is the distance between the source point in the conductive medium to the field point and V represents conductive medium volume. Since \vec{J} has two sources: 1) current in the transmitter coil (\vec{J}_T), 2) induced currents in the conductive body (\vec{J}_i), note that there is a 90° phase difference between these currents, the magnetic flux density can be expressed as

$$\vec{B} = \frac{\mu_0}{4\pi} \int \vec{J}_T \times \frac{R}{R^3} dV_{Coil} + \frac{\mu_0}{4\pi} \int \vec{J}_i \times \frac{R}{R^3} dV_{Body} \quad (2.11)$$

or

$$\vec{B} = \vec{B}_p + \vec{B}_s \quad (2.12)$$

where \vec{B}_p and \vec{B}_s represents the primary and secondary magnetic fields, respectively. By using the Equation 2.6, \vec{B}_s can be rewritten as

$$\vec{B}_s = -j \frac{\mu_0}{4\pi} \int \sigma (w \vec{A}_t + \nabla \phi) \times \frac{\vec{R}}{R^3} dV_{Body} \quad (2.13)$$

where the μ_0 is the free-space permeability and \vec{R} is the pointing vector from the source point to the field point. In this equation a relation between the \vec{B}_s and the σ can be seen but since $\nabla\phi$ is dependent on the conductivity, the relationship is rather complicated. To overcome this problem a linear variation of $\Delta\vec{B}_s$ with $\Delta\sigma$ can be assumed. Thus, for a certain conductivity distribution σ_0 , the effect of a change in conductivity $\Delta\sigma$ to the field measurements $\Delta\vec{B}_s$ should be formulated. If \vec{B}_s and \vec{B}_{s0} are the magnetic flux densities corresponding to σ and σ_0 then $\Delta\vec{B}_s = \vec{B}_s - \vec{B}_{s0}$. Consequently, by substituting $\phi_0 + \Delta\phi$ and $\sigma_0 + \Delta\sigma$ for ϕ and σ , we obtain

$$\Delta\vec{B}_s = j\frac{\mu_0}{4\pi} \int \frac{\vec{R}}{R^3} \times (w\vec{A}_t + \nabla\phi_0 + \frac{\partial(\nabla\phi)}{\partial\sigma})\Delta\sigma dV_{Body} \quad (2.14)$$

This equation shows the change in magnetic field $\Delta\vec{B}_s$ when a perturbation $\Delta\sigma$ occurs.

2.3 Inverse Problem

The *inverse problem* is defined as calculation of the conductivity distribution from the magnetic field measurements. Since the scalar potential distribution ϕ is a function of the unknown conductivity distribution, the relation between the secondary magnetic field in the detector coil and the conductivity distribution is non-linear. One method to find an estimate of the conductivity distribution from a set of measurements is to linearize (2.9) around an initial conductivity distribution. Using this approach, it is possible to obtain a linear relation between the perturbation in conductivity and the changes in the measurements.

For m measurements, if the conductive body is discretized into n elements (of constant conductivity), it is possible to obtain the following matrix equation [51]:

$$\Delta \mathbf{v} = \mathbf{S} \Delta \sigma \quad (2.15)$$

where $\Delta \mathbf{v}$ is an $m \times 1$ vector representing the perturbation in measurements and $\Delta \sigma$ is an $n \times 1$ vector representing the perturbations in the element conductivities from an assumed conductivity value. The sensitivity matrix \mathbf{S} can be calculated as explained in detail in [51]. Note that calculation of \mathbf{S} requires the solution of the scalar potential distribution for an assumed conductivity distribution. For a body of arbitrary geometry, a numerical method, such as the FEM [51], must be employed for that purpose.

In this thesis study, to obtain a fast estimate of the conductivity distribution, the effects of the $\nabla \phi$ term on the magnetic field measurements are simply neglected. Using this simplification, Equation (2.9) reduces to the following:

$$v = \int \omega \left(\frac{\omega \vec{A}_{R_1}}{I_{R_1}} - \frac{\omega \vec{A}_{R_2}}{I_{R_2}} \right) \cdot \sigma(\omega \vec{A}_T) dV_{Body} \quad (2.16)$$

Thus, one obtains a linear relation between the measurements and the conductivity distribution. In matrix notation, the resultant equation can be expressed as

$$\mathbf{v} = \mathbf{S}' \sigma \quad (2.17)$$

where \mathbf{S}' denotes the coefficient matrix of the simplified equations.

This approach, previously proposed by Ulker and Gencer [59], considerably simplifies the numerical solutions. Reconstructed images using experimental data (see Chapter 4) proves that this approach provides satisfactory estimates while reducing the computation time.

2.3.1 Characteristics of the imaging system

To reveal the characteristics of the imaging system, the coefficient matrix is analyzed using the Singular Value Decomposition (SVD) technique. In this subsection, the SVD technique will be reviewed first. The characteristics of the imaging system will then be presented using the SVD tools.

If \mathbf{A} is an $m \times n$ matrix with $m > n$, then \mathbf{A} can be written using the so-called singular value decomposition of the form

$$\mathbf{A} = \mathbf{U}\mathbf{\Sigma}\mathbf{V}^T \quad (2.18)$$

where \mathbf{U} is an $m \times m$ orthonormal matrix and \mathbf{V} is an $n \times n$ orthonormal matrix. $\mathbf{\Sigma}$ is an $m \times n$ diagonal matrix such that

$$\mathbf{\Sigma} = \text{diag}(\sigma_1, \dots, \sigma_r) \quad (2.19)$$

where $r = \min(m, n)$ and $\sigma_1 \geq \dots \geq \sigma_r \geq 0$.

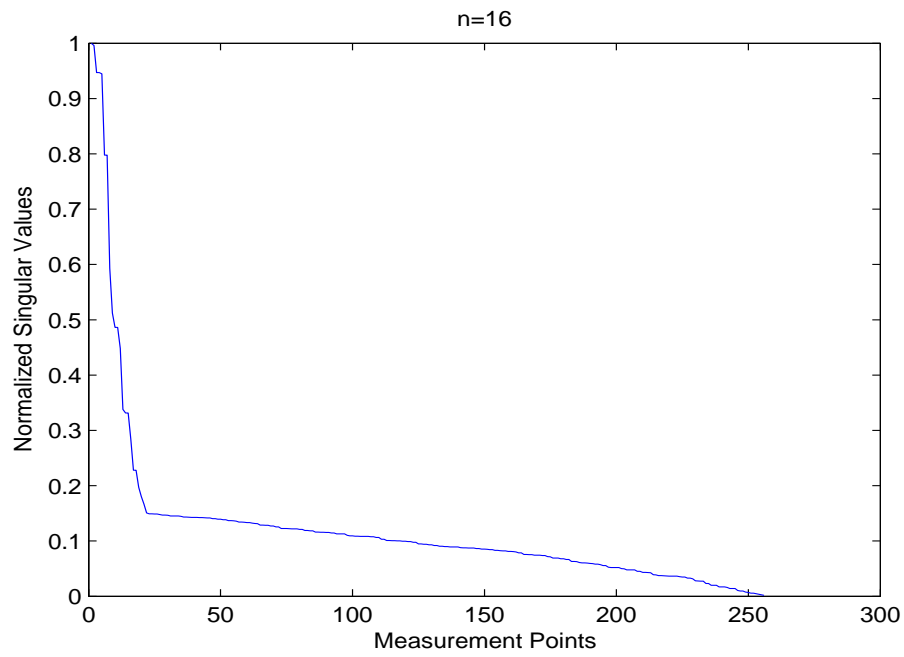
σ_k is called the k^{th} singular value of \mathbf{A} . The first r columns of \mathbf{V} and \mathbf{U} are the right- and left-singular vectors and r denotes the rank of \mathbf{A} [67]. The condition number is the measure of the *singularity* of a matrix and is defined as

$$\kappa = \frac{\sigma_{max}}{\sigma_{min}} \quad (2.20)$$

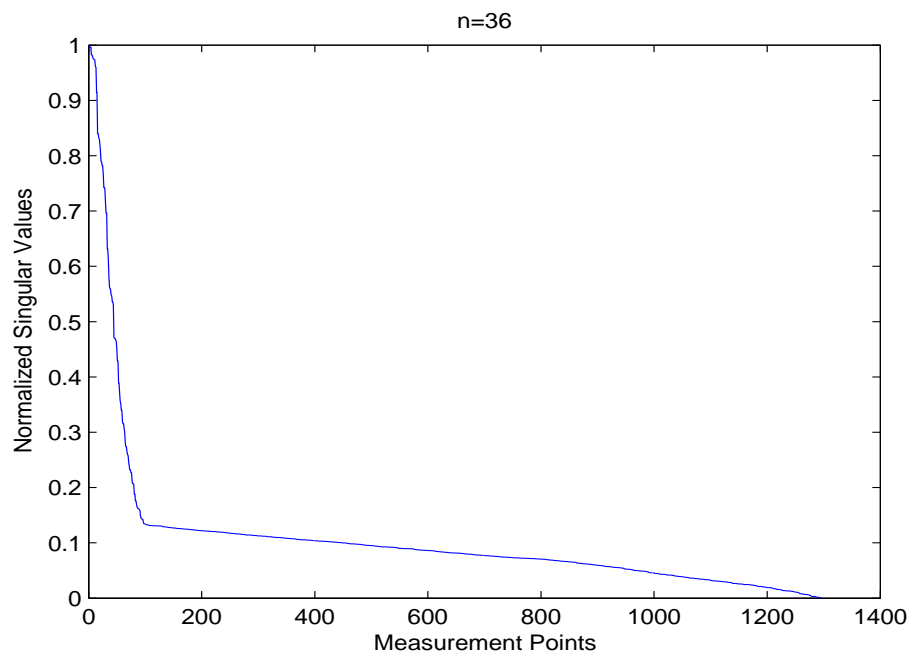
where σ_{max} and σ_{min} are the maximum and minimum singular values, respectively.

Figure 2.3 shows the singular value decay pattern of \mathbf{S}' for different number of measurements (m) and different number of pixels (n) in the image domain. Figure 2.3(a) and (b) show the decay pattern for \mathbf{S}' of dimensions 16×16 and 36×36 , respectively. It is observed that, in both cases, there is a break point after a specific singular value.

To understand the characteristics of the imaging system the right singular vectors of \mathbf{S}' are displayed. Figure 2.4 shows four right singular vectors (basis functions) corresponding to higher singular values. Figure 2.5 shows four right singular vectors corresponding to lower singular values. It is observed that as the basis function number increases, the high frequency terms become more apparent. Therefore, the quality of images, reconstructed with these high frequency terms will be poor.

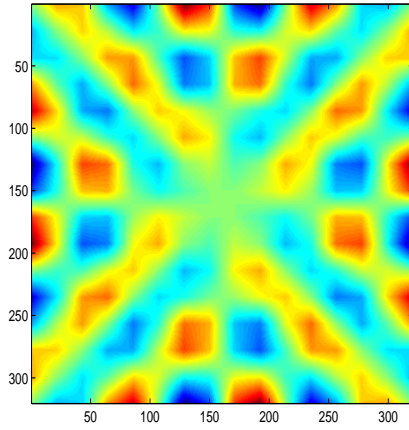


(a)

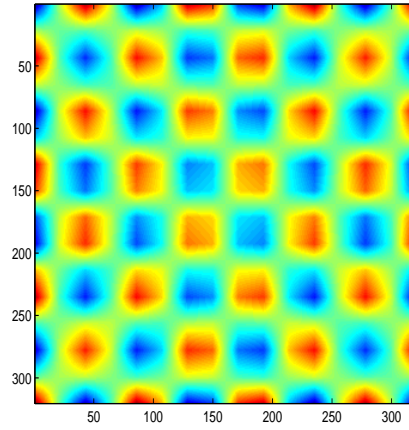


(b)

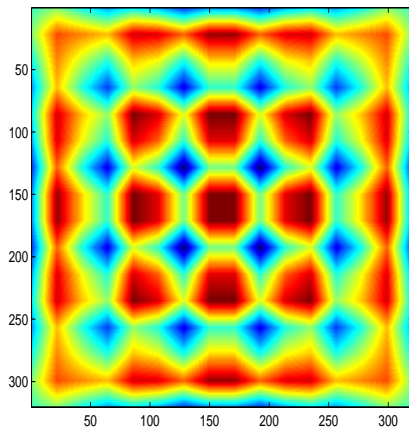
Figure 2.3: Singular values of \mathbf{S}' normalized with the highest singular value. (a) $n = 256$ and $m = 256$, $\kappa = 719.6$, (b) $n = 1296$ and $m = 1296$, $\kappa = 2.3 \times 10^3$.



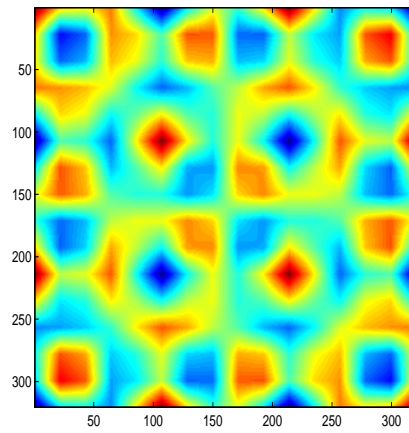
(a) 224th basis function



(b) 241th basis function

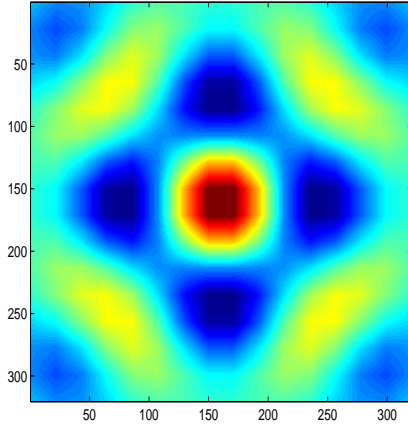


(c) 250th basis function

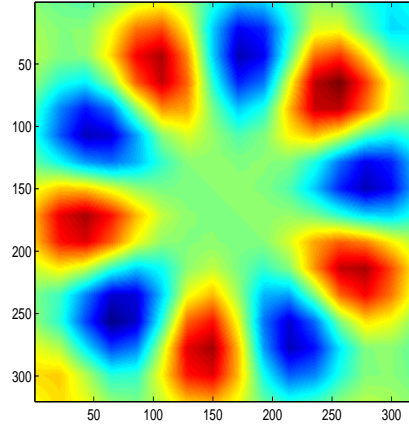


(d) 256th basis function

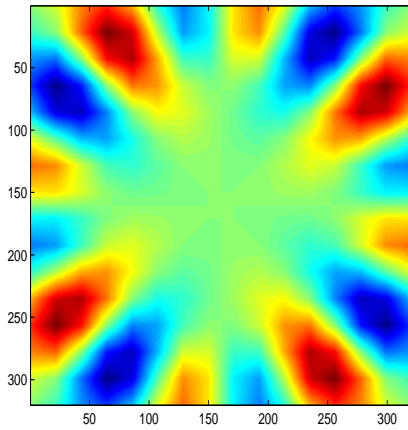
Figure 2.4: Display of the right singular vectors corresponding to higher singular values.



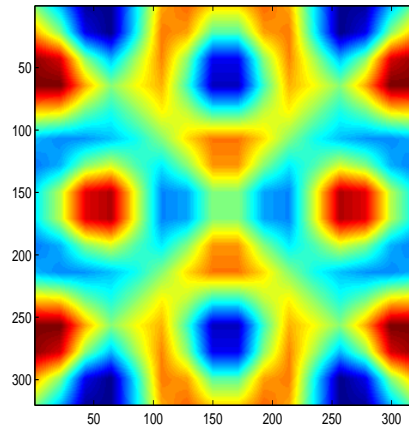
(a) 1st basis function



(b) 10th basis function



(c) 20th basis function



(d) 30th basis function

Figure 2.5: Display of the right singular vectors corresponding to lower singular values.

2.3.2 The Steepest Descent Algorithm

In this thesis study, the steepest descent algorithm is used to solve the inverse problem. This algorithm is one of the most fundamental procedures used for minimizing a differentiable function of several variables. It always converges to a local minimum, but convergence might be slow. In this section, this algorithm will be summarized.

Given a point \mathbf{x} , the steepest descent algorithm proceeds by performing a line search along the direction $-\nabla f(\mathbf{x}) / \|\nabla f(\mathbf{x})\|$ or, equivalently, along the direction $-\nabla f(\mathbf{x})$.

To implement the steepest descent algorithm a computer code is written in MATLAB by using the following algorithm [68]:

- **Initialization Step** Let $\varepsilon > 0$ be the termination scalar. Choose a starting point \mathbf{x}_1 , initialize the iteration number $k=1$, and go to **Main Step**.
- **Main Step** If $\|\nabla f(\mathbf{x}_k)\| < \varepsilon$, stop; otherwise, let $\mathbf{d}_k = -\nabla f(\mathbf{x}_k)$, and let λ_k be the optimal solution to the problem of minimizing $f(\mathbf{x}_k + \lambda \mathbf{d}_k)$ subject to $\lambda \geq 0$. Let $\mathbf{x}_{k+1} = \mathbf{x}_k + \lambda_k \mathbf{d}_k$, replace k by $k+1$, and repeat the **Main Step**.

Here $\mathbf{f}(\mathbf{x})$ is:

$$f(\mathbf{x}) = \frac{1}{2} \|\mathbf{S}\mathbf{x} - \mathbf{v}\|^2. \quad (2.21)$$

$\nabla f(\mathbf{x}_k)$ and λ_k are:

$$\nabla f(\mathbf{x}_k) = \mathbf{S}^T \mathbf{S} \mathbf{x}_k - \mathbf{S}^T \mathbf{v} \quad (2.22)$$

and

$$\lambda_k = \frac{(\mathbf{S}\mathbf{x}_k - \mathbf{v})^T \mathbf{S} \mathbf{S}^T (\mathbf{S}\mathbf{x}_k - \mathbf{v})}{\nabla f(\mathbf{x}_k)^T \mathbf{S}^T \mathbf{S} \nabla f(\mathbf{x}_k)} = \frac{\nabla f(\mathbf{x}_k)^T \nabla f(\mathbf{x}_k)}{\nabla f(\mathbf{x}_k)^T \mathbf{H} \nabla f(\mathbf{x}_k)} \quad (2.23)$$

respectively. Here, \mathbf{H} is an $n \times n$, symmetric, positive definite Hessian matrix. The starting point \mathbf{x}_1 is chosen as $\mathbf{0}$.

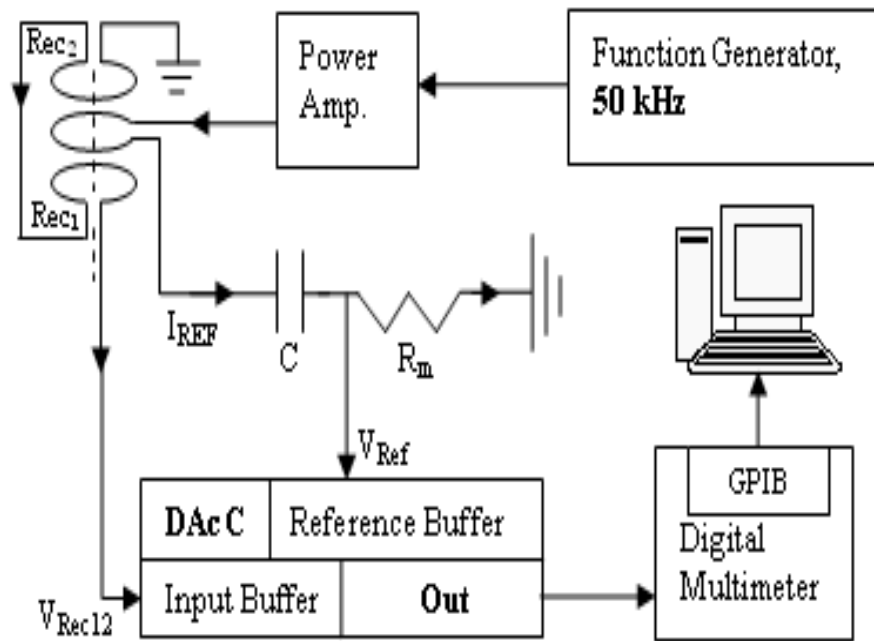
CHAPTER 3

EXPERIMENTAL SETUP

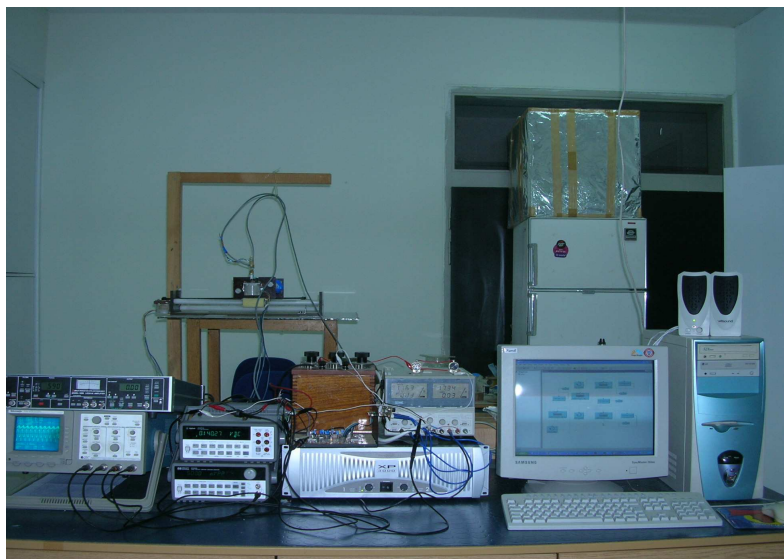
3.1 Data Collection System

3.1.1 Basic Operation Principle

The block diagram and the appearance of the data acquisition system is shown in Figure 3.1. The operation principle is the following: the power amplifier, fed by the function generator, excites the transmitter coil. This induces a voltage on the receiver coils. The receiver coils are identical and differentially connected, thus, in the absence of the conductive body, the sensor output V_{Rec12} is approximately 0 V. However further cancelation is required due to the mismatch of the receiver coils. This cancelation is performed by using a phase shifter circuit assembled on a printed circuit board with the phase sensitive detection (PSD) circuit. The PSD circuit has 2 inputs, one is for the reference and the other one is for the receiver coils. The PSD circuit converts the phase difference between the transmitter and receiver coil signals to a voltage. When the object is brought nearby the sensor, this results a phase shift at the receiver coil output. The degree of the phase shift is related with the conductivity of the object. Thus, by measuring the resultant voltage, it is possible to obtain the conductivity information of the object under study. In this study, the voltage is measured using an Agilent 34401A Voltmeter and a Acquitex CM-2251 Data Acquisition Card. The details of the blocks of the data acquisition system will be explained in the following subsections.



(a)



(b)

Figure 3.1: The block diagram and appearance of the data acquisition system: (a) The block diagram of the system, (b) The appearance of the system.

Table 3.1: Technical specifications of HY60

Parameter	Value
Frequency Response (-3dB)	15 kHz - 50 kHz
Total Harmonic Distortion @1kHz	< 0.015 %
Signal to Noise Ratio	100 dB
Slew Rate	15 V / μ S
Rise Time	5 μ S
Input Sensitivity	500 mV rms
Input Impedance	100 Kohms
Load Impedance	8 - ∞ ohms
Damping Factor (8ohms @ 100Hz)	> 400

3.1.2 Power Amplifier

Two different power amplifiers are employed to excite the two systems, namely, the prototype system operating at 50 kHz and the multi-frequency system. HY60 Bipolar Power Amplifier by ILP Electronics is employed for the prototype system and XP3000 2800 Watts Power Amplifier by Phonic is employed for the multi-frequency system.

The operating voltage of the HY60 Power Amplifier is up to $\pm 25V$. In the prototype system, the power amplifier is fed with $\pm 17.5V$ from a DC power supply (Farnell PDD3010A). The power amplifier is capable of driving a minimum 8Ω load and can deliver 30W of power into a 8Ω load with 0.015% distortion. The sine wave feeding the power amplifier input is produced by the Agilent 34401A Function Generator. The specifications of the HY60 power amplifier is given in Table 3.1.

The XP3000 power amplifier is fed with 220 Volts, 50 Hz AC from the mains. It has two independent output channels. These two channels can be connected in series, in case more is power required. The power amplifier is capable of driving a 8Ω load and can deliver 600W of sine wave power into a 8Ω load with 0.03% distortion (20 times more power than HY60). The sine wave feeding the power amplifier input is produced by the Agilent 34401A Function Generator. The specifications of the XP3000 power amplifier is given in Table 3.2.

Table 3.2: Technical specifications of XP3000

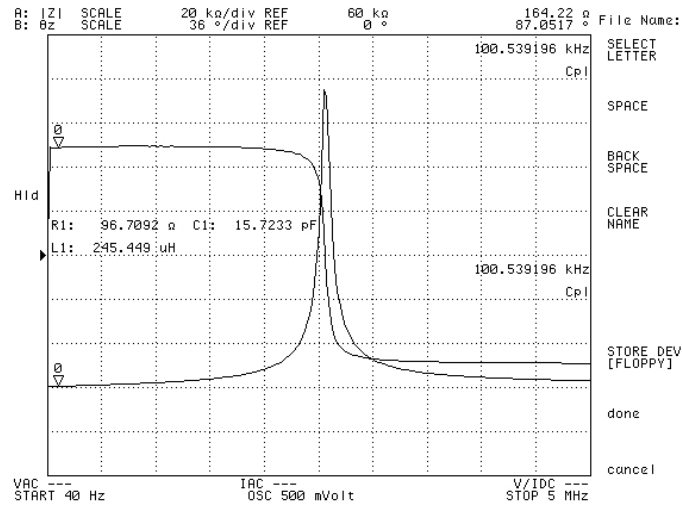
Parameter	Value
Frequency Response (-3dB)	5 Hz - 100 kHz
Total Harmonic Distortion	< 0.02 %
Signal to Noise Ratio	107 dB
Input Sensitivity	1.23 V rms
Input Impedance	20 Kohms
Load Impedance	2 - ∞ ohms
Damping Factor (@ 8ohms)	> 500

3.1.3 Coils

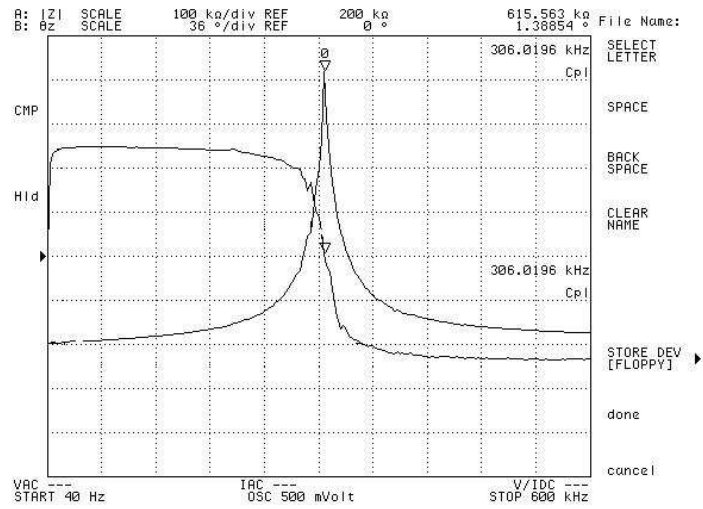
In this study, magnetic excitation (primary field) is used to induce eddy currents inside the conductive body and the resulting magnetic field due to these currents (secondary field) is measured. For this purpose, two differential-coil sensors are employed: one is for the prototype system and the other one is for the multi-frequency measurements. Geometrically the coils are same, the only difference between them is the radius of the wires wound on them. The sensor consists of two differentially connected identical receiver coils employed to measure the secondary field. In between the receiver coils, a transmitter coil is placed, which creates the primary field. All coils are placed coaxially. The delrin rods that the coils are wrapped on is a nonconductive material. Their inner thickness is 6 mm and the sidewall thickness is 1mm. They are placed face to face giving a total sensor height of 24 mm. Two imaging system has been realized in the scope of this thesis. Thus two different sensors with different properties (coil diameter, number of turns etc.) are used. The properties of the two sensors are explained in the following two subsections.

3.1.3.1 Characteristics of the prototype system sensor

The properties of the sensor used in the prototype system is given in Table 3.3. The impedance as a function of frequency graph is also shown in Figure 3.2. A sinusoidal current of 300 mA(peak) at 50 kHz flows in the the transmitter coil fed by an HY60 power amplifier (1.5MW, 0.01% total harmonic distortion). A capacitor of 6 nF is connected in series with the transmitter coil to cancel out the inductance of the transmitter coil.



(a)



(b)

Figure 3.2: Impedance as a function of frequency characteristic of the sensor used in the prototype system, (a) The transmitter coil characteristic (the resonance frequency is 2.55 MHz), (b) The differentially connected receiver coils characteristic (the resonance frequency is 306.02 kHz).

Table 3.3: Coil Properties of the single-frequency prototype system

	transmitter	receiver
number of turns	80	650
DC resistance	0.51 ohm	90.87 ohm
diameter	0.75 mm	0.20 mm
resonance frequency	2.55 MHz	306.019 kHz

Table 3.4: Coil Properties of the multi-frequency system

	transmitter	receiver
number of turns	70	350
DC resistance	0.84 ohm	20.5 ohm
diameter	0.6 mm	0.30 mm
resonance frequency	3.225 MHz	675.013 kHz

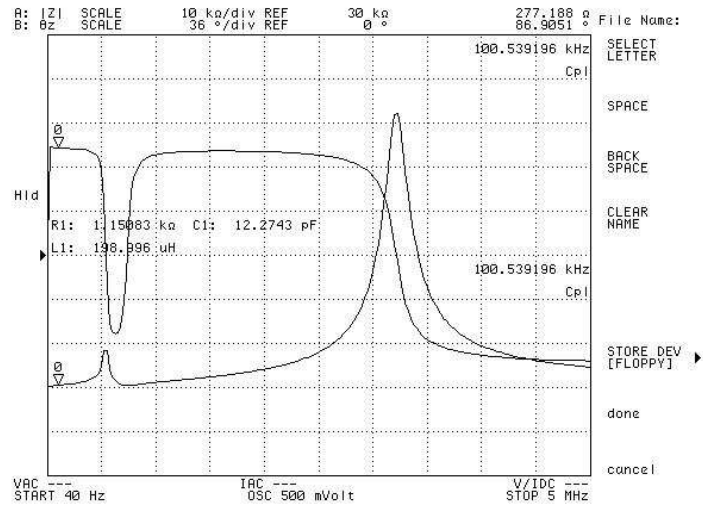
3.1.3.2 Sensor for the multi-frequency system

The properties of the sensor used in the multi-frequency system is given in Table 3.4 and the impedance as a function of frequency graph is shown in Figure 3.3. The transmitter coil is fed by the XP3000 2800 Watts power amplifier. Different capacitors are employed in series with the transmitter coil to cancel out the inductance of the transmitter coil for each operation frequency (Table 3.5).

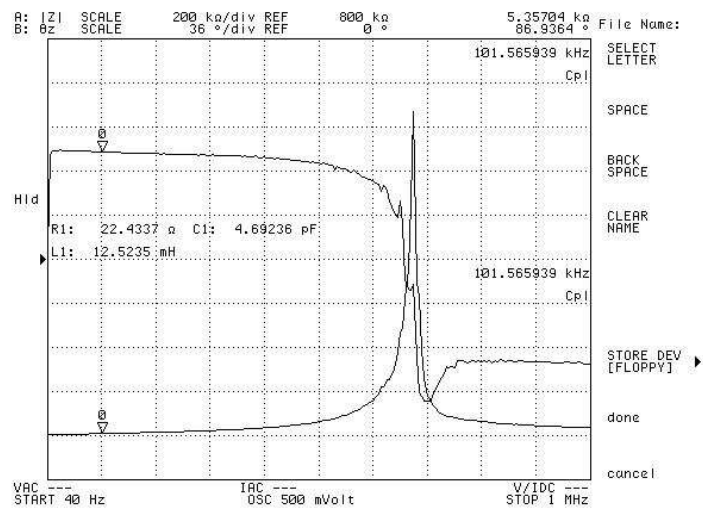
3.1.4 Phase Sensitive Detection

3.1.4.1 Introduction

In the absence of the conductive object (i.e., $\sigma = 0$ S/m), the only source of the magnetic field is the current in the transmitter coil. Thus, the induced voltages (V_{REC1} , V_{REC2} in Fig. 3.1(a)) in the receiver coils are due to the primary field and are purely imaginary. The magnitude of V_{REC1} and V_{REC2} is on the order of 100 V. These are canceled out as a result of the differential connection (i.e., to produce $V_{REC12} = V_{REC1} - V_{REC2}$). It should be noted that real part of $V_{REC1,2}$ in equation [2.8] is also 0 V since $\sigma = 0$ S/m. Thus, V_{REC12} is expected to be 0 V for the perfectly matched receiver coils.



(a)



(b)

Figure 3.3: Impedance as a function of frequency characteristic of the sensor used in the multi-frequency system, (a) The transmitter coil characteristic (the resonance frequency is 3.225MHz), (b) The differentially connected receiver coils characteristic (the resonance frequency is 675.013 kHz).

Table 3.5: Capacitors employed in series with the transmitter coil to cancel out the inductance of the coil in the multi-frequency system

Operation Frequency (kHz)	Capacitor Value (nF)
30	60
50	22
60	15
90	7

In this thesis study, however, an imaginary residual voltage of 10 V (i.e., $Im\{V_{REC12}\} = 10$ V), which leads the reference signal, approximately, by 90° . This originates from the mismatch in the receiver coils. Phase sensitive detection (PSD) is employed in the data acquisition card (DAcC) to cancel out this undesired residual signal. The theory of the PSD is given in subsection 3.1.4.2. The operation principle of the DAcC is explained in subsection 3.1.4.3.

3.1.4.2 Basics of Phase Sensitive Detection

Assuming two cosines, $A\cos(\omega_0t + \phi)$ (the input signal) and $\cos(\omega_0t)$ (the reference signal), the PSD is simply low pass filtering the multiplication of these two signals. In such a way, the phase difference and the amplitude information of the former signal can be extracted.

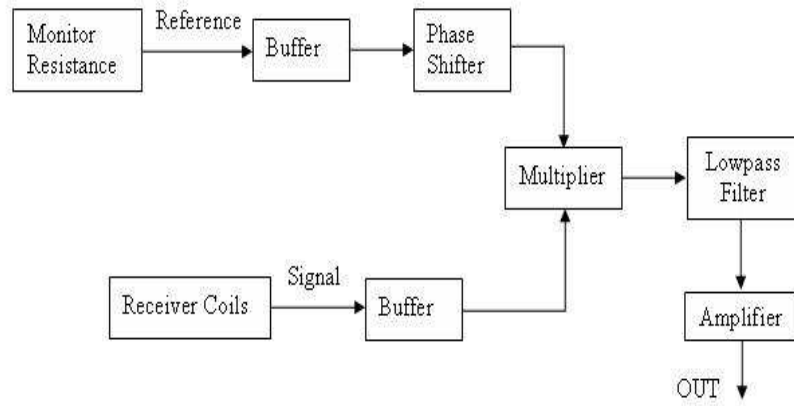
A trigonometric identity yields,

$$A\cos(\omega_0t + \phi) \times \cos(\omega_0t) = \frac{1}{2}A \times \cos(\omega_0t + \phi) + \frac{1}{2}A \times \cos(\phi) \quad (3.1)$$

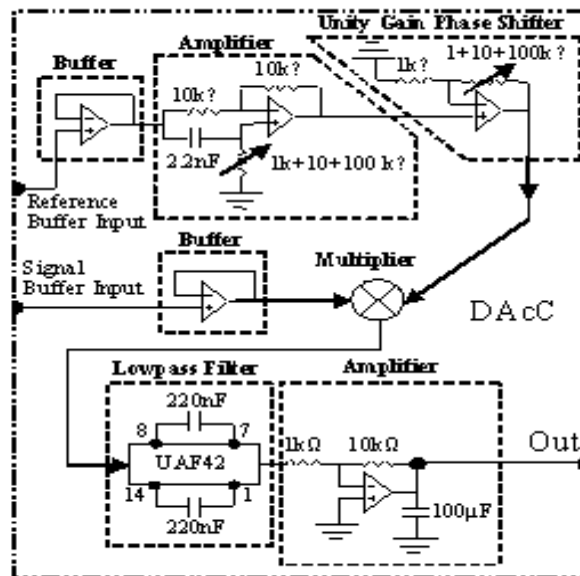
resulting in a high frequency term ($2\omega_0$) and a DC offset. The high frequency term is eliminated by employing a low pass filter. The remaining DC term, $\frac{1}{2}A \times \cos(\phi)$, includes the phase (ϕ) and magnitude (A) information.

3.1.4.3 The Data Acquisition Card

To achieve a phase sensitive detection, a Low Pass Filter (LPF) and a phase shifter circuit is designed and implemented on a Printed Circuit Board (PCB). The PCB is named as, simply, the Data Acquisition Card (DAcC). The block diagram representation of the DAcC is shown in Figure 3.4(a) and detailed representation of the DAcC is shown in Figure 3.4(b). The details of the blocks in the DAcC are shown and explained in Figure 3.5 - Figure 3.10.



(a)



(b)

Figure 3.4: The Data Acquisition Card (DAcC), (a) block diagram representation, (b) detailed block diagram representation.

The operation principle of the DAcC is the following: In the DAcC, voltage on the monitor resistor R_M (the reference signal) is buffered. After amplification, phase calibration is done on the buffered reference signal. Output of the phase shifter is multiplied with the buffered input signal (V_{REC12}) using an AD633 Multiplier. A low pass filter (UAF42) with a cut-off frequency of 1 Hz is employed at the output of the multiplier to extract the in-phase signal. Cut-off frequency of the filter is diminished by means of shunting external 220 μF capacitors with the internal capacitors of the filter IC. Then, the in-phase component of V_{REC12} (i.e., $Re\{V_{REC12}\}$) is obtained at the output of the filter. Finally, it is seen from Eq.[2.9] that the in-phase component of the signal contains the conductivity information of the object under study. Since the measured voltage due to conductive object is small with respect to the residual voltage, the residual voltage should be further canceled when there is no conductive body in the medium. This cancelation is achieved by a minor adjustment (i.e., phase shift of 2-3 degrees) on the phase of the reference signal by using the phase shifter. Thus, approximately 0V is obtained at the filter output. Phase shifter setting is kept untouched in the rest of the experiment. Thus, a residual signal of (10 V) is almost eliminated in the PSD application, whereas the in-phase component of V_{REC12} developed due to the conductive body is still measurable. The filter output is amplified. The gain of the amplifier can be changed depending the resistor values in the circuit. The filtered signal is the output of the DAcC.

The DC signal at the output of the DAcC is measured by an Agilent 34401A multi-meter and also by an Acquittek CM-2251 Data Acquisition Card. The data received from the measurement devices is acquired in a PC.

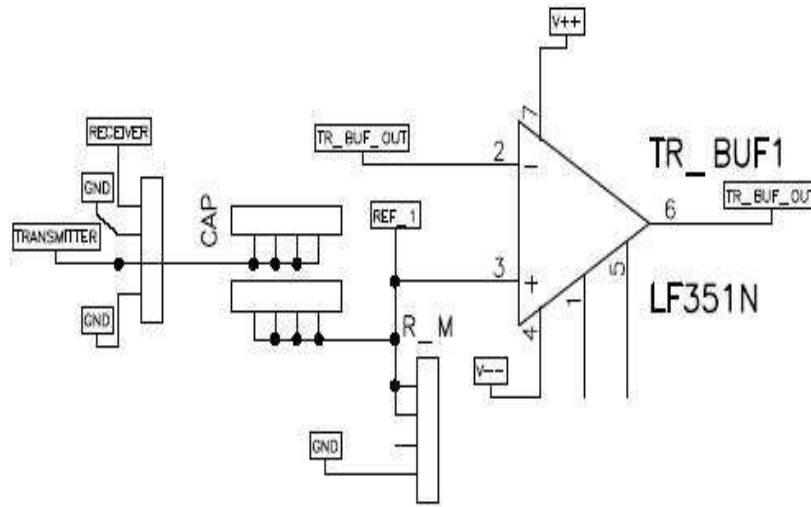


Figure 3.5: Transmitter Coil Current Buffer. Transmitter coil current entering the DA_cC at 'TRANSMITTER' flows through the capacitor connected between the sockets indicated as CAP and then passes from the monitor resistor in *R_M* socket and flows to the ground. Voltage on the monitor resistance (*REF_1*) is taken as the reference voltage and is buffered. The buffer output (*TR_BUF_OUT*) is connected to the input of the amplifier circuit (Figure 3.6).

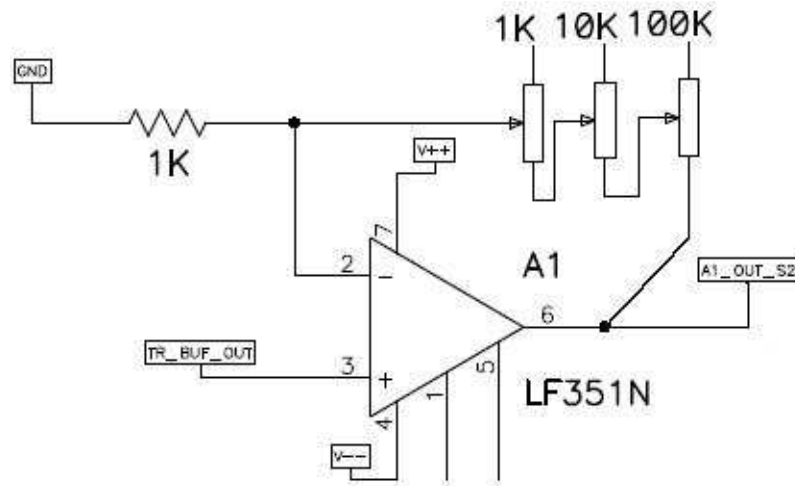


Figure 3.6: Amplifier (A1 circuit) connections. Its input is the buffered monitor resistor (*R_M*) voltage *TR_BUF_OUT* (Figure 3.5). Total amplification factor of *111 is available with this configuration without any instability. Output of the amplifier is connected to the input of the phase shifter circuit (Figure 3.7).

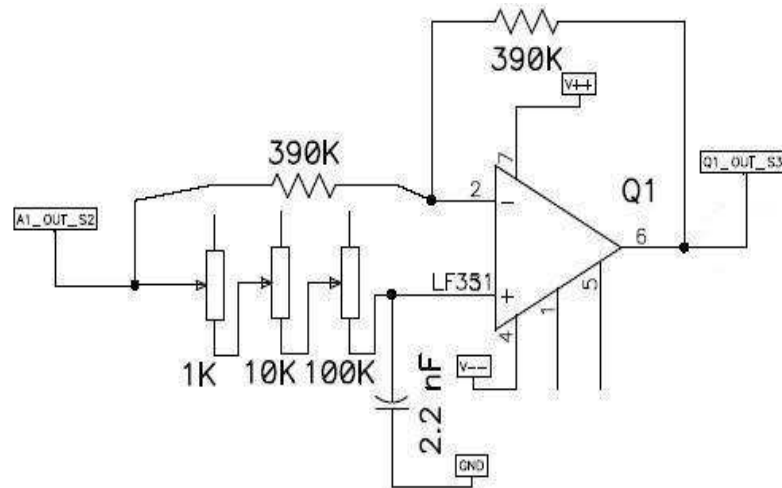


Figure 3.7: Phase shifter (PS) circuit. Its input is the buffered & amplified monitor resistor (R_M) voltage $A1_OUT_S2$ (Figure 3.6). In the phase shifter blocks switching the positions of the 2.2 nF capacitor and the 1+10+100 $k\Omega$ potentiometers results in the phase shifter a phase lag or phase lead circuit. Output of the PS is connected to the input of the multiplier (Figure 3.9).

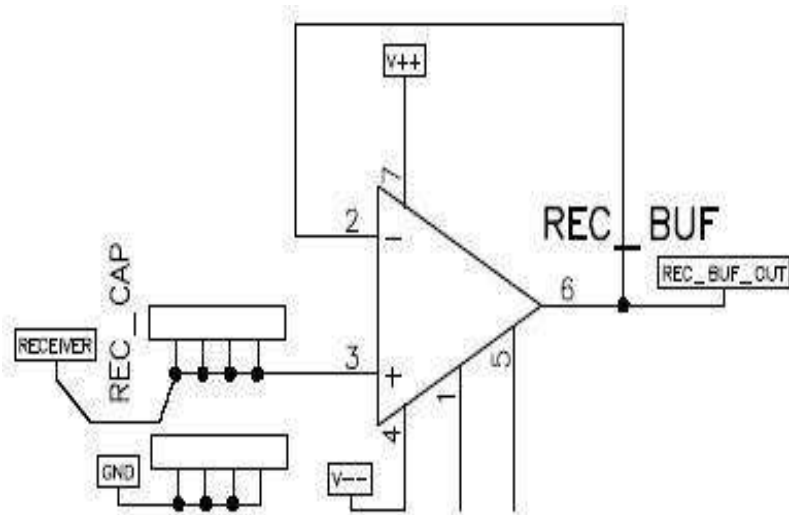


Figure 3.8: Receiver coil signal buffer circuit connections. Output of the differentially connected coils is given to the DAC via RECEIVER channel (Figure 3.5). Socket block named as REC_CAP is available in case capacitors between V_+ input of the buffer and ground are needed to load the receiver coils. The output of the buffer is connected to the input of the multiplier (Figure 3.9).

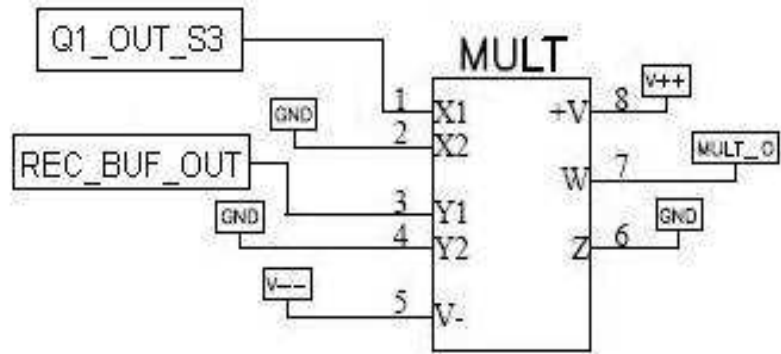


Figure 3.9: Multiplier circuit connections. AD633 is employed to multiply the buffered reference voltage and buffered receiver coil signal which are available at *Q1_OUT_S3* (Figure 3.7) and *REC_BUF_OUT* (Figure 3.8), respectively.

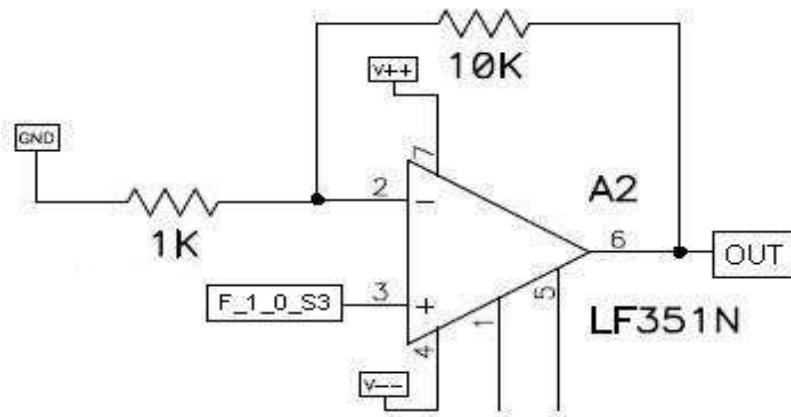
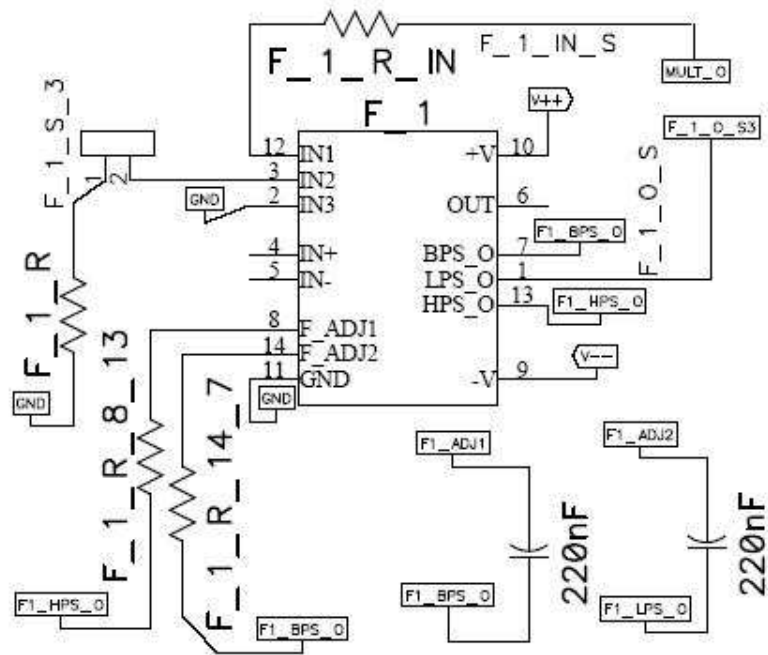


Figure 3.10: Amplifier circuit connections. Total amplification factor of *100 is available with this configuration without any instability.



(c)

Figure 3.11: Low Pass Filter circuit connections. Input to this circuit, comes from the output of the multiplier shown as *MULT_O*. To decrease the cutoff frequency of *F_1*, external 220 nF capacitors are connected in parallel to the internal 1000 pF capacitors buried in the filter IC [6] (Pages 1 and 6). The output of the multiplier (*F_1_0_S3*) is connected to the input of the Amplifier (Figure 3.10)

3.2 XY Scanner System

To scan the probe over the phantom a computer controlled XY scanning system, designed and implemented in [61] and improved in [60], is used. Since the measurement system is sensitive to conductive materials, to avoid artifacts the scanner should be made of non-conductive materials. Delrin, a non-conductive material, is employed to make the scanner system except the step motors. The probe motion is controlled by two step motors, which are controlled by a step motor driving circuit that is fed by a PIC16F877 micro-controller (μC). Thus, the circuitry is composed of two parts:

1. PIC16F877 μC producing the necessary digital signals for the step motor driver circuit.
2. The main driver circuit.

The μC communicating with PC via RS-232 communication protocol. One of the two serial ports of the PC is used for this purpose. Consequently, the XY scanning system is controlled with a PC. HP VEE based user interface program is prepared to control the XY scanner system and to collect measurement data (Section 3.3.1.1). Since direction of the motion is two-dimensional (2D), there are two step motors (one for X movement and one for Y movement). Thus, two driver circuits working in synchrony are required. The synchronization is achieved with the software (Section 3.3.1.1).

The scanning system has a minimum step size of 0.3 mm. The average data acquisition time (scanning and recording the output) for 100 samples is calculated as 0.2893 *sec/mm*².

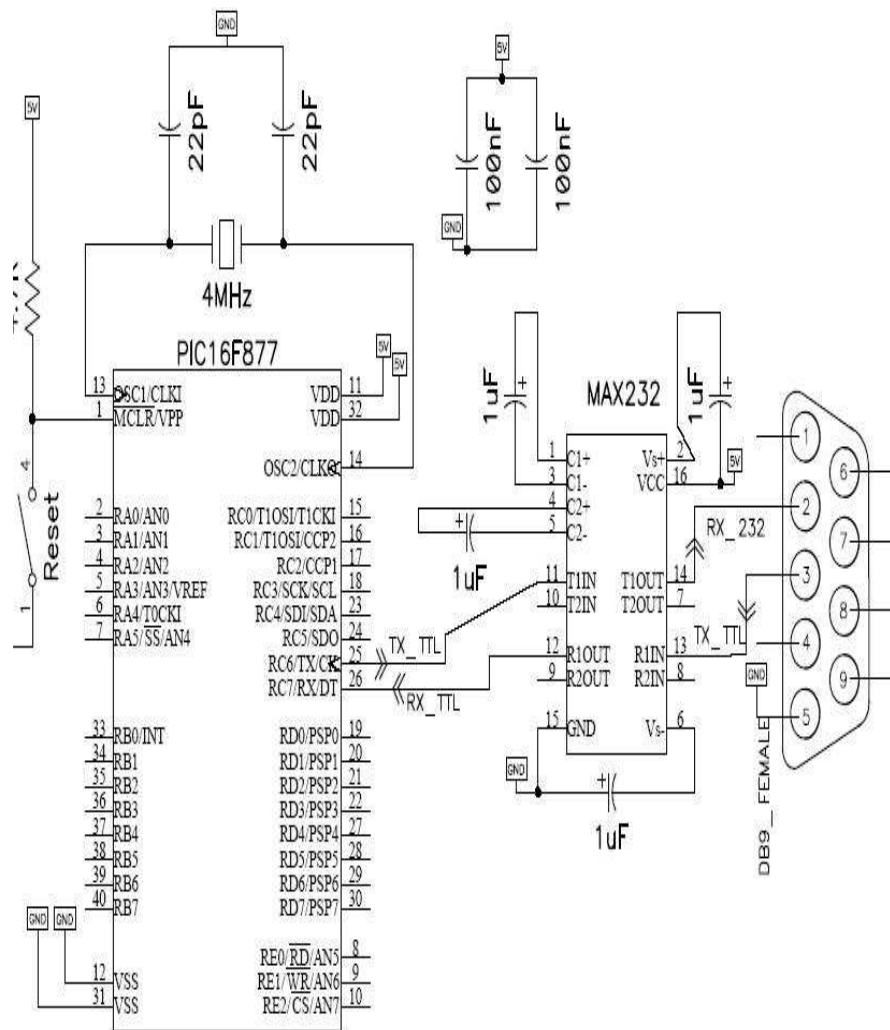


Figure 3.12: PIC16F877 μC connecting scheme

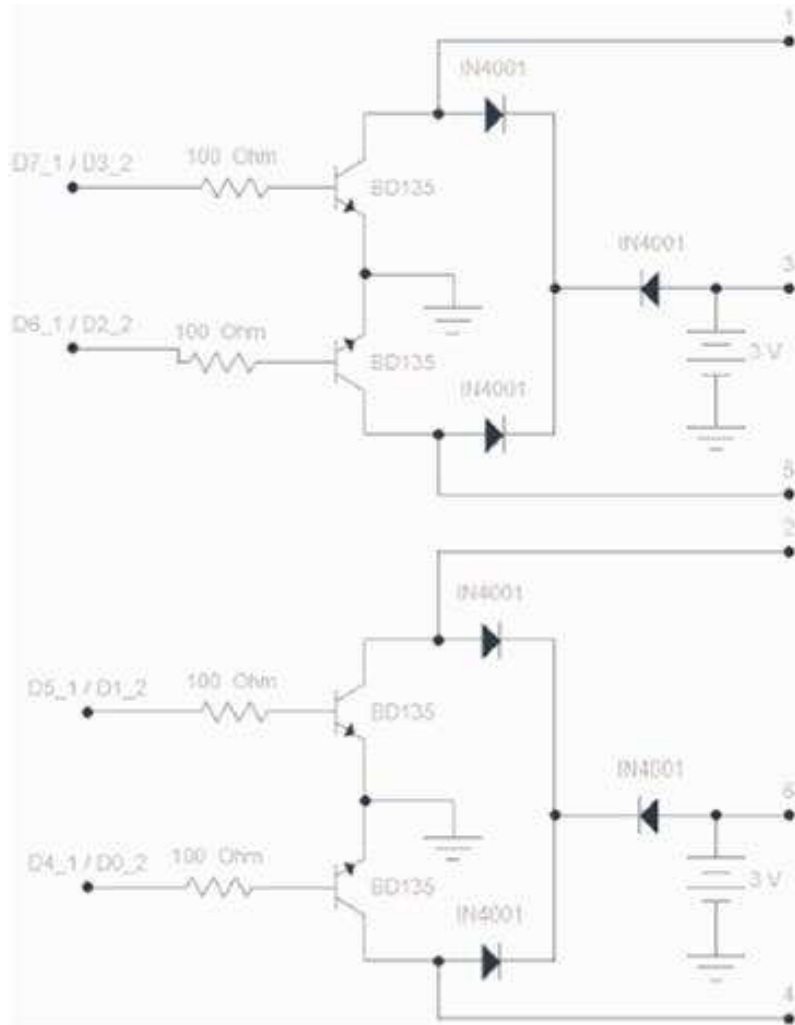


Figure 3.13: Step motor driving circuitry. Since the direction of the motion is 2D, there are two step motors. Thus, two of these circuits are required to control the two step motors separately. Here ' i ' in Dk_i represents the motor number while ' k ' represents the pin number of the μC . The voltage levels in nodes $D7_1, \dots, D4_1$ ($D3_2, \dots, D0_2$ for the other step motor driver) controls the voltage levels in terminals 1, 3, 2 and 4, respectively.

3.2.1 RS-232 Programming

RS-232 communication protocol uses serial communication where one bit is sent along a line at a time. To communicate via RS-232 there are two options:

1. *no-handshaking*: the transmitter sends data without waiting acknowledgment from the receiver,
2. *handshaking*: the transmitter waits for the acknowledgment from the receiver.

In this study handshaking is used with 9600 baud rate, even parity, 7 data bits per byte, 1 stop bit. For the serial communication, the registers of the PIC16F877 μC should be initialized before the communication starts. For asynchronous mode of the USART module (Universal Synchronous Asynchronous Receiver Transmitter) related registers are: 1) *SPBRG*, 2) *TXSTA*, 3) *RCSTA*, 4) *TXREG*, 5) *RCREG*, 6) *PIR*, 7) *PIE* [60]. Initializing process of these registers and the details of programming the PIC16F877 μC for serial communication can be found elsewhere [69], [70].

3.3 Data collection, acquisition and analysis software

In this study data collection is performed with two different instruments. These are (1) Agilent 34401A Digital Multimeter, (2) Acquiretek CM-2251 Data Acquisition Card (DAC). In both cases, the data is acquired to a PC. A user interface program is prepared using LabVIEW to control the CM-2251 DAC and also a user interface program is prepared using HP VEE to control the Agilent 34401A Digital Multimeter.

In the data analysis step, the graphical user interface (GUI) facility of MATLAB is used and a MATLAB based GUI is prepared.

The details of the programs are explained in the following subsections.

3.3.1 Data Collecting Step

3.3.1.1 HP VEE Based User Interface Program

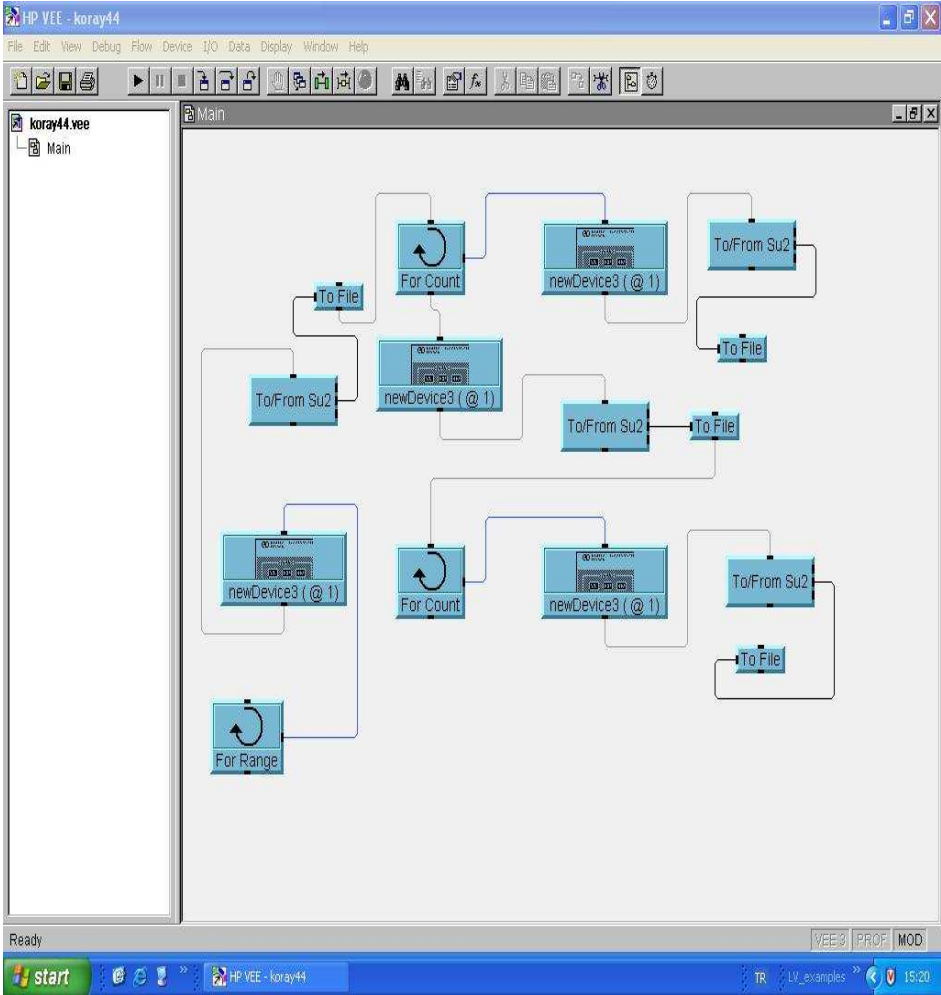


Figure 3.14: HP VEE 4.0 based user interface program.

HP VEE based user interface program (UIP) is prepared to perform scanning experiments using the HP34401A digital multi-meter and to control the XY scanner. The program communicates with the multi-meter via the GPIB port. The XY scanner is controlled by PIC16F877 micro-controller (μC) which communicates with the UIP via RS232 port while the multi-meter is still communicating through the GPIB port.

The UIP send serial data to the μC . According to the received data the μC drives the step motors and thus moves the sensor probe to the next measurement point. When the probe is settled, μC sends a 'done' signal to the UIP via the RS232 port. Then, the program waits for a user defined time of delay (in this study for 1 sec.) until the mechanical oscillation of the probe is damped. After this delay, the program sends a 'take measurement' comment to the multi-meter via the GPIB port and the measurements are sent to PC, again, via the GPIB port and saved in a file. The number of the samples that the multi-meter handles at each measurement point is defined by the user at the beginning of the experiment (in this study, 100 samples at each measurement point). After finishing the measurement task, the multi-meter sends a 'done' signal to the PC via the GPIB port and the process (starts at the beginning of this paragraph) repeats until the area defined by the user at the beginning of the experiment is scanned completely.

3.3.1.2 LabVIEW Based User Interface Program

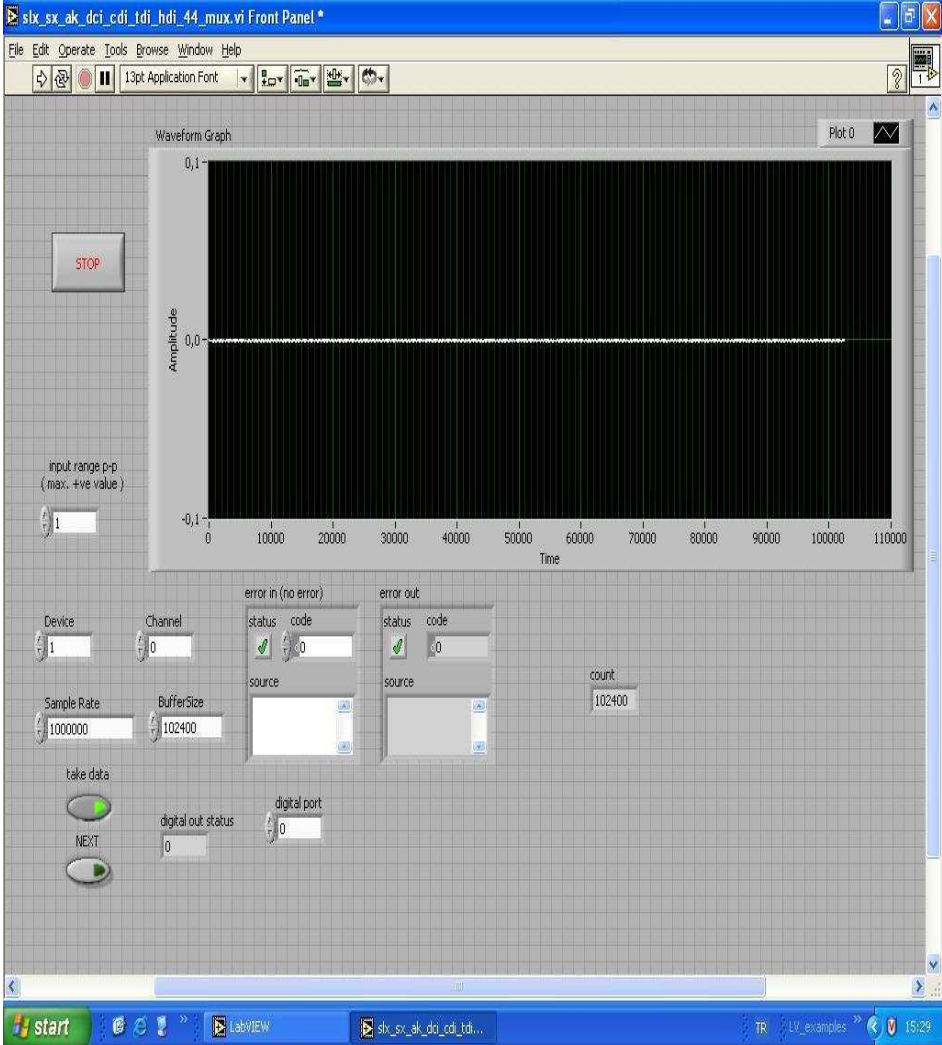


Figure 3.15: LabVIEW based user interface program.

LabVIEW based user interface program (UIP) is prepared to perform linearity experiments using the CM-2251 data acquisition card (DAC). The DAC is installed in a PCI slot. The number of the samples and the sampling rate is defined by the user before the experiment. When the phantom is placed under the sensor (for saline solution phantoms) or is connected to the conductive ring (for resistive ring phantoms) the user presses the 'take data' button, thus the measurement step is started. The green led on the button is turned on and handles its position during the measurement process. After finishing the measurement task the led turns off. The measured signals are also shown as a real time in a graph of the UIP.

The program is also capable of creating a user defined digital signal at any of its digital output pin. This facility added to the program to perform resistive ring experiments automatically by employing a multiplexer. In order to use this facility, the user defines a digital output pin by writing its number (the DAC has 16 digital output pins, thus the written number should be between 1-16) into the box named as 'digital port'. Then, the user can control the digital state of the selected pin by pressing the 'next' button.

3.3.2 Data Analysis Step

3.3.2.1 MATLAB Based User Interface Program

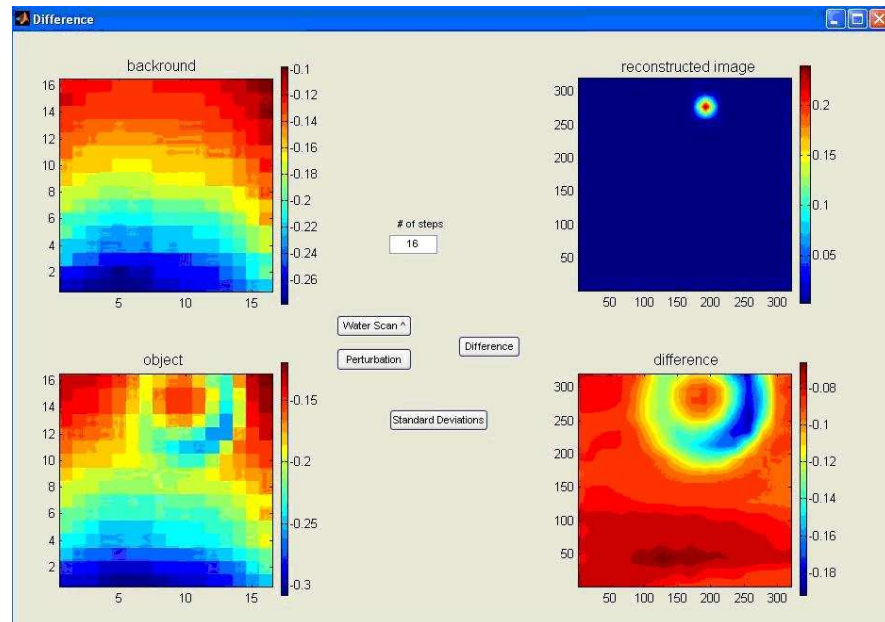


Figure 3.16: MATLAB based Graphical User Interface (GUI) program.

MATLAB based user interface program is prepared to analyze the field profiles (voltage measurements) obtained by scanning experiments. The scanning experiments for agar objects are performed in two steps:

1. The defined area is scanned without the agar object in the medium (i.e. in the saline solution). Thus the field profile for the background is obtained.
2. Then, the same area is scanned with the agar object in the medium, i.e. scanning is repeated with the agar object placed in the saline solution.

This program allows the user 1) to observe the image of the background (i.e. the image of the saline solution before the agar phantom is immersed). The image is shown in the upper left window in the GUI, 2) to observe the image of the agar object placed in the saline solution (i.e. the image of the agar object + saline solution). The image is shown in the lower left window in the GUI, 3) to observe the image of the former data being subtracted from the latter to give the image profile due to the agar object (i.e. the image of the agar object). The image is shown in the lower right window in the GUI, 4) to observe the reconstructed conductivity distribution of the object. The resultant conductivity distribution image for each iteration is shown in the upper right window in the GUI. Each of four images can be observed at the same time in one of the four available windows in the GUI.

CHAPTER 4

RESULTS

4.1 Introduction

A multi-frequency measurement system is realized. For different operating frequencies, the measurement procedures are the same. The only difference is the hardware, i.e. the sensor and the power amplifier used in the experiments. To avoid confusion, the measurement system used for single frequency experiments is named as the *prototype system* and the measurement system used for the multi-frequency experiments is named as the *multi-frequency system*. The prototype system operates at a single frequency of 50 kHz, whereas the multi-frequency system operates in the frequency range of 30-90 kHz.

The performance of both systems are tested individually to explore whether the systems can be used to image biological tissues. The response of the systems to conductivity variations is tested by using two types of phantoms, namely, the saline and resistance phantoms. Since using the resistive phantoms is more practical in testing the performance, the relation between these two phantoms is investigated. After determining this relation, only the resistive phantoms are used for daily tests. The resistance phantoms proved to be a novel and fast testing method for this imaging modality.

To understand the imaging performance, first agar phantoms are used. Experiments with living tissues are performed using leeches. The conductivity

images of a leech is reconstructed for the first time in the literature. The results are presented in the following subsections.

4.2 The Prototype System Operating at Single Frequency: 50 kHz

4.2.1 Sensitivity to conductivity variations

The response of the system to conductivity variations is investigated using two phantom types: saline solution phantoms and resistive phantoms. The relation between the corresponding measurements is investigated. The ratio given in Equation 4.1 reveals the relation between the slopes of the two linearity measurements.

$$Slope_{Resistors} = 8.108 \left[\frac{(S/m)}{Mho} \right] \times Slope_{Saline\ Solutions} \quad (4.1)$$

After determining this relation, the daily tests are performed using the resistance phantoms.

4.2.1.1 Saline Solution Phantoms

Saline solution phantoms are developed using a 11.5 cm diameter, 1.1 cm deep circular vessel filled with saline solutions of different conductivities. The vessel is placed at a distance of 1 mm below the sensor. The theoretical fact that the voltage measurements show linear dependence to conductivity variations is confirmed within the tissue conductivity range (0.1 S/m - 7 S/m). The measured voltages as a function of conductivity are shown in Figure 4.1. The linearity of the system is obtained as 3.96 % of the full scale. The slope of this curve, namely, the sensitivity of this system is 13.2 mV/(S/m).

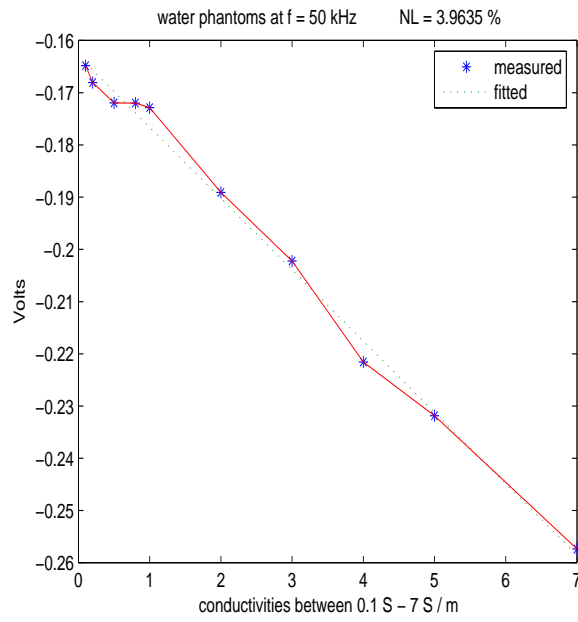


Figure 4.1: Receiver coil output voltages as a function of conductivity obtained by using saline solution phantoms (100 data are taken for each phantom).

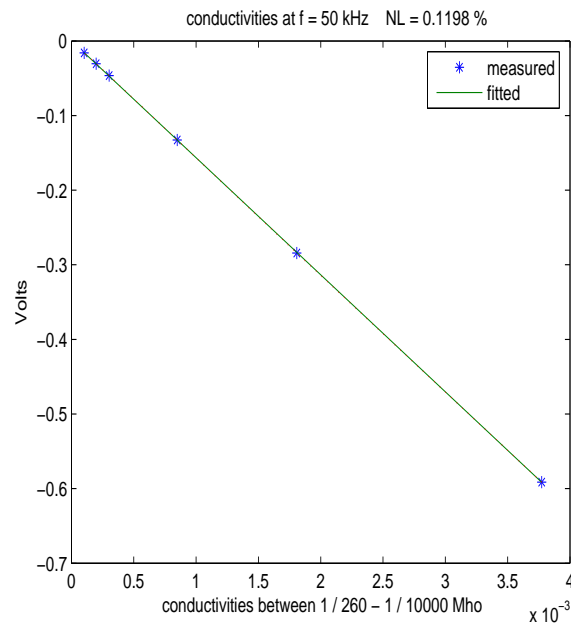


Figure 4.2: Receiver coil output voltage as a function of conductivity obtained by using resistance phantoms (100 data are taken for each phantom)

4.2.1.2 Resistance Phantoms

The saline solution phantoms are impractical both in preparation and in usage. To overcome this difficulty, a novel test method that employs resistance phantoms is proposed. A three-turn coil with a diameter of 9 mm is stuck on the sensor and different resistances between 260Ω - 10000Ω are connected to the open ends of the three-turn coil (The details of the experiment are explained in Appendix C). Equation B.11 shows that this resistance range corresponds to a conductivity range of 5.7 S/m - 0.125 S/m . The measured voltages as a function of conductivity are shown in Figure 4.2. When the resistive phantoms are used, the linearity of the system is obtained as 0.12% of the full scale. The slope is calculated as 155.02 mV/Mho .

4.2.2 Signal to Noise Ratio

Signal-to-noise ratio (SNR) is an important quantity in determining the performance of imaging systems. SNR in the experimental data is defined by the ratio of the signal variance to the noise variance, and is often expressed in decibels:

$$SNR = 10 \log_{10} \frac{\sigma_s^2}{\sigma_n^2} \quad (4.2)$$

where σ_s^2 and σ_n^2 are the variances of the signal and noise, respectively. In these thesis study, these variances are calculated by obtaining 100 samples of the data at a point in an area of $11.5\text{ cm} \times 11.5\text{ cm}$. The data is obtained on a 16×16 grid with and without conductive body. When the conductive body is placed, the measurements also contain a noise component. Thus, in order to obtain the true signal data, average value the of noise component is subtracted from the average value of signal at each data point. The SNR of the system is obtained as 35.44 dB .

4.2.3 Spatial Resolution

Spatial resolution is a measure of how well the system can distinguish two closely located point or line objects. One common method to find the spatial resolution is finding the Full Width Half Maximum (FWHM) of the Point Spread Function (PSF). To determine the FWHM of the system, a cylindrical agar phantom of conductivity 6 S/m (blood conductivity) is prepared and placed in 0.2 S/m (average tissue conductivity) solution. The radius and height of the phantom is 7.5 mm and 17 mm, respectively. 11.5 cm \times 11.5 cm area is scanned and data is acquired on a 16 \times 16 grid (i.e. pixel size is 7.2 mm). Thus the object is approximately one pixel size.

The field profile and the reconstructed conductivity image is shown in Figure 4.3(a) and (b), respectively. FWHM of the PSD in the x-direction is found as 9.36 mm and is shown in Figure 4.3(c). To determine the spatial resolution of the system another experiment is performed using two agar bars. The bars have a width of 15 mm, length of 57 mm, and 17 mm height with a conductivity of 6 S/m. The same experimental conditions are established. The results are shown in Figure 4.6. Spatial resolution found in this way is 14.4 mm.

4.2.4 Image Reconstruction

Experiments using agar phantoms are performed to understand the performance of the system for biological subjects. Different shaped agar phantoms with conductivity of 6 S/m are placed in a saline solution of conductivity 0.2 S/m. Finally, as a biological subject a leech is scanned and the image of the first living tissue is obtained in the literature. To reconstruct the conductivity distributions of the subjects, the inverse problem is solved by employing the Steepest Descent method (the effect of $\nabla\phi$ term is ignored in inverse problem solution). The results of these experiments are given in the following subsections.

4.2.4.1 Cylindrical Agar Phantom

In the first experiment, the cylindrical agar phantom of conductivity 6 S/m (blood conductivity) is prepared and placed in 0.2 S/m (average tissue conductivity) solution. The radius and the height of the phantom is 7.5 mm and 17 mm, respectively. 11.5×11.5 cm area is scanned on a grid of 16×16 data points. The results are shown in Figure 4.3. In the second experiment the same phantom is placed in different location in the scanning area. The aim of this experiment is to see the performance of the system in determining the location of the object. The results are shown in Figure 4.4.

4.2.4.2 Agar Phantom Bars

In this group of experiments, the performance of the system for imaging objects with sharp edges is investigated. For this purpose 2 agar phantom bars of conductivity 6 S/m are prepared. The bars are 15 mm width, 57 mm long and 17 mm height. The bars are inserted in a saline solution of conductivity 0.2 S/m and 17 mm height. Two experiments are performed with these bars.

In the first experiment, a single bar is placed in the solution. The results are shown in Figure ???. The shape and size of the object is not clearly apparent in the field profile shown in Figure ??(a), however, in the reconstructed conductivity distribution (Figure ??(b)) the object is clearly identified.

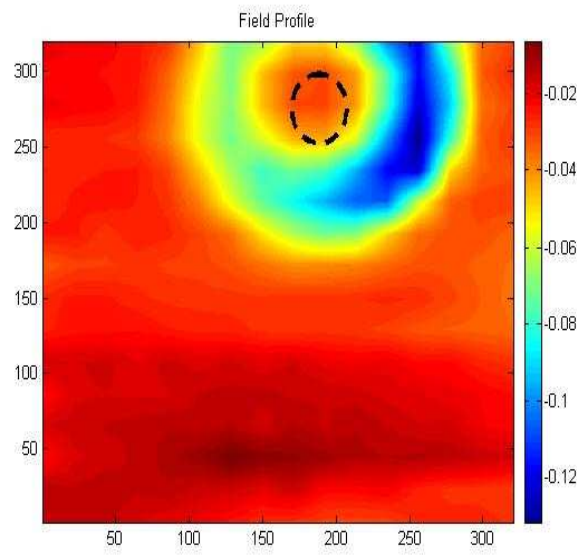
In the second experiment two agar bars are inserted into the solution. The results are shown in Figure 4.6. The actual shape and the size of these bars are not clearly apparent in the field profile shown in Figure 4.6(a). After the solution of the inverse problem, the bars are easily identified both in shape, size and location (as seen from Figure 4.6(b)).

4.2.4.3 The First Conductivity Images of a Living Tissue

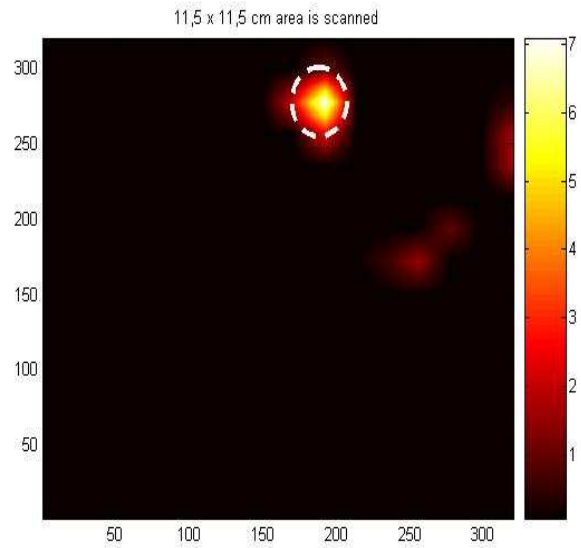
Imaging a living biological tissue is the focus of this study since 1998 [57]. After imaging agar phantoms and testing the performance of the system, we wonder the results for a living biological body. Since the distance between the body to be imaged and the sensor is an important constraint, the body should have a smooth surface. It should also have a simple geometry and possibly a simple conductivity distribution. For this purpose, three invertebrates are considered: an earthworm, a leech, and a snake.

The body of the animal should not move during the scanning process. It would be difficult to anaesthetize a snake in the laboratory. The earthworm is a cold-blooded animal and related tissues may have low conductivities. Since leeches suck blood, the tissue conductivities may be high enough to be detected by the developed system. Thus, the first animal experiments are performed using leeches.

To make a leech stable during the scanning process, it is anaesthetized with ether. 11.5 cm \times 11.5 cm area is scanned on a grid of 16 \times data points. The results are shown in Figure 4.7.

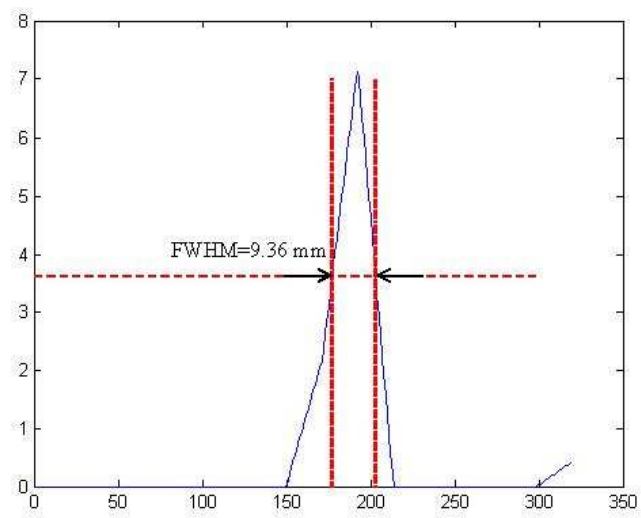


(a)



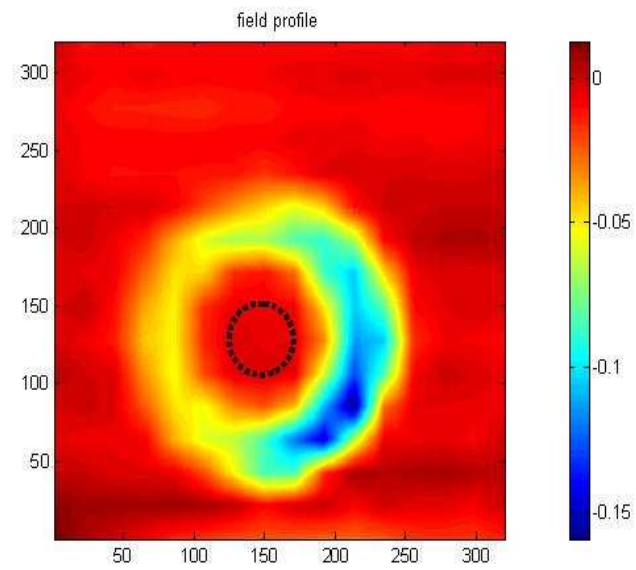
(b)

(Fig. 4.3 is cont. at next page)

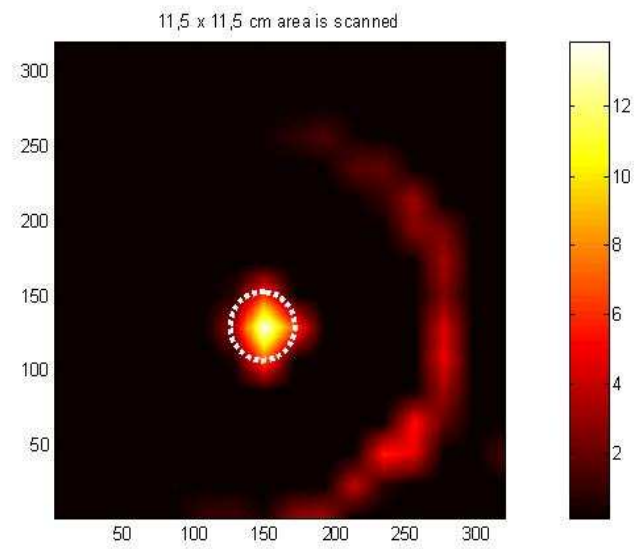


(c)

Figure 4.3: Experiment result and inverse problem solution of 7.5 mm radius circular agar phantom: (a) measured field profile, (b) reconstructed conductivity distribution, (c) FWHM calculation.

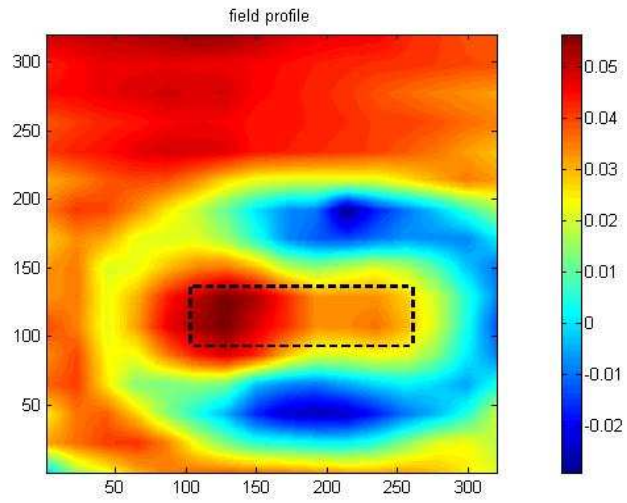


(a)

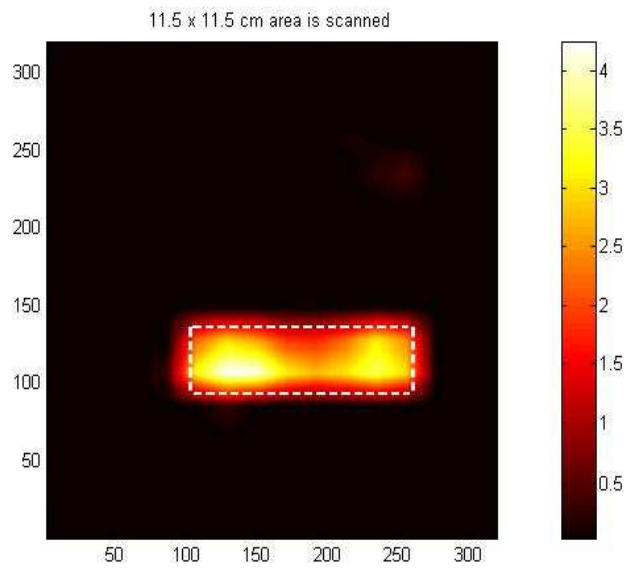


(b)

Figure 4.4: Experiment result and inverse problem solution of 7.5 mm radius circular agar phantom placed at the center of the scanning area: (a) measured field profile, (b) reconstructed conductivity distribution.

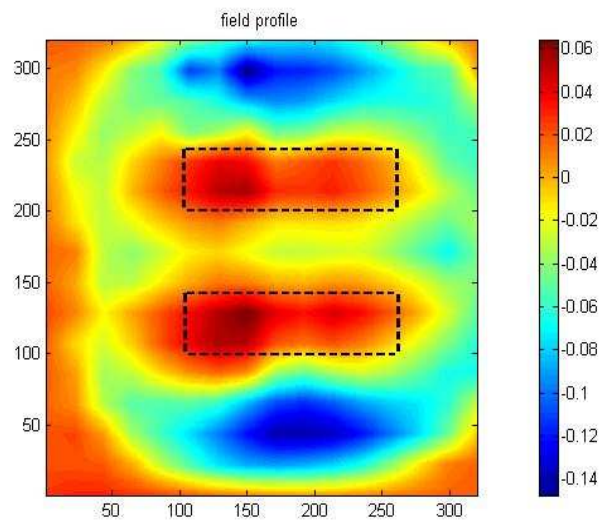


(a)

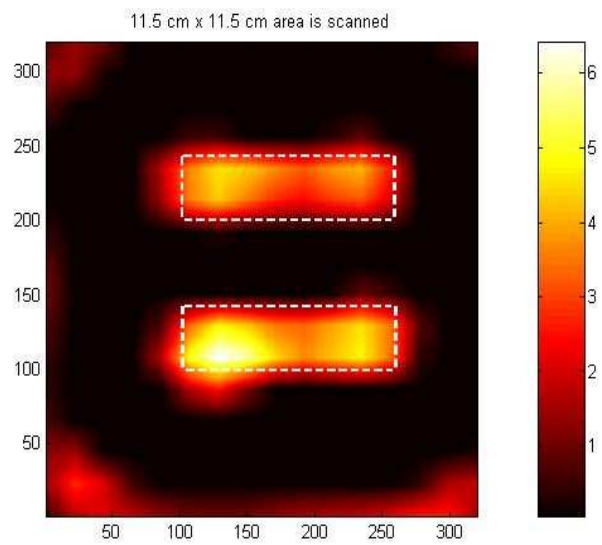


(b)

Figure 4.5: Experiment result and inverse problem solution of the 15 mm width, 57 mm long bar shaped agar phantom : (a) measured field profile, (b) reconstructed conductivity distribution.

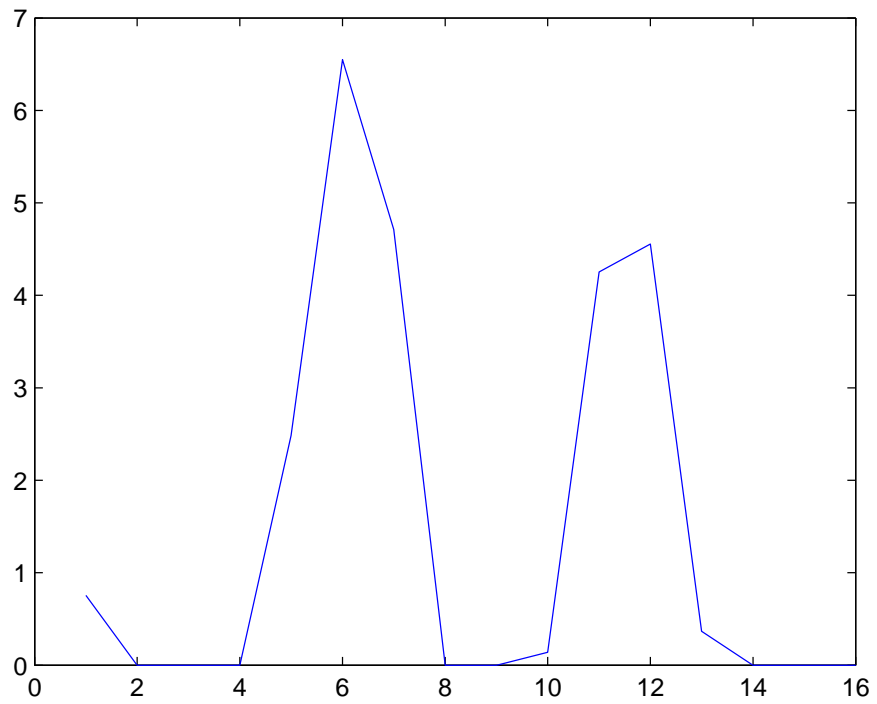


(a)



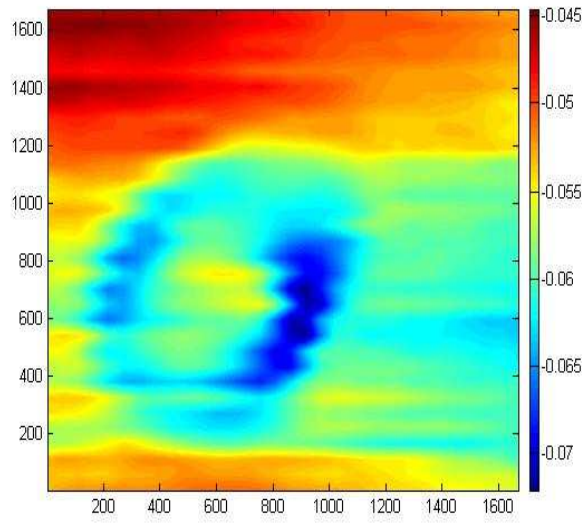
(b)

(Fig. 4.6 is cont. at next page)

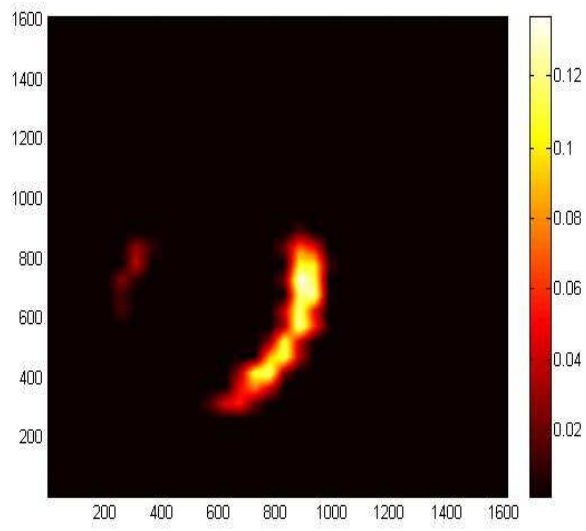


(c)

Figure 4.6: Experiment result and inverse problem solution of two 15 mm width, 57 mm long bar shaped agar phantoms : (a) measured field profile, (b) reconstructed conductivity distribution, (c) image spread along axial direction.

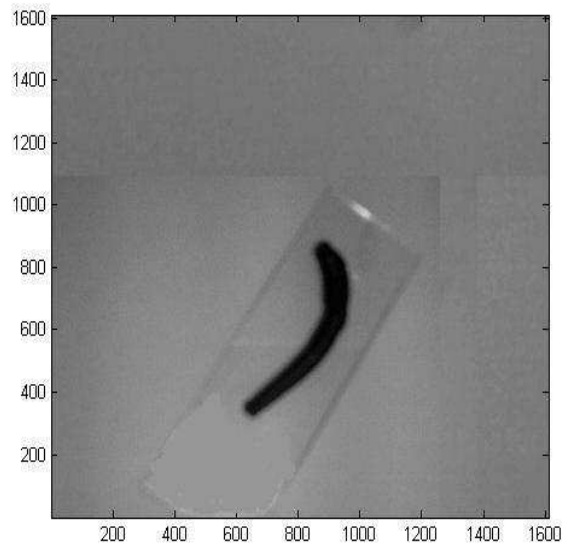


(a)

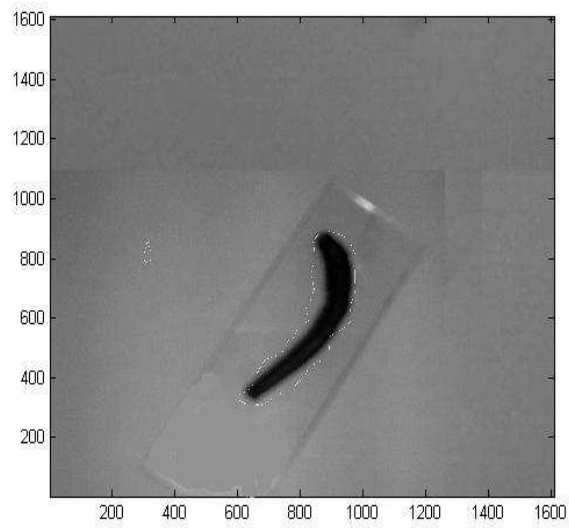


(b)

(Fig. 4.7 is cont. at next page)

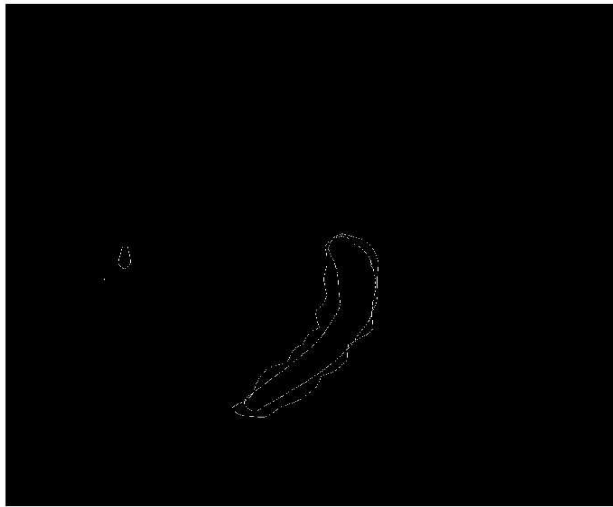


(a)



(b)

(Fig. 4.7 is cont. at next page)



(c)

Figure 4.7: The first conductivity images of a living tissue: imaging a leech. (a) The measured field profile, (b) reconstructed conductivity distribution, (c) photograph of the leech, (d) edges of the reconstructed conductivity distribution, (e) the boundaries of the leech and the reconstructed conductivity distribution are shown on the same figure.

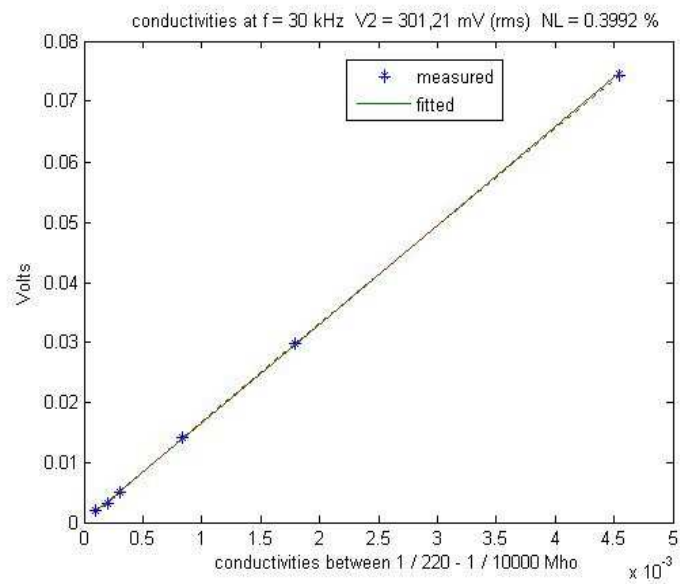
4.3 The Multi-Frequency System

The multi-frequency system operates at 30 kHz, 50kHz, 60 kHz and 90 kHz. Since the signal intensity increases with the square of the operating frequency, the response of the system to conductivity variations should improve as the frequency increases. The frequency response of the system to conductivity variations is tested for each operating frequency. The results are presented in the following subsections.

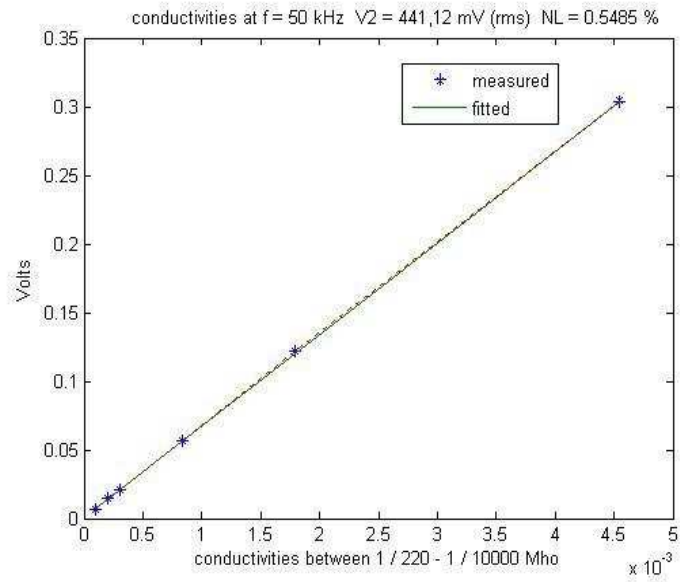
4.3.1 Sensitivity

Since a relation is established between the saline solution and the resistance phantoms (Equation 4.1), only the resistance phantoms are used to determine the sensitivity of the system at each operating frequency. This novel test method is very fast and less laborious to determine the sensitivity of the system. The results are shown in Figure 4.8. Here V_2 is the voltage measured on the monitor resistance 2Ω (the transmitter coil current is flowing through the monitoring resistance).

Theoretically, as seen in Equation 2.9, the measurements are proportional with the square of the frequency. To determine the frequency response of the system, slopes of the measured voltages are normalized with the average of the transmitter coil currents. The slopes, normalized slopes, monitoring resistance voltages and the operation frequencies are given in Table 4.1. The slopes of the normalized measurements as a function of frequency are shown in Figure 4.9. As seen in the Figure 4.9, the results verify the theory.

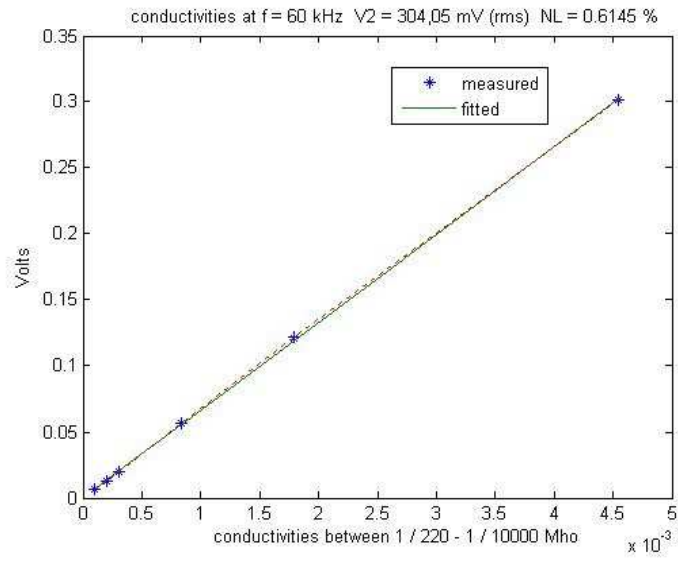


(a)

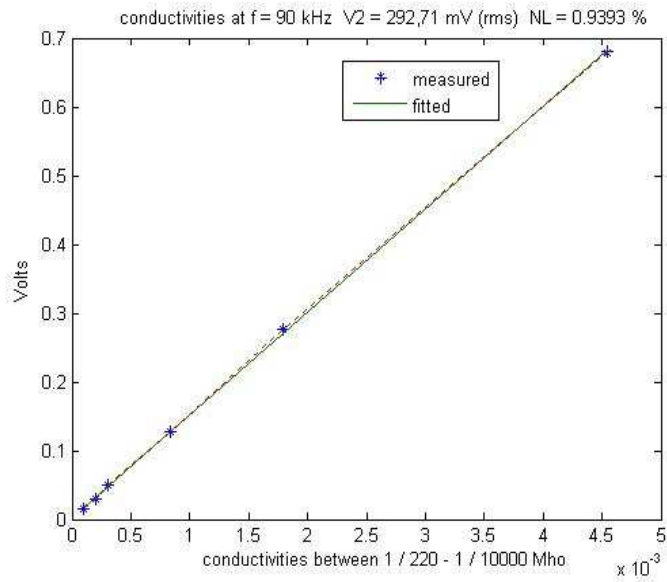


(b)

(Fig. 4.8 is cont. at next page)



(c)



(d)

Figure 4.8: Receiver coil output voltage as a function of conductivity at (a) 30 kHz, (b) 50 kHz, (c) 60 kHz, (d) 90 kHz.

Table 4.1: The excitation currents and the slopes of the measured voltages at each operation frequency in the multi-frequency experiment.

Frequency (kHz)	Excitation current (mA)	Slope (mV / Mho)	Normalized Slope (mV / Mho)
30	150.605	16.3843	18.2099
50	220.56	66.836	50.7228
60	152.025	66.401	73.1104
90	146.355	149.6673	171.1745

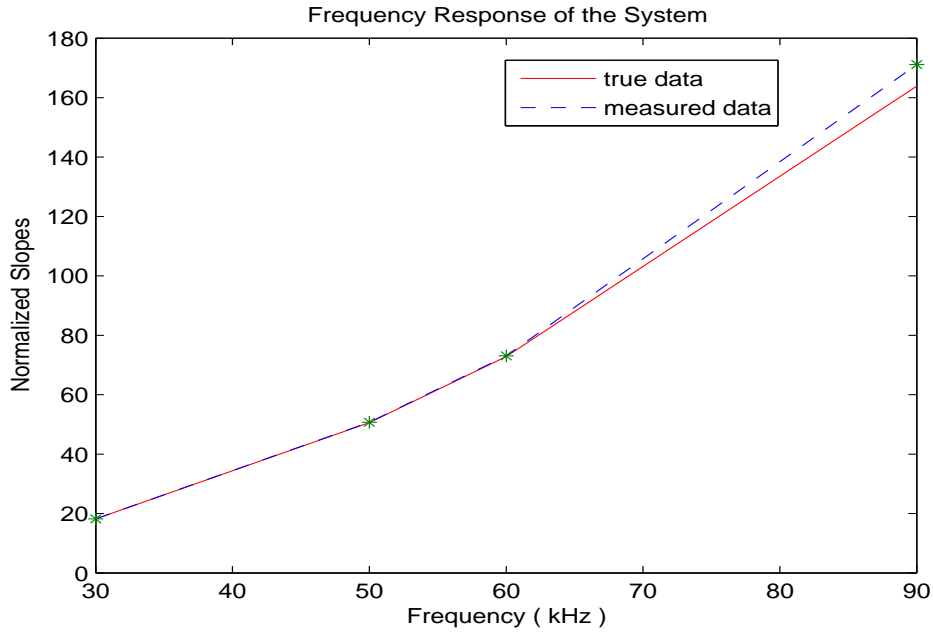


Figure 4.9: The normalized slopes of the sensitivity experiments (receiver coil output as a function of conductivity measurements) at each operation frequency. In theory (Equation 2.9), the measured voltage is proportional to the square of the frequency.

4.3.2 Signal to Noise Ratio

The SNR of the multi-frequency system is investigated at each operation frequency. The calculation of the SNR is explained in Section 4.2.2. The results are given in Table 4.2. The SNR of the system as a function of frequency is drawn in Figure 4.10. As it is expected, the SNR of the system is increasing as the frequency increases.

Table 4.2: SNR of the multi-frequency system at each operation frequency.

Frequency (kHz)	SNR (dB)
30	20.535
60	37.260
90	45.788

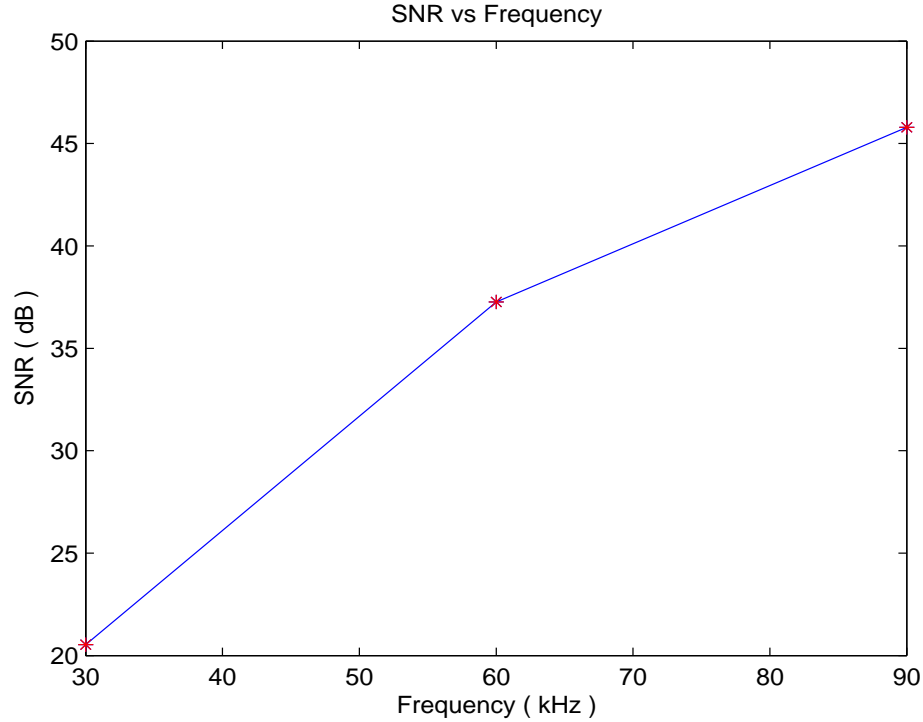


Figure 4.10: SNR of the multi-frequency system as a function of frequency.

4.3.3 Spatial Resolution

To determine the spatial resolution of the imaging system, the Full Width Half Maximum (FWHM) of the point spread function is calculated. A 10 mm \times 10 mm square-shaped agar phantom with conductivity of 6 S/m (blood conductivity) is prepared to simulate a small conductive body. The body is 17 mm in height. The experiments are performed at 30 kHz, 60 kHz and 90 kHz. 129 mm \times 129 mm area is scanned with 36 \times 36 data points. The FWHM of the system is determined at each operating frequency. Note that, while scanning the conducting body, there are two other conductive bodies with

Table 4.3: FWHM of the multi-frequency system at each operation frequency.

Frequency (kHz)	FWHM (mm)
30	19.8
60	10.8
90	9

different shapes in the scan area (assuming they are at distant locations and thus, do not effect the measurements). The photograph of the phantoms are shown in Figure 4.14. The image spread of the square shaped body along the x-direction is plotted at 30 kHz in Figure 4.11 , at 60 kHz in Figure 4.12 and at 90 kHz in Figure 4.13. The FWHM calculation results are also given in Table 4.3.

4.3.4 Image Reconstruction

Three agar phantoms of conductivity 6 S/m (blood conductivity) are prepared to understand the frequency dependency of the measured signal and, thus, the quality of the reconstructed images at each operation frequency. These three phantoms are: 1) a 15 mm diameter circular body, 2) a 10 mm \times 10 mm square shaped body (also used in the FWHM calculations), and 3) a 10 mm \times 27 mm rectangular body. The phantoms are all 17 mm in height.

The experiments are performed using three different operation frequencies (30 kHz, 60 kHz and 90 kHz). 129 mm \times 129 mm area is scanned with 36 \times 36 data points. To reconstruct the conductivity distributions of the bodies, the inverse problem is solved by employing the Steepest Descent method (the effect of $\nabla\phi$ is ignored in the inverse problem solutions). The field profile and the reconstructed conductivity distribution obtained at 30 kHz, 60 kHz and 90 kHz are given in Figure 4.15, Figure 4.16 and Figure 4.17, respectively. The photograph of the agar phantoms is shown in Figure 4.14. As it is expected, the reconstructed images resemble the actual distribution, as the operating frequency increases.

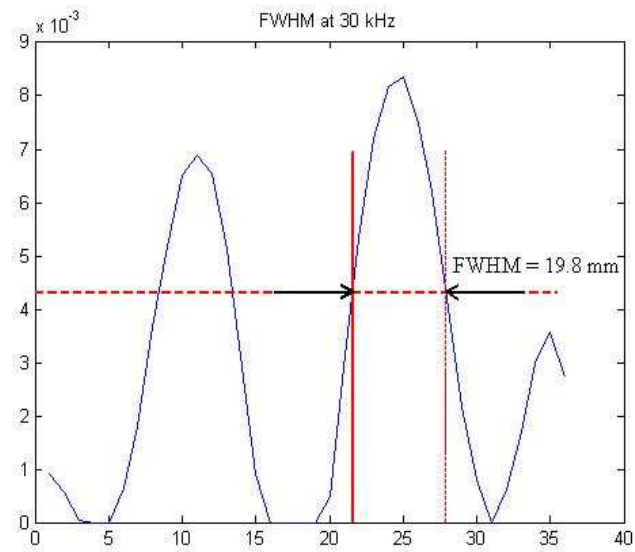


Figure 4.11: Measured profile on the horizontal line of Figure 4.15(b). The FWHM is calculated as 19.8 mm at 30 kHz.

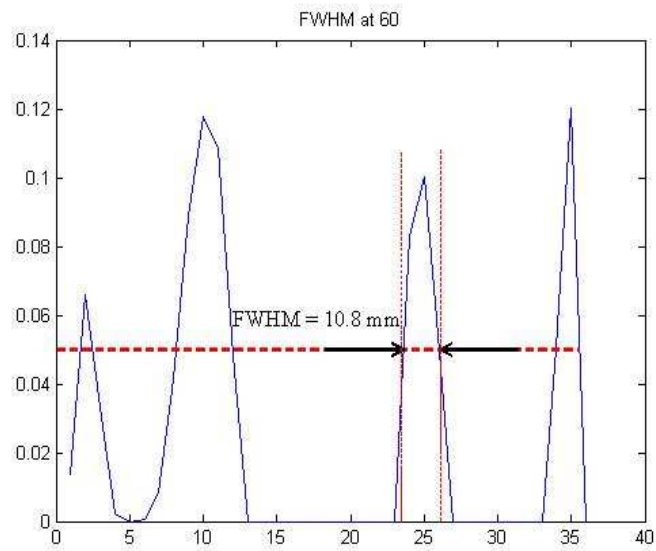


Figure 4.12: Measured profile on the horizontal line of Figure 4.15(b). The FWHM is calculated as 10.8 mm at 60 kHz.

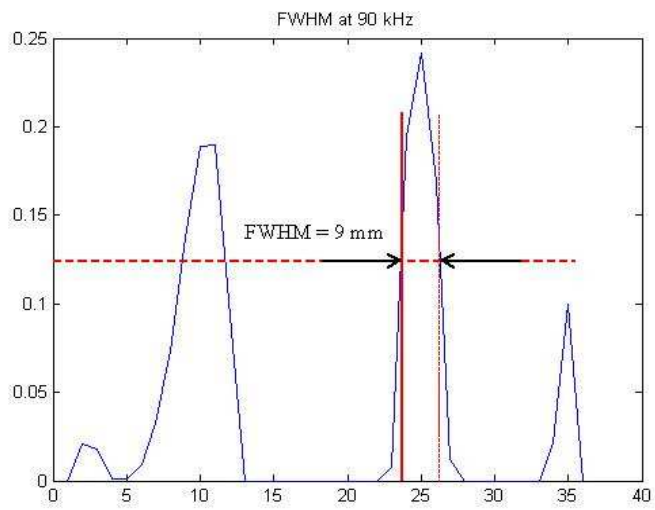


Figure 4.13: Measured profile on the horizontal line of Figure 4.17(b). The FWHM is calculated as 9 mm at 90 kHz.

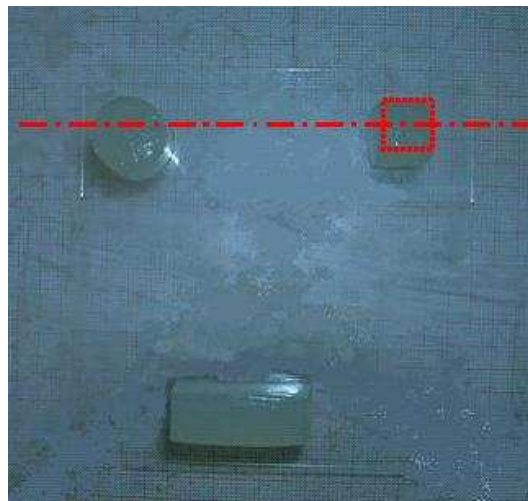
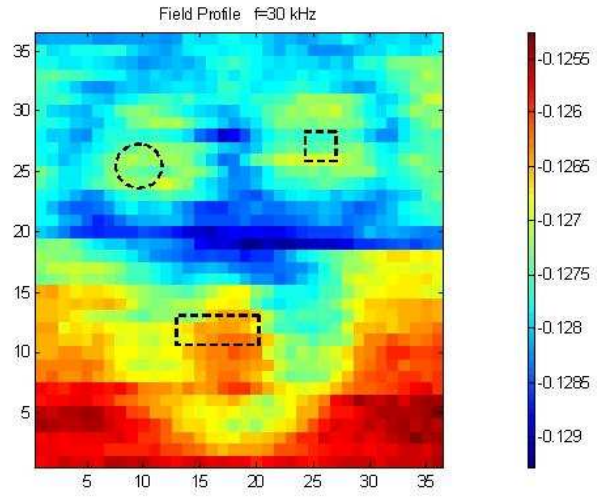
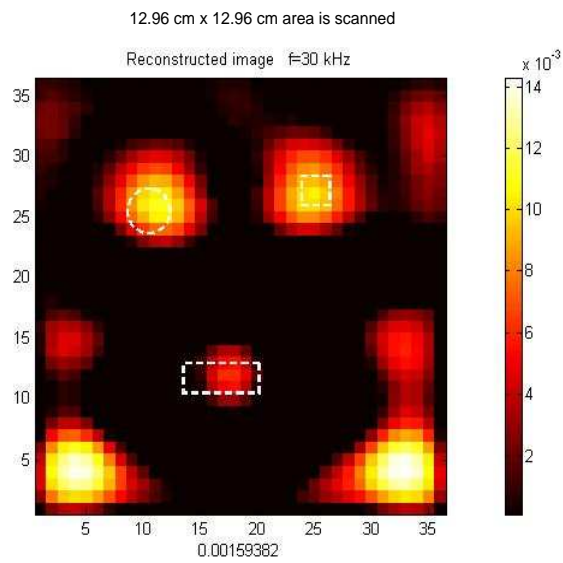


Figure 4.14: The photograph of the phantom with three agar bodies of different shapes. The conductivity of the agar blocks is 6 S/m.

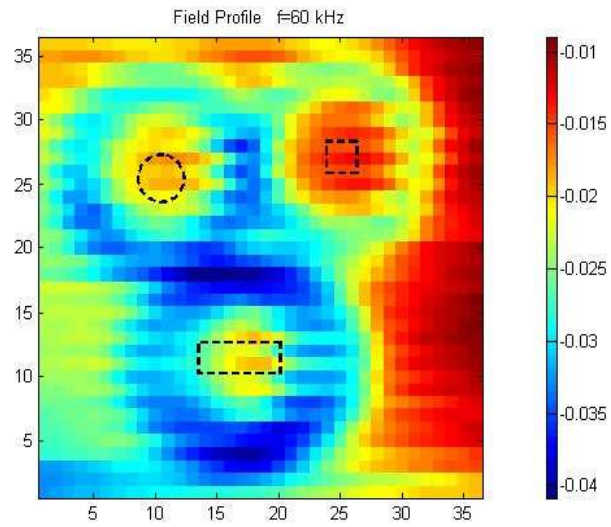


(a)



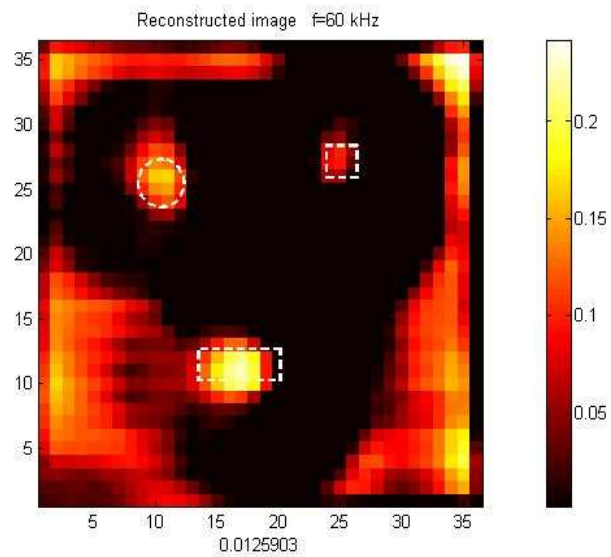
(b)

Figure 4.15: Experiment results for the agar phantom at 30 kHz: (a) measured field profile, (b) reconstructed conductivity distribution profile.



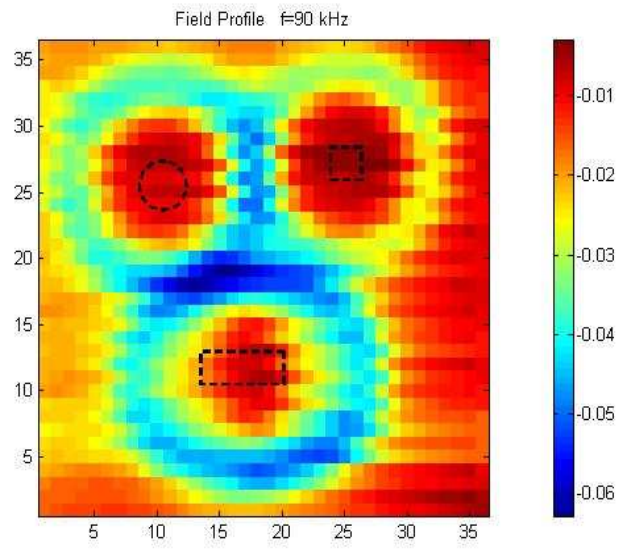
(a)

12.96 cm x 12.96 cm area is scanned



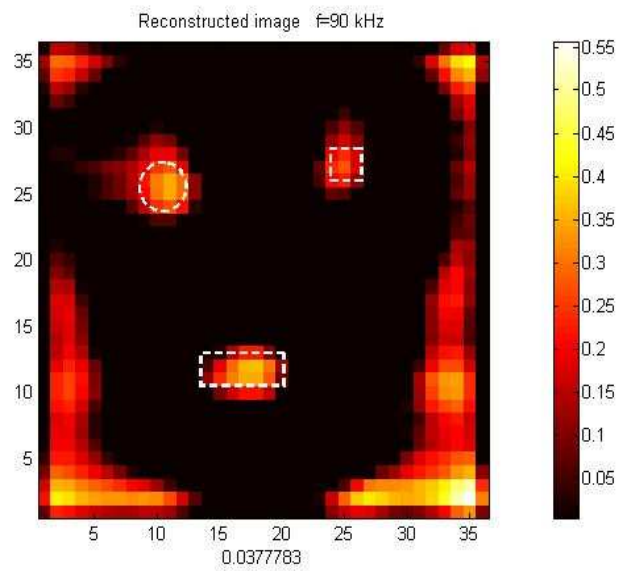
(b)

Figure 4.16: Experiment results for the agar phantom at 60 kHz: (a) measured field profile, (b) reconstructed conductivity distribution profile.



(a)

12.96 cm x 12.96 cm area is scanned



(b)

Figure 4.17: Experiment results for the agar phantom at 90 kHz: (a) measured field profile, (b) reconstructed conductivity distribution profile.

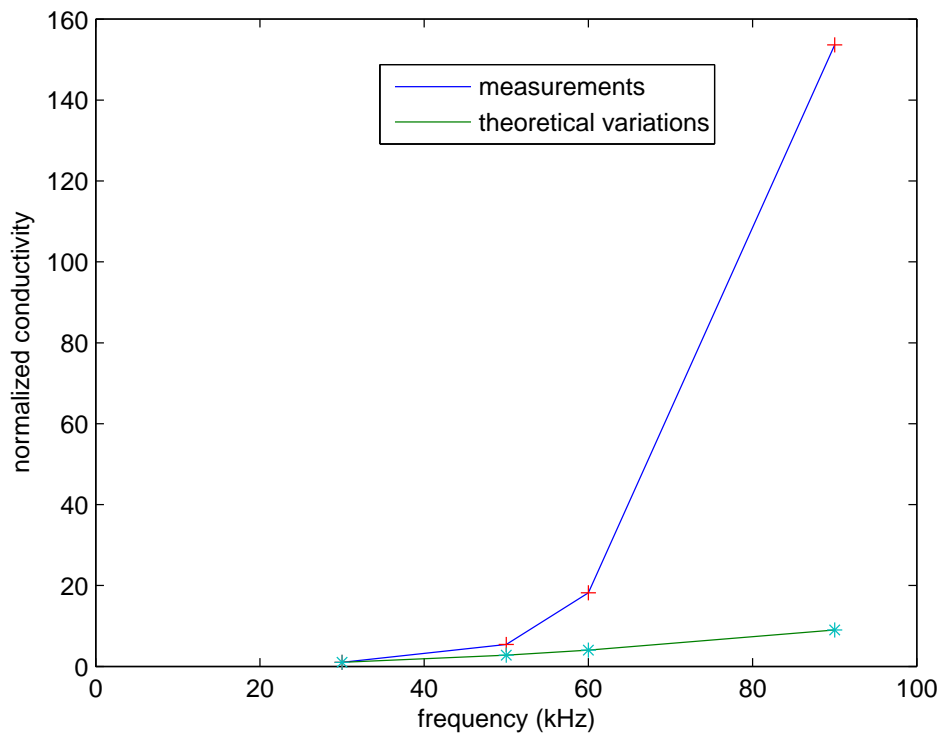


Figure 4.18: Conductivity spectrum of a potato. If the conductivity of the potato was independent from the frequency and was equal to that was measured at 30 KHz, the measured conductivities were to be equal to the conductivity values shown with a star (*). Since the plots are different it is concluded from the figure that the conductivity of the potato increases as the frequency increases. Data have been normalized with respect to the readings at 30 kHz.

4.4 Spectroscopy

The conductivity spectrum of a potato is shown in Figure 4.18 with a plus (+). If the conductivity of the potato was constant at each frequency and was equal to that was measured at 30 kHz, the measured conductivities varied linearly with the square of the frequency and were to be equal to the conductivity values shown with a star (*) in Figure 4.18. The green line is similar to the red line shown in Figure 4.9. The spectra shown demonstrate the feasibility of magnetic conductivity spectroscopy.

4.5 Equivalent Input Noise Voltage

4.5.1 Introduction

All external noise coupling could be eliminated from a circuit with proper shielding, however, the noise would still exist in the circuit due to certain intrinsic or internal noise sources. Thermal noise is the most important intrinsic noise source and is present in all elements containing resistance. Active devices, such as bipolar transistors, field effect transistors, op-amps and other integrated circuits also have inherent noise generation mechanisms. The common method of specifying active device noise is the use of a noise voltage and current model. The calculation of an active device noise and the thermal noise of a resistance is explained in Appendix D. This is important because only the voltages greater than that noise level can be detected by the system. In the following section, the input referred noise of the data acquisition circuit is calculated.

4.5.2 The Input Noise of the Data Acquisition Card

The noise of a resistance can be calculated using Equation D.1 as given in Appendix D. The equivalent noise of the integrated circuits can be calculated by using the noise equivalent model of the IC's as explained in Section D.2 in Appendix D. The manufacturers provide the equivalent input noise voltage and current $V_n - I_n$ (or $e_n - i_n$) in the data sheets of the ICs. For example, in the data sheet of LF-356 op-amp from the National Semiconductor, the equivalent input noise voltage and current noise are given as $12 nV/\sqrt{Hz}$ and $0.01 pA/\sqrt{Hz}$, respectively [71]. These equivalent values should be multiplied with the bandwidth of the circuit (see Section D.1 in Appendix D).

The values for $V_n - I_n$ of the components used in the data acquisition card are provided from the data sheets of the ICs ([6], [71]-[73]) and the equivalent input noise voltage is calculated as $146.80 nV$. The system cannot detect signal voltages below this value. This is the physical limit of the circuit and can be improved by using low noise components.

CHAPTER 5

CONCLUSIONS AND DISCUSSION

5.1 Summary and Conclusion

A prototype system (operating at 50 kHz) and a multi-frequency system (operating between 30-90 kHz) were developed to image electrical conductivity of biological tissues via contactless measurements .

Two different sensors were designed and implemented for each of the two systems. The sensors are quite sensitive to conductivity variations in the vicinity of the average tissue conductivity (0.2 S/m). A new data acquisition card was designed and constructed on PCB. This was an important step to make the system portable. The equivalent input noise voltage of the card was found as 146.80 *nV*. An HP-VEE based user interface program was prepared to perform the scanning experiments using a PC. A LabVIEW based user interface program was prepared to perform experiments by using the Acquitek CM-2251 data acquisition card. In the data analysis step, a MATLAB based graphical user interface program was prepared. A novel test method employing resistive ring phantoms has been developed to investigate the sensitivity of the system. The theoretical relation between saline solution phantoms and resistive ring phantoms was determined.

The prototype system has an SNR of 35.43 dB. The sensitivity of the system to saline solution phantoms (saline solution filled vessels) is 13.2 mV/(S/m)

and to resistive ring phantoms is 155.02 mV/Mho , while the linearity is 3.96% of the full scale for the saline solution phantoms and 0.12% of the full scale for the resistive ring phantoms. The spatial resolution of the prototype system is found as 9.36 mm with cylindrical agar phantoms and 14.4 mm with two agar phantom bars. The average data acquisition time (scanning and recording the output for 100 samples) is calculated as 0.29 sec/mm^2 . To understand imaging performance, different agar phantoms were scanned. The field profiles and the reconstructed conductivity distributions of the objects were obtained. The reconstructed images show the exact location, actual size and geometry of the objects. Consequently, the first living tissue experiment in this field was performed and the image of a living tissue, a leech, is reconstructed for the first time in the literature.

The SNR of the multi-frequency system is calculated as 20.53 dB at 30 kHz, 37.26 dB at 60 kHz and 45.79 dB at 90 kHz. As it is expected, the SNR of the system is increasing as the frequency increases. The resistive ring phantoms were used to determine the sensitivity of the system at each operation frequency. In this experiments the transmitter coil current values were slightly different for each frequency, thus, the slopes of the measurements were normalized with respect to the transmitter coil currents. The normalized sensitivity of the system is 18.21 mV/Mho at 30 kHz, 50.72 mV/Mho at 50 kHz, 73.11 mV/Mho at 60 kHz and 171.17 mV/Mho at 90 kHz. The results verify the theory. The spatial resolution of the system is found as 19.8 mm at 30 kHz, 10.8 mm at 60 kHz and 9 mm at 90 kHz. The field profiles and the reconstructed conductivity distributions of the objects were obtained at different frequencies for the first time in the literature. The conductivity spectrum obtained demonstrates that, using electrical conductivity imaging via contactless measurements technique, spectroscopy is possible within the β -dispersion range of biological tissues. The results show the potential of this method for clinical applications.

The innovations of this study can be summarized as follows:

- Sensors working at different operation frequencies were designed and fabricated. The sensors are sensitive to conductivity variations in the vicinity of the average tissue conductivity (0.2 S/m)
- A portable data acquisition card was designed and constructed on a printed circuit board. This is an important step for developing portable imaging systems.
- A novel method to test the sensitivity of the system was developed. Using this approach, the sensitivity experiments can be performed in a fast and convenient way.
- The reconstructed conductivity distributions of the agar phantoms show the exact location, actual size and geometry of the objects. This quality has not been achieved before in electrical conductivity imaging via contactless measurements.
- The image of a living tissue is acquired for the first time in the literature.
- Multi-frequency experiments were performed and reconstructed conductivity distribution images have been obtained for the first time in the literature.
- Magnetic conductivity spectroscopy of a biological tissue is shown for the first time in electrical conductivity imaging via contactless measurements.

5.2 Future Work

Following work sequence is proposed for future studies:

- The effects of neglecting $\nabla\phi$ in the inverse problem solution should be investigated.
- Multi-frequency biological tissue experiments should be performed.
- The permittivity images should be obtained in addition to conductivity images.
- 1 or 2 dimensional sensor arrays using coil or other magnetic sensors should be used. This will increase the speed of the data acquisition process (measurement and analysis).
- Instead of using coils, different type of magnetic sensors such as Hall effect sensors etc. should be used to measure the secondary magnetic fields.
- Automatic calibration or nulling circuit should be developed.
- A portable system that can be used for clinical applications should be developed.

REFERENCES

- [1] D. C. Barber and B. H. Brown, “Applied potential tomography (review article),” *J. Phys.*, vol. 17, pp. 723–733, 1984.
- [2] T. Ahmad and N. G. Gençer, “Development of data acquisition system for conductivity images of biological tissues via contactless measurements,” *Proceedings of 23rd Annual EMBS International Conference, İstanbul, Turkey*.
- [3] T. Ahmad, “Experimental studies on development of a new imaging system for contactless subsurface conductivity imaging of biological tissues,” Master’s thesis, METU, AUGUST 2001.
- [4] H. P. Schwan *Therapeutic Heat and Cold ed S Licht (Baltimore: Waverly)*, pp. 63–125, 1965.
- [5] T. Yamamoto and Y. Yamamoto *Med. Biol. Eng.*, vol. 14, pp. 494–499, 1976.
- [6] *UAF42, Universal Active Filter Datasheet, Burr – Brown*.
- [7] H. W. Ott, *Noise Reduction Techniques in Electronic Systems*. John Wiley and Sons, Inc., 2nd Ed. 1988.
- [8] *WIKIPEDIA, The Free Encyclopedia, Medical Imaging, www.wikipedia.org* , December 2005.
- [9] D. A. Boas, D. H. Brooks, E. Miller, C. A. DiMarzio, M. Kilmer, R. J. Gaudette, and Z. Quan, “Imaging the body with diffuse optical tomography,” *Signal Processing Magazine, IEEE*, vol. 18, pp. 57–75, November 2001.
- [10] E. Konofagou, J. D’hooge, and J. Ophir, “Cardiac elastography- a feasible study,” *Ultrasonic Symposium, 2000 IEEE*, vol. 2, pp. 1273–1276, October 2000.
- [11] J. Webster, *Electrical Impedance Tomography*. No. 0-85274-304-1, IOP Publishing, 1990.
- [12] A. G. Webb, *Introduction to Biomedical Engineering*. Hardcover: IEEE Press Series on Biomedical Engineering, 1st ed., December 2002.

- [13] J. J. Niederhauser, M. Jaeger, R. Lemor, P. Weber, and M. Frenz, "Combined ultrasound and optoacoustic system for real-time high-contrast vascular imaging in vivo," *IEEE Transactions on Medical Imaging*, vol. 24, pp. 436–440, April 2005.
- [14] M. V. Ranganath, A. P. Dhawan, and N. Mullani, "A multigrid expectation maximization reconstruction algorithm for positron emission tomography," *IEEE Transactions on Medical Imaging*, vol. 7, pp. 273–278, December 1988.
- [15] L. Cerullo, "Laser neurosurgery: Past, present, and future," *IEEE Journal of Quantum Electronics*, vol. 20, pp. 1397–1400, December 1984.
- [16] J. Morucci and B. Rigaud, "Bioelectrical impedance techniques in medicine," *Crit. Rev. Biomed. Eng.*, vol. 24, pp. 467–597, 1996.
- [17] D. Isaacson, "Distinguishability of conductivities by electric current computed tomography," *IEEE Trans. Med. Imag.*, vol. 5, pp. 91–95, 1986.
- [18] J. Bronzino, "The biomedical engineering handbook," *IEEE Press, CRC Press*, 1995.
- [19] W. R. Purvis, R. Tozer, D. Anderson, and I. Freeston, "Induced impedance imaging," *IEEE Proceedings-A*, vol. 140, pp. 135–141, 1993.
- [20] N. G. Gençer, M. Kuzuoglu, and Y. Z. Ider, "Electrical impedance tomography using induced currents," *IEEE Trans. Med. Imag.*, vol. 13, pp. 338–350.
- [21] N. G. Gençer, Y. Z. Ider, and S. Williamson, "Electrical impedance tomography: Induced current imaging achieved with a multiple coil system," *IEEE Trans on Med. Imag.*, vol. 43, pp. 139–149, 1996.
- [22] N. G. Gençer, *Electric impedance tomography using induced currents*. PhD thesis, METU, JULY 1993.
- [23] I. Freeston and R. Tozer, "Impedance imaging using induced currents," *Physiol. Meas.*, vol. 16, pp. 257–266, 1995.
- [24] S. Zlochiver, M. Radai, M. S. Abboud, M. Rosenfeld, X. Dong, R.-G. Liu, F.-S. You, H.-Y. Xiang, and X.-T. Shi, "Induced current electrical impedance tomography system: Experimental results and numerical simulations," *Physiol. Meas.*, vol. 25, pp. 239–255, 2004.
- [25] R. H. Ireland, J. C. Tozer, A. T. Barker, and D. C. Barber, "Towards magnetic detection eit: Data acquisition and image reconstruction of current density in phantoms in vivo," *Physiol. Meas.*, vol. 25, pp. 775–796, 2004.
- [26] B. M. Eyuboglu, B. H. Brown, D. C. Barber, and A. Seager, "Localization of cardiac related impedance changes in the thorax," *Clin. Phys. Physiol. Meas.*, vol. 8, pp. A167–A173, 1987.

- [27] B. M. Eyuboglu and B. H. Brown, "Methods of cardiac gating applied potential tomography," *Clin. Phys. Physiol. Meas.*, vol. 9, pp. 43–48, 1988.
- [28] B. M. Eyuboglu, B. H. Brown, and D. C. Barber, "Problems of cardiac output determination from eit scans," *Clin. Phys. Physiol. Meas.*, vol. 9, pp. 71–77, 1988.
- [29] G. Piperno, E. Frei, and M. Moshitzky, "Breast cancer screening by impedance measurements," *Frontiers Med. Biol. Eng.*, vol. 2, pp. 111–117, 1990.
- [30] V. Cherepenin, A. Karpov, A. Korjnevsky, V. Kornienko, A. Mazaletskaya, D. Mazurov, and D. Meister, "A 3d electrical impedance tomography (eit) system for breast cancer detection," *Physiol. Meas.*, vol. 22, pp. 9–18, 2001.
- [31] T. E. Kerner, K. D. Paulsen, A. Hartov, S. Soho, and S. P. Poplack, "Electrical impedance spectroscopy of the breast: Clinical results in 26 subjects," *IEEE Trans. Med. Imaging*, vol. 21, pp. 638–645, 2002.
- [32] K. S. Nirmal, A. Hartov, C. Kogel, S. P. Poplack, and K. D. Paulsen, "Multi-frequency electrical impedance tomography of the breast: New clinical results," *Physiol. Meas.*, vol. 25, pp. 301–314, 2004.
- [33] V. Cherepenin, A. Karpov, A. Korjnevsky, V. Kornienko, Y. Kultiasov, A. Mazaletskaya, and D. Mazurov, "Preliminary static eit images of the thorax in health and disease," *Physiol. Meas.*, vol. 23, pp. 33–41, 2002.
- [34] R. Merwa, K. Hollaus, O. Biro, and H. Scharfetter, "Detection of brain oedema using magnetic induction tomography: a feasibility study of the likely sensitivity and detectability," *Physiol. Meas.*, vol. 25, pp. 347–354, 2004.
- [35] D. Holder, "Editorial, biomedical applications of electrical impedance tomography," *Physiol. Meas.*, vol. 23, 2002.
- [36] A. A. Kaufman and G. V. Keller, *Induction Logging*. Amsterdam, Netherland: Elsevier Science Publishers, 1989.
- [37] H. Libby, *Introduction to Electromagnetic Nondestructive Test Methods*. John Willey & Sons, Inc, 1971.
- [38] J. Blitz, *Electrical and Magnetic Methods of Nondestructive Testing*. Adam Hilger Imprinted by IOP Publishing Ltd., 1991.
- [39] R. P. Henderson and J. G. Webster, "An impedance camera for spatially specific measurements of the thorax," *IEEE Trans. Biomed. Eng.*, vol. 25, pp. 250–254, 1978.
- [40] P. Tarjan and R. McFee, "Electrodeless measurements of the active resistivity of the human torso and head by magnetic induction," *IEEE Transactions on Biomedical Engineering*, vol. 15, pp. 266–278, 1968.

- [41] S. Al-Zeibak and N. H. Sunders, “A feasibility study of in vivo electromagnetic imaging,” *Phys. Med. Biol.*, vol. 38, pp. 151–160, 1993.
- [42] J. Netz, E. Forner, and S. Haagemann, “Contactless impedance measurement by magnetic induction- a possible method for investigation of brain impedance,” *Physiol. Meas.*, vol. 14, pp. 463–471, 1993.
- [43] A. V. Korzhenevskii and V. A. Cherepenin, “Magnetic induction tomography,” *J. Commun. Tech. Electron.*, vol. 42, pp. 469–474, 1997.
- [44] A. Korjenevsky and V. C. and S. Sapetsky, “Magnetic induction tomography: experimental realization,” *Physiol. Meas.*, vol. 21, pp. 89–94, 2000.
- [45] A. Korjenevsky and S. Sapetsky, “Methods of measurements and image reconstruction in magnetic induction tomography,” *Proc. 2nd EPSRC Engineering Network Meeting on Biomedical Applications of EIT*, April, London, 2000.
- [46] H. Griffiths, “Magnetic induction tomography,” *Meas. Sci. Technol.*, vol. 12, pp. 1126–1131, 2001.
- [47] H. Scharfetter, H. Lackner, and J. Rossel, “Magnetic induction tomography: Hardware for multi-frequency measurements in biological tissues,” *Physiol. Meas.*, vol. 22, pp. 131–146, 2001.
- [48] J. Rossel, R. Casanas, and H. Scharfetter, “Sensitivity maps and system requirements for magnetic induction tomography using a planer gradiometer,” *Physiol. Meas.*, vol. 22, pp. 121–130, 2001.
- [49] H. Scharfetter, P. Rui, M. Populo, and J. Rossel, “Sensitivity maps for low-contrast perturbations within conducting background in magnetic induction tomography,” *Physiol. Meas.*, vol. 22, pp. 195–202, 2002.
- [50] K. Hollaus, C. Magele, R. Merva, and H. Scharfetter, “Fast calculation of the sensitivity matrix in magnetic induction tomography by tetrahedral edge finite elements and the reciprocity theorem,” *Physiol. Meas.*, vol. 25, pp. 159–168, 2004.
- [51] N. G. Gençer and M. N. Tek, “Electrical conductivity imaging via contactless measurements,” *IEEE Trans. On Med. Imag.*, vol. 18, pp. 617–627, 1999.
- [52] R. Merva, K. Hollaus, P. Brunner, and H. Scharfetter, “Solution of the inverse problem of magnetic induction tomography (mit),” *Physiol. Meas.*, vol. 26, pp. 241–250, 2005.
- [53] S. Watson, A. Morris, R. J. Williams, H. Griffiths, and W. Gough, “A primary field compensation scheme for planar array magnetic induction tomography,” *Physiol. Meas.*, vol. 25, pp. 271–279, 2004.

- [54] A. Morris, H. Griffiths, and W. G. and, “A numerical model for magnetic induction tomographic measurements in biological tissues,” *Physiol. Meas.*, vol. 22, pp. 113–119, 2001.
- [55] S. Watson, C. H. Igney, O. Dossel, R. J. Williams, and H. Griffiths, “A comparison of sensors for minimizing the primary signal in planar-array magnetic induction tomography,” *Physiol. Meas.*, vol. 26, pp. 319–331, 2005.
- [56] C. H. Igney, S. Watson, R. J. Williams, H. Griffiths, and O. Dossel, “Design and performance of a planar-array mit system with normal sensor alignment,” *Physiol. Meas.*, vol. 26, pp. 263–278, 2005.
- [57] N. G. Gençer and M. N. Tek, “Imaging tissue conductivity via contactless measurements: A feasible study,” *TUBITAK Elektrik J.*, vol. 6, pp. 183–200, 1998.
- [58] N. G. Gençer and M. N. Tek, “Forward problem solution for electrical conductivity imaging via contactless measurements,” *Phys. Med. Biol.*, vol. 44, pp. 927–940, 1999.
- [59] B. Ülker and N. G. Gençer”, “Electrical conductivity imaging via contactless measurements: An experimental study,” *IEEE Trans. On Med. Imag.*, vol. 22, pp. 627–635, 2003.
- [60] İlyas Evrim Çolak, “An improved data acquisition system for contactless conductivity imaging,” Master’s thesis, METU, APRIL 2005.
- [61] B. Ülker, “Electrical conductivity imaging via contactless measurements an experimental study,” Master’s thesis, METU, DECEMBER 2001.
- [62] B. Ülker and N. G. Gençer”, “Implementation of a data acquisition system for contactless conductivity imaging,” *IEEE Eng. Med. Biol.*, pp. 152–155, 2002.
- [63] H. P. Schwan, “Biological effects of non-ionizing radiations: Cellular properties and interactions,”
- [64] H. P. Schwan, *Dielectric properties of body tissues*. No. 75–96, Plenum Press, 1985.
- [65] J. Jackson, *Classical Electrodynamics*. John Wiley and Sons Inc., 1998.
- [66] S. Williamson, G. Romani, L. Kaufman, and I. Modena, eds., *Physical concepts and mathematical models in biomagnetism: An Interdisciplinary Approach*. New York: Plenum Press pp. 101-139, 1983.
- [67] G. H. Golub and C. F. van Loan, *Matrix Computation*. The John Hopkins University Press, 1983.
- [68] M. S. Bazaraa, H. D. Sherali, and C. M. Shetty, *Nonlinear Programming Theory and Algorithms*. John Wiley & Sons Inc., 1993.

- [69] A. B. J. Axelson Ceviren: C. Gercek Editor: G. Dincer Katkda Bulunanlar: Z. Aytemur, *Her Yonuyle Seri Port.* www.Tekno-market.com yaynlar, 2000.
- [70] *PIC16F877 Microcontroller Datasheet, Microchip.*
- [71] *LF351, Operational Amplifier Datasheet, National Semiconductors.*
- [72] *LF356, Operational Amplifier Datasheet, National Semiconductors.*
- [73] *AD633, Analog Multiplier Datasheet, Analog Devices.*
- [74] R. Pethig, "Dielectric properties of body tissues," *Clin. Phys. Physiol. Meas.*, vol. 8, Supp. A, pp. 5–12, 1987.
- [75] S. Webb, *The Physics of Medical Imaging.* Bristol: IOP Publishing Limited, 1988.
- [76] M. N. Tek, "Electrical conductivity imaging via contactless measurements: Forward and inverse problem simulations," Master's thesis, METU, JULY 1998.

APPENDIX A

Useful Assumptions

In this section the effects of 1) the displacement currents, 2) the propagation term e^{-jkR} in formulation of the forward problem for frequencies at or below 100 kHz are discussed. Then, the necessary assumptions for the quasi-static conditions in electromagnetic fields are determined.

A.1 Effects of Displacement Currents

The relative permittivity ϵ_r ($\epsilon = \epsilon_r \epsilon_0$) of biological tissues decreases with increasing frequency [74]. The $(\sigma + j\omega\epsilon) = \sigma(1 + \frac{j\omega\epsilon}{\sigma})$ term in $\vec{J} = (\sigma + j\omega\epsilon) \vec{E}$ represents the complex electrical properties of the conductive medium and the $(\omega\epsilon)$ term corresponds to the displacement current density. When tissue impedance measurements are considered, the dielectric effects are usually neglected at or below 100 kHz [75]. In order to verify this Tek and Gençer calculated the ratio $\frac{\omega\epsilon}{\sigma}$ for various tissue types at different frequencies up to 100 kHz (Table A.1) and they concluded that the displacement currents can be negligible for frequencies at or below 100 kHz [76] (pages 17-19).

A.2 Effects of e^{-jkR} Term

The question is whether e^{-jkR} term is neglected for biological tissues or not. The effects of e^{-jkR} are investigated in the formulation of the forward problem in [76] (pages 19-20). For this purpose quantitative values of wavelengths and skin depths according to operating frequencies are calculated for an average

Table A.1: Ratio of displacement to conduction currents for various frequencies and body tissues.

Frequency (kHz)	0.01	0.1	1	10	40.96	100
Lung	0.15	0.025	0.05	0.14	0.422	-
Fat	-	0.01	0.03	0.15	0.020	0.015
Liver	0.20	0.035	0.06	0.20	0.331	0.529
Heart Muscle	0.10	0.04	0.15	0.32	-	-
Skeletal M. (longi.)	0.0069	0.0153	0.0556	-	0.036	0.190
Skeletal M. (trans.)	0.01	0.12	0.7	-	-	-
Bone	-	-	0.008	0.053	0.151	0.107
Kidney	-	-	-	-	0.309	0.385
Spleen	-	-	-	-	0.093	0.0297

tissue conductivity of 0.2 S/m and a survey distance of $R_{max} = 0.2$ m in the object region (Table A.2). Also propagation related parameters, magnitude and phase of $e^{-j\mathbf{k}\mathbf{R}}$, are determined (Table A.3). As seen in Table A.3 the effect of $e^{-j\mathbf{k}\mathbf{R}}$ term can be neglected up to 100 kHz in biological tissues ([76]).

Table A.2: Wavelengths and skin depths for various frequencies, The wavelength and the skin depth is defined as: $\lambda = \frac{2\pi}{\beta}$ and $\sigma = \frac{1}{\alpha}$, respectively. The wave number k can be express as $k = \alpha + j\beta$.

Frequency (kHz)	$\lambda(\mathbf{m})$	σ
1	143.91	55.30
10	45.51	17.48
50	20.35	7.82
100	14.39	5.53

Table A.3: Propagation related parameters for various frequencies. Error column shows the percentage error of magnitude from unity. Magnitude and phase difference of $e^{-j\mathbf{k}\mathbf{R}}$ is tabulated.

Frequency(kHz)	R=20 cm			R=10 cm		
	$ e^{-jkR} $	P(°)	error (%)	$ e^{-jkR} $	P(°)	error (%)
1	0.9921	0.46	0.79	0.9960	0.22	0.40
10	0.9752	1.44	2.48	0.9875	0.72	1.25
50	0.9454	3.22	5.46	0.9723	1.61	2.77
100	0.9236	4.55	7.64	0.9610	2.27	3.90

APPENDIX B

RESISTANCE OF A CONDUCTIVE RING

Let us assume that a magnetic flux density $B(t) = B_0 \cos(\omega t) \vec{a}_z$ is applied to a conductive ring of conductivity σ , with inner radius of b and outer radius of a , placed on the x-y plane as shown in Figure 2.2. Voltage induced around contour can be found starting from Maxwell Equations:

$$\nabla \times E = -\frac{dB}{dt} \quad (\text{B.1})$$

Applying Stokes's theorem to B.1 and using (2.12) we can write:

$$\begin{aligned} \oint_C \vec{E} \cdot d\vec{l} &= \int_S -\frac{dB}{dt} = V_{induced} \\ &= -\frac{d\Phi}{dt} = V_{induced} \end{aligned} \quad (\text{B.2})$$

Taking the surface integral of B over surface S which is encircled by contour (Figure 2.2),

$$\begin{aligned} \Phi &= B \cdot S \\ &= B_0 \cos(\omega t) \pi (r^2 - b^2) \end{aligned} \quad (\text{B.3})$$

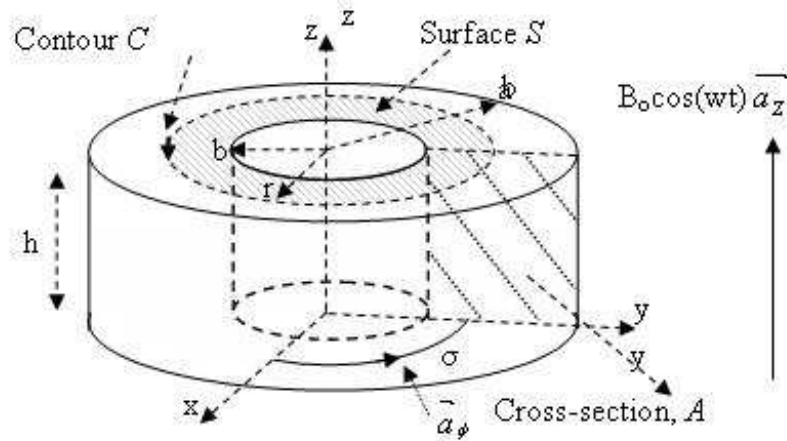


Figure B.1: The conductive ring. A z-directed magnetic field applied to a conductive ring of inner radius b and outer radius a . Height of the ring is indicated as h .

The time derivative of is obtained as follows,

$$\begin{aligned} -\frac{d\Phi}{dt} &= -\frac{d(B_0 \cos(\omega t) \pi(r^2 - b^2))}{dt} \\ &= -\frac{d(B_0 \cos(\omega t) \pi r^2)}{dt} \end{aligned} \quad (\text{B.4})$$

Since the magnitude of the electric field is constant on a specific contour C , using cylindrical coordinates, combining Eq. B.2 and Eq. B.4 we obtain:

$$E_\phi \cdot 2\pi r = \pi r^2 \omega B_0 \sin(\omega t) \quad (\text{B.5})$$

$$E_\phi = \frac{1}{2} B_0 r \omega \sin(\omega t) \vec{a}_\phi \quad (\text{B.6})$$

Since \vec{E} has only the \vec{a}_ϕ component,

$$\vec{E} = \frac{1}{2} B_0 r \omega \sin(\omega t) \vec{a}_\phi \quad (\text{B.7})$$

Thus, the current density \vec{J} can be found by multiplying electric field with conductivity σ :

$$\vec{J} = \sigma \vec{E} = \sigma \frac{1}{2} B_0 r \omega \sin(\omega t) \vec{a}_\phi \quad (\text{B.8})$$

Current flowing in the conductive ring is then found by integrating the current density:

$$\begin{aligned} I &= \int_A \vec{J} \cdot d\vec{S} = \int_0^h \int_b^a \frac{\sigma B_0 \omega r}{2} \sin(\omega t) dr dz \\ &= \frac{\sigma B_0 h \omega (a^2 - b^2)}{4} \sin(\omega t) \end{aligned} \quad (\text{B.9})$$

The dissipated power (Eddy current loss) can be obtained as follows:

$$\begin{aligned} P &= \int_V \vec{J} \cdot \vec{E} dV = \int_V \sigma |E|^2 dV \\ &= \int_0^h \int_0^{2\pi} \int_b^a \frac{\sigma B_0^2 \omega^2 r^2}{4} \sin^2(\omega t) r dr d\phi dz \\ &= \frac{\sigma B_0^2 \pi h (a^4 - b^4)}{8} \omega^2 \sin^2(\omega t) \end{aligned} \quad (\text{B.10})$$

Since $P = \frac{1}{2} I^2 R$, using Eq. B.7 and Eq. B.8, the effective resistance R of the conductive ring can be obtained as:

$$R = \frac{P}{I^2} = \frac{4\pi a^2 + b^2}{\sigma h a^2 - b^2} \quad (\text{B.11})$$

APPENDIX C

MAGNETIC FIELD MEASUREMENT USING RESISTIVE RING EXPERIMENT

Secondary voltage induced in the receiver coils due to secondary flux generated by the resistive ring is measured by using the circuit shown in Figure C.1. A 3-turn coil with diameter of 9 mm is prepared and placed on the sensor. The terminals of the ring are shunted with resistors. The primary flux created by the transmitter coil induces eddy currents in the 3-turn coil. However the eddy currents cannot flow in the ring unless the terminals of the ring are shunted with a resistor. Since the transmitter current's amplitude and frequency is constant, the amplitude of the current flowing in the 3-turn ring is inversely proportional to the resistor shunting the ring. Consequently, the secondary flux generated by the resistive ring is controlled with the shunting resistor. If the resistor value is decreased, the current flowing in the ring will be increased and vice versa. The operation principle of the circuit is explained in Section 3.1.1.

6 resistances varied in the range of 260Ω - 10000Ω (Table C.1) are connected to the open ends of the 3-turn coil (i.e. the coil is shunted with the resistors). In experiments, first, the ring is shunted to a resistor and measurements are performed (100 samples are taken for each measurement), then, another measurements are performed after making the ring open (eddy currents cannot flow in the ring, thus, no secondary field is generated). The former data is subtracted from the latter and the difference data is obtained, thus, the effect

Table C.1: Resistor values (and corresponding $1/(\text{resistor values})$) used in the resistive ring experiments.

<i>Resistor Values</i> (Ω)	265	553	1178	3303	5054	9829
<i>1/(Resistor Values)</i> ($\text{V} \times 10^{-4}$)	38	18	8	3	2	1

of voltage drift in the receiver coils is cancelled out. No voltage drift is observed in the coils when the system become stable (4 hours should be elapsed from the starting of the set-up). However, in this study always the difference data is obtained and used. Mean value of the difference data is determined for each resistance and plotted as a function of the inverse of the resistance values as shown in Figures in the RESULTS Chapter (Chapter 4). As an example mean value of the difference data obtained in the prototype system is plotted as a function of the resistor values in Figure C.2(a) and in Figure C.2(b) the same data plotted for $1/(\text{Resistor values})$.

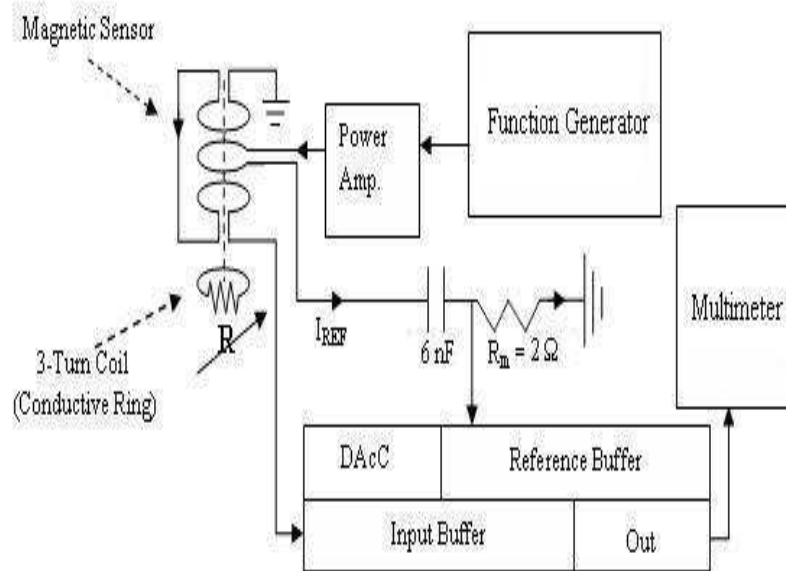
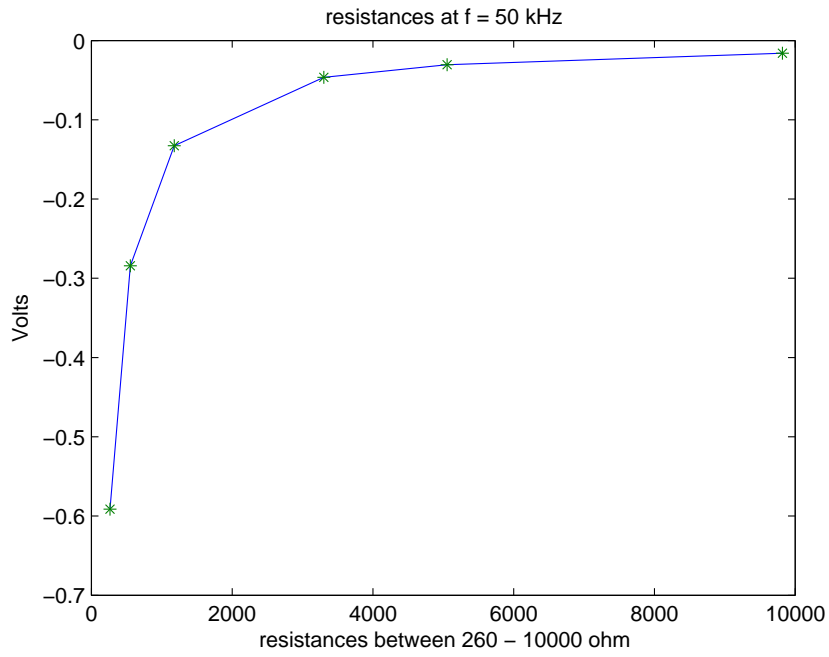
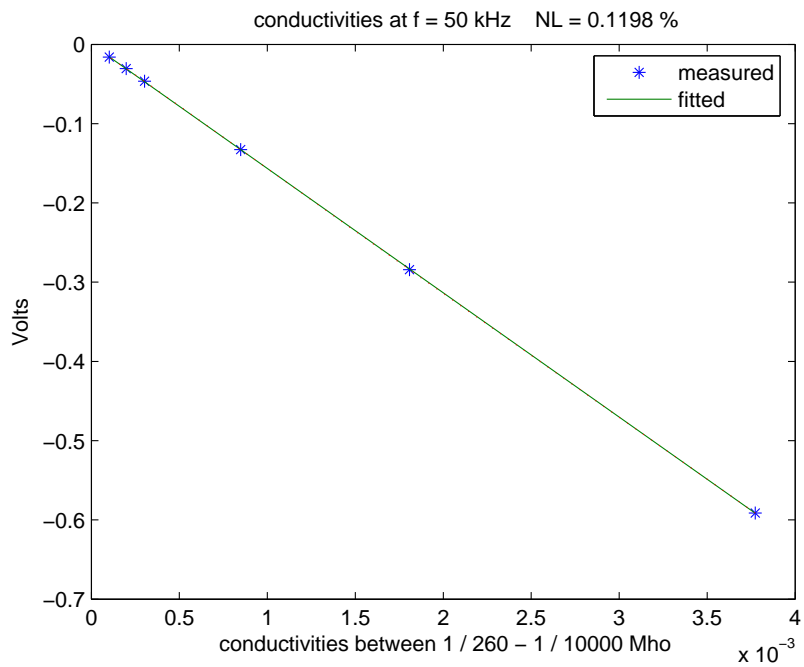


Figure C.1: Magnetic field measurement using resistive ring experiment setup



(a)



(b)

Figure C.2: Receiver coil output voltage versus conductivity plot obtained by using resistive ring. Mean value of the difference data is plotted as a function of: (a) resistor values, (b) 1/(resistor values) (100 sample are taken for each measurement).

APPENDIX D

THERMAL NOISE

Thermal noise comes from thermal agitation of electrons within a resistance, and it sets a lower limit on the noise present in a circuit. The open-circuit rms noise voltage produced by a resistance is ¹ :

$$V_t = \sqrt{4kTBR} \quad (\text{D.1})$$

where

K=Boltzmann's constant ($1.38 \times 10^{-23} \text{joules}/^\circ K$),

T=absolute temperature ($^\circ K$),

B=noise bandwidth(Hz),

R=resistance (Ω).

At room temperature ($290^\circ K$), $4kT$ equals $1.6 \times 10^{-20} W/Hz$.

¹

Ott, *Noise Reduction Techniques in Electronic Systems*, 1988 [7]

D.1 Equivalent Noise Bandwidth

The noise bandwidth B is the voltage-gain-squared bandwidth of the system or circuit being considered. The noise bandwidth is defined for a system with uniform gain throughout the passband and zero gain outside the passband. Figure D.1 shows this ideal response for a low-pass circuit and a band-pass circuit.

However, since practical circuits do not have these ideal characteristics, the area under the equivalent noise bandwidth is made equal to the area under the actual curve. This shown in Figure D.2 for a low pass circuit. For any network transfer function, $A(f)$ (expressed as a voltage or current ratio), there is an equivalent noise bandwidth with constant magnitude of transmission A_0 and bandwidth of

$$B = \frac{1}{|A_0|^2} \int_0^\infty |A(f)|^2 df \quad (\text{D.2})$$

Table D.1 gives the ratio of the noise bandwidth to the 3-dB bandwidth for circuits with various numbers of identical poles [7].

Table D.1: Ratio of the Noise Bandwidth B to the 3-dB Bandwidth f_0

Number of Poles	B/f_0	High-Frequency Rolloff (dB per Octave)
1	1.57	6
2	1.22	12
3	1.15	18
4	1.13	24
5	1.11	30

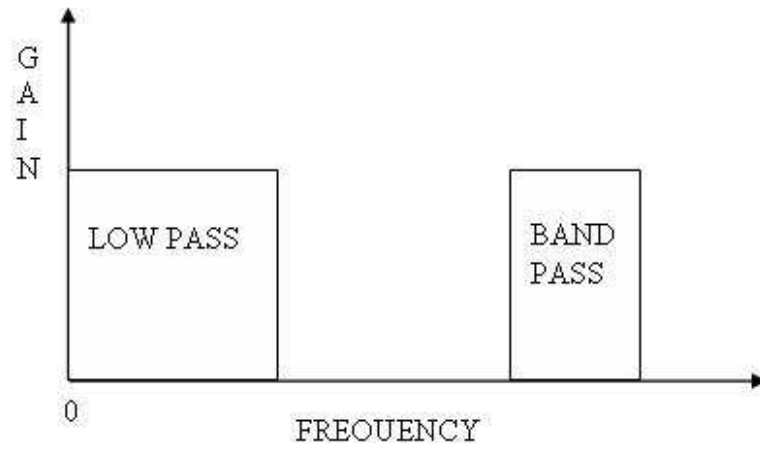


Figure D.1: Ideal bandwidth of low-pass and band-pass circuit elements

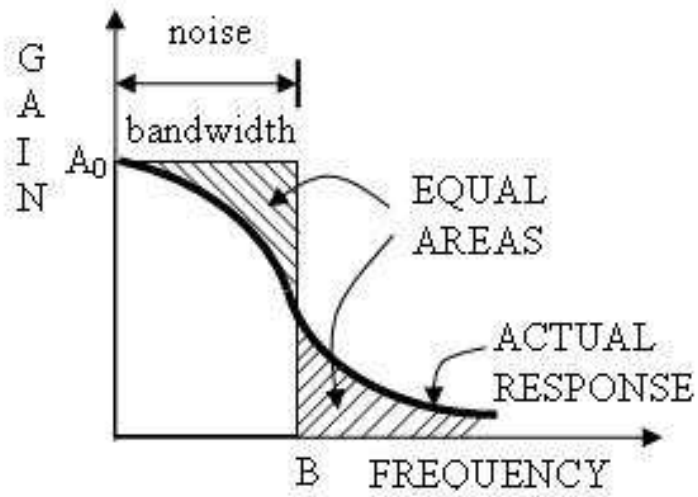


Figure D.2: Actual response and equivalent noise bandwidth for low-pass circuit.

D.2 Noise In IC Operational Amplifiers

The noise characteristics of an op-amp can be modelled by using the equivalent input noise voltage and current $V_n - I_n$. Typical op-amp circuit is shown in Figure D.3. The same circuit with the equivalent noise voltage and current sources included is shown in Figure D.4(a).

The equivalent circuit in Figure D.4(a) can be used to calculate the total equivalent input noise voltage, which is

$$V_{nt} = [4kTB(R_{s1} + R_{s2}) + V_{n1}^2 + V_{n2}^2 + (I_{n1}R_{s1})^2 + (I_{n2}R_{s2})^2]^{\frac{1}{2}} \quad (\text{D.3})$$

It should be noted that V_{n1} , V_{n2} , I_{n1} and I_{n2} (given in the Datasheets of the components) are also functions of the bandwidth B . The two noise voltage sources of Equation D.3 can be combined by defining

$$(V'_n)^2 = V_{n1}^2 + V_{n2}^2 \quad (\text{D.4})$$

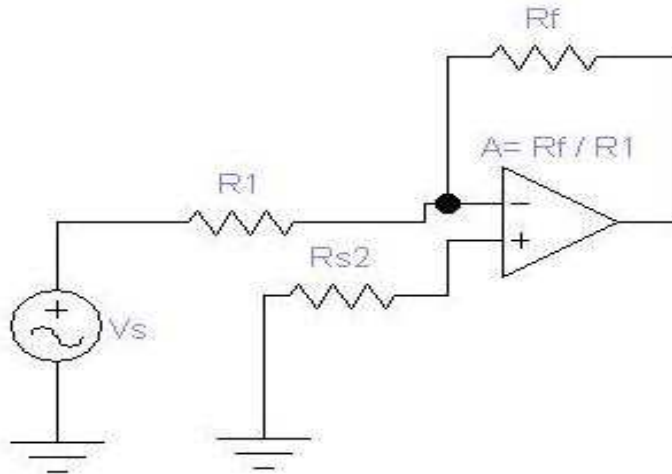


Figure D.3: Typical op-amp circuit with an absolute gain $A = \frac{R_f}{R_1}$

Equation D.3 can then be written as

$$V_{nt} = [4kTB(R_{s1} + R_{s2}) + (V'_n)^2 + (I_{n1}R_{s1})^2 + (I_{n2}R_{s2})^2]^{\frac{1}{2}} \quad (\text{D.5})$$

Although the voltage sources have been combined, the two noise current sources are still required in Equation D.5. If, however, $R_{s1} = R_{s2}$, which is usually the case, then the two noise current generators can be combined by defining

$$(I'_n)^2 = I_{n1}^2 + I_{n2}^2 \quad (\text{D.6})$$

For $R_{s1} = R_{s2} = R_s$, Equation D.5 reduces to

$$V_{nt} = [4kTB(R_{s1} + R_{s2}) + (V'_n)^2 + (I_n R_s)^2]^{\frac{1}{2}} \quad (\text{D.7})$$

The equivalent circuit for this case is shown in Figure D.4(b). To obtain optimum noise performance (maximum signal-to-noise-ratio) from an op-amp, the total equivalent input noise voltage V_{nt} should be minimized [7] (pages 267-269).

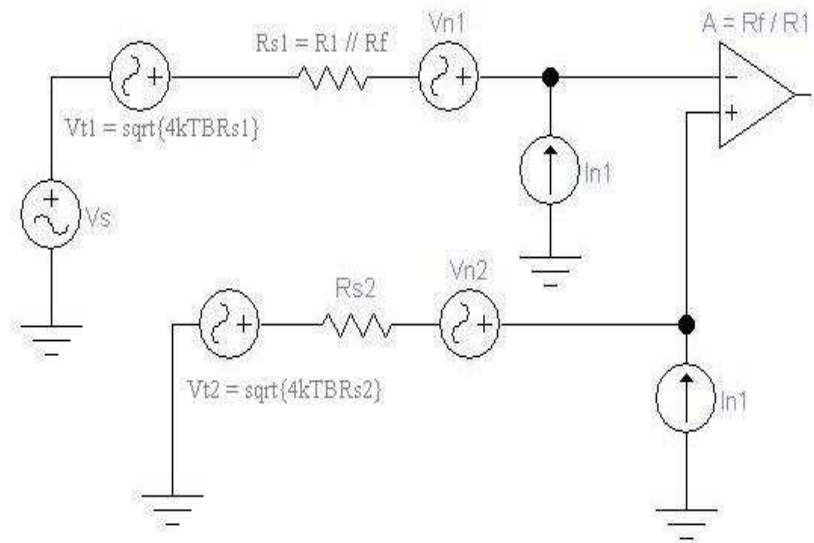
D.3 Addition of Noise Voltages

When noise sources added together, the total power is equal to the sum of the individual powers. Adding two noise voltage generators V_1 and V_2 , together on a power basis, gives [7]

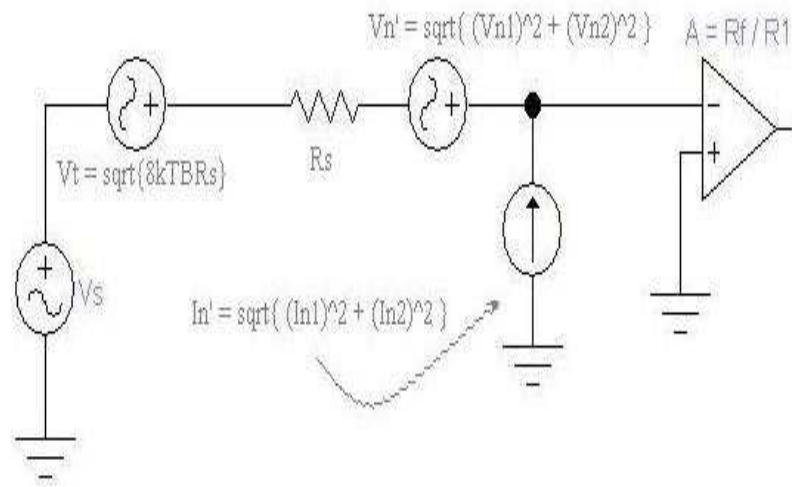
$$V_{total}^2 = V_1^2 + V_2^2 \quad (\text{D.8})$$

The total noise voltage can then be written as

$$V_{total} = \sqrt{V_1^2 + V_2^2} \quad (\text{D.9})$$



(a)



(b)

Figure D.4: Typical op-amp circuit (Figure D.3) with the equivalent noise voltage and current sources included; (a) Circuit of Figure D.3 with noise sources added; (b) Circuit of Figure D.4(a) with noise sources combined at one terminal for the case $R_{s1} = R_{s2} = R_s$.

APPENDIX E

AGAR PHANTOM PREPARATION

E.1 Equipment and Materials Needed

- Agar powder
- Distilled water
- Table salt or NaCl
- Heater
- Beaker or Erlenmeyer flask

E.2 Preparation

1. Decide how much agar is needed according to the desired conductivity. If you add ρ gr of NaCl and 1.5 gr agar powder to 100 ml distilled water, the conductivity of the solution will be [11]:

$$S = 0.02\rho \text{ S/cm} \tag{E.1}$$

2. Choose a beaker or erlenmeyer flask that is 2-4 times the volume of the solution.
3. Place the flask above heater. Bring the solution to a boil while stirring. Agar powder will be dissolved and solution change color to light brown.
4. Lower the heat and simmer until no air bubble remains.

5. Pour the agar solution into the phantom of desired shape and let the gel sit undisturbed until cool (approximately 15 minutes). The agar will change color from clear to slightly milky [61].